# CEREBRAL HEMODYNAMICS IN HIGH-RISK NEONATES PROBED BY DIFFUSE OPTICAL SPECTROSCOPIES

Erin M. Buckley

A DISSERTATION

in

Physics and Astronomy

Presented to the Faculties of the University of Pennsylvania

in

Partial Fulfillment of the Requirements for the

Degree of Doctor of Philosophy

2011

Supervisor of Dissertation:

_____

Arjun G. Yodh

Professor of Physics and Astronomy

Graduate Group Chairperson:

_____

A.T. Charlie Johnson

Professor of Physics and Astronomy

Dissertation Committee:

Andrea Liu, Professor of Physics

Philip Nelson, Professor of Physics

Joel Greenberg, Professor of Neurology

Joseph Kroll, Professor of Physics

Daniel Licht, Asst. Professor of Neurology

## Acknowledgements

As I transcribe the culmination of my six years in graduate school, I am overwhelmed by the number of people to whom I owe thanks for helping me get to this point. First and foremost, I am today thanks to the love, support, and encouragement of my wonderful mom. I could not have asked for a better person to raise me, to teach me, and to always lend an ear to listen. Second, I do not know what I would do without my amazing boyfriend, Peter Yunker, who has been my biggest fan since the day we first met. He's my best friend, my shoulder to lean/cry on, and my favorite person to be around.

I came to Penn thinking I would pursue particle physics. However, during my first year, I was lucky enough to catch a talk by Arjun Yodh on his biomedical optics research. It was perfect: a way for me to combine my love of physics with the possibility of helping people by answering clinical questions as well. Not only was the research exciting, but I also signed on with an advisor who is an extremely talented and brilliant researcher. Arjun has been an excellent mentor. He encourages independence and creativity, and he makes a point to always be available to his students if they need him. He has taught me many research skills: paying attention to every detail, giving a clear presentation, designing a strong experiment, writing grants, etc.

In my first few years in the lab, Turgut Durduran was a co-mentor and Arjun's right-hand man. Turgut imparted his extensive experience in the lab to me with patience (lots of patience!), and his presence in the lab was invaluable to me. He taught me so much, for example: diffusion theory, experimentation, coding, computers, etc. Further, he took me under his wing and included me in so many collaborations with valuable

contacts around Penn. I really felt like a valuable part of a team with Turgut, instead of a just young student trying to learn the basics.

Not only have I have great mentors in my physics work, but I have also had the privilege to work with some excellent clinical collaborators, including Joel Greenberg, John Detre, and Daniel Licht. In particular, I have worked closely with Dan, who has taught me an immense amount of physiology and neurology. He is a very patient and passionate researcher, and I truly enjoyed all of our time together (and had fun too!). His rigorous support of me and of my endeavors has meant so much to me. Not to mention, he has greatly helped us promote our optical techniques throughout CHOP and to pediatric neurologists across the country.

In addition to Dan, the research I have conducted in this dissertation would not have been possible without the help of so many people at the Children's Hospital of Philadelphia. Donna Goff, Noah Cook, Mark Fogel, Matthew Harris, Susan Nicholson, Lisa Montenegro, Maryam Naim, Laura Diaz, Peter Schwab, Grady Hedstrom, Justine Wilson and the rest of the MRI technicians, Kathy Mooney, Kerri Kelly, all the guys down in biomedical engineering, and the CICU nurses have all gone above and beyond the call of duty to ensure that we recruit patients and acquire quality data. I cannot thank them all enough for their efforts and enthusiasm.

I must also acknowledge the many members of Arjun's lab who have helped me in so many different ways and made life fun in the process: Leonid Zubkov, who is my go-to guy for instrumentation help or for a good story about his past (or his dog); David Busch, who supported me and commiserated with me during the long, drawn out process of writing a thesis, and who is also always willing to drop everything to help with

troubleshooting experiments or have ideas bounced off of him; Meeri Kim, who has been my partner in crime since we both joined the lab and whose support, empathy, gossip, and friendship has helped me get through trying times; Wes Baker, who has not only been a great friend, but he has also spent endless hours of patiently enhancing my understanding of diffusion theory; Han Ban, who always drops by my office to say hi and discuss life; Dalton Hance, who willingly came to all of our early morning studies; and the numerous other members of the lab who I've had the privilege to work with- Chao Zhou, Guoqiang Yu, Regine Choe, Sophie Chung, Rickson Mesquita, Jenn Lynch, Jiaming Liang, David Minkoff, Frank Moscatelli, Saurav Pathak, Soren Konecky, Alper Corlu, Jonathan Fisher, Kijoon Lee, Hsing-Wen Wang, Ellen Foster, Steve Schenkel, and Tiffany Averna.

And finally, for any future graduate students reading this dissertation: when pursuing your degree, I highly recommend getting a pet or two. Or maybe three… Nothing is better than a puppy who greets you at the end of a long day in lab with a full body wiggle and a smile from ear to ear. Or kitties who snuggle on your lap while you work late nights at home (Boo actually has me trapped at the moment as I'm typing). Betty, Boo, and Mustache have provided me with unconditional love over the past six years, and for that I am forever grateful.

ABSTRACT

CEREBRAL HEMODYNAMICS IN HIGH-RISK NEONATES PROBED BY DIFFUSE OPTICAL SPECTROSCOPIES

Erin McGuire Buckley

Supervisor: Arjun G. Yodh

Advances in medical and surgical care of the critically ill neonates have decreased mortality, yet a significant number of these neonates suffer from neurodevelopmental delays and failure in school. Thus, clinicians are now focusing on prevention of neurologic injury and improvement of neurocognitive outcome in these high-risk infants. Assessment of cerebral oxygenation, cerebral blood volume, and the regulation of cerebral blood flow (CBF) during the neonatal period is vital for evaluating brain health. Traditional CBF imaging methods fail, however, for both ethical and logistical reasons. In this dissertation, I demonstrate the use of non-invasive optical modalities, i.e., diffuse optical spectroscopy and diffuse correlation spectroscopy, to study cerebral oxygenation and cerebral blood flow in the critically ill neonatal population. The optical techniques utilize near-infrared (NIR) light to probe the static and dynamic physiological properties of deep tissues. Diffuse correlation spectroscopy (DCS) employs the transport of temporal correlation functions of diffusing light to extract relative changes in blood flow in biological tissues. Diffuse optical spectroscopy (DOS) employs the wavelength-

dependent attenuation of NIR light to assess the concentrations of the primary chromophores in the tissue, namely oxy- and deoxy-hemoglobin. This dissertation presents both validation and clinical applications of novel diffuse optical spectroscopies in two specific critically ill neonatal populations: very-low birth weight preterm infants, and infants born with complex congenital heart defects.

For validation of DCS in neonates, the blood flow index quantified by DCS is shown to correlate well with velocity measurements in the middle cerebral artery acquired by transcranial Doppler ultrasound. In patients with congenital heart defects DCS-measured relative changes in CBF due to hypercapnia agree strongly with relative changes in blood flow in the jugular veins as measured by phase-encoded velocity mapping magnetic resonance. For applications in the clinic, $CO_2$ reactivity in patients with congenital heart defects prior to various stages of reconstructive surgery was quantified; our initial results suggest that $CO_2$ reactivity is not systematically related to brain injury in this population. Additionally, the cerebral effects of various interventions, such as blood transfusion and sodium bicarbonate infusion, were investigated. In preterm infants, monitoring with DCS reveals a resilience of these patients to maintain constant CBF during a small postural manipulation.

## Table of Contents

## List of Abbreviations

| | |
|---|---|
| ASL-pMRI | Arterial spin labeled perfusion MRI |
| APD | Avalanche photodiode |
| ADC | Analog to digital converter |
| ADHD | Attention deficit/hyperactivity disorder |
| BFI | Blood flow index |
| BF | Blood flow |
| CBF | Cerebral blood flow |
| CHD | Congenital heart defect |
| CBFV | Cerebral blood flow velocity |
| $C_{Hb}$ | Concentration of deoxy-hemoglobin |
| $C_{HbO2}$ | Concentration of oxy-hemoglobin |
| CBV | Cerebral blood volume |
| CW | Continuous wave |
| $CMRO_2$ | Cerebral metabolic rate of oxygen extraction |
| $CO_2$ | Carbon dioxide |
| CHOP | Children's Hospital of Philadelphia |
| CVR | Cerebrovascular resistance |
| CSF | Cerebrospinal fluid |
| CCC | Concordance correlation coefficient |
| CI | Confidence interval |
| CICU | Cardiac intensive care unit |
| CE US | Contrast enhanced ultrasound |
| DWI | Diffusion weighted imaging |
| DSC | Dynamic susceptibility contrast |
| DOS | Diffuse optical spectroscopy |
| DCS | Diffuse correlation spectroscopy |
| DPDW | Diffuse photon density wave |

| | |
|---|---|
| DWS | Diffusing wave spectroscopy |
| EEG | Electroencephalography |
| EDV | End diastolic velocity |
| $FiO_2$ | Fraction of inspired oxygen |
| $FiCO_2$ | Fraction of inspired carbon dioxide |
| Hb | Deoxy-hemoglobin |
| $HbO_2$ | Oxy-hemoglobin |
| HOB | Head of bed |
| HLHS | Hypoplastic left heart syndrome |
| IVH | Intraventricular hemorrhage |
| I/Q | In phase/In quadrature |
| IQR | Interquartile range |
| LPF | Low pass filter |
| MRI | Magnetic resonance imaging |
| MV | Mean velocity |
| MBL law | Modified Beer-Lambert law |
| NIRS | Near infrared spectroscopy |
| NIM bin | Nuclear instrumentation bin |
| NIR | Near infrared |
| OD | Optical density |
| PVL | Periventricular leukomalacia |
| PET | Positron emission tomography |
| PSV | Peak systolic velocity |

| | |
|---|---|
| PMT | Photomultiplier tube |
| PSD | Phase sensitive detector |
| $pCO_2$ | Partial pressure of carbon dioxide |
| | |
| RI | Resistance index |
| RTE | Radiative transport equation |
| RF | Radio frequency |
| rBF | Relative change in blood flow |
| rCBF | Relative change in cerebral blood flow |
| rCBV | Relative change in cerebral blood volume |
| $rCMRO_2$ | Relative change in cerebral metabolic rate of oxygen extraction |
| | |
| SNR | Signal to noise ration |
| $SpO_2$ | Transcutaneous oxygen saturation |
| $SaO_2$ | Arterial oxygen saturation |
| $StO_2$ | Tissue oxygen saturation |
| $ScO_2$ | Cerebral oxygen saturation |
| | |
| TCD | Transcranial Doppler ultrasound |
| THC | Total hemoglobin concentration |
| | |
| US | Ultrasound |
| | |
| VENC MRI | Phase encoded velocity mapping MRI |

## List of Tables

## List of Illustrations

# 1 Introduction

This introductory chapter summarizes current neuromonitoring techniques available for use with critically ill neonates. The chapter also highlights the need for a non-invasive bedside monitor of cerebral hemodynamics in high-risk neonates. Of course, I am proposing (and demonstrating) that diffuse optical spectroscopies offer unique tools to fill important niches for monitoring newborn infants.

## 1.1 Critically-Ill Neonates

Two populations of neonates are investigated in this dissertation. This section briefly summarizes the reasons these infants should be studied and it motivates the need for bedside monitoring of cerebral hemodynamics in these populations. An in-depth discussion of these patients can be found in Chapters 5 and 6.

### 1.1.1 Motivation Studies of Preterm Infants

Between 1990 and 2005 the percentage of preterm births in the United States rose by 20% [1]. Preterm births now account for almost half of children with cerebral palsy, as well as a significant portion of children with cognitive, visual, and hearing impairments. Three forms of acquired brain injury affect the likelihood of mortality and neurodevelopmental deficits in very low birth weight (< 1500 g), very preterm (< 32 weeks gestation age) neonates: hypoxic-ischemic insult, periventricular leukomalacia (PVL), and intraventricular hemorrhage (IVH) [2, 3]. PVL is a specific form of necrosis of

the cerebral white matter adjacent to the lateral ventricles that is often associated with impaired motor development and is a major cause of cerebral palsy. During the early stages of brain development, this region of white matter is highly susceptible to injury from lack of blood flow and oxygen delivery, due to the maturation stage of the supporting cells (oligodendrocytes) [4]. IVH refers to hemorrhaging from the germinal matrix, an immature bed of vascular tissue along the ventricular wall that is typically present only in preterm infants less than 32 weeks gestation age. Such hemorrhages are caused by fluctuations in cerebral blood flow (CBF) and may induce profound cognitive and physical handicaps. A continuous monitor of cerebral hemodynamics (both cerebral blood flow and cerebral oxygenation) at the bedside could therefore be a valuable supplement for gathering information about a patient's condition [5] and for guiding treatment.

### 1.1.2 Motivation for Studies of Neonates with Congenital Heart Defects

Approximately 35,000 infants are diagnosed yearly with congenital heart defects (CHD) [6]. A third of these infants will have severe, complex cardiac lesions that will require surgical repair in the first few months of life. Importantly, cardiac surgery for serious forms of CHD in the neonatal period has progressed to the point wherein mortality is minimal. However, these patients have a high risk of stroke, seizure, hemorrhages, and periventricular leukomalacia. At school age, these patients are at higher risk for impaired cognitive and fine motor skills, learning and speech problems, attention deficit/hyperactivity disorder (ADHD), and potentially lower IQ than the general population [7-10]. Thus, clinicians are now focusing on prevention of neurologic injury and improvement of neurocognitive outcome in these high-risk infants. Therefore, as

was the case for preterm infants, a continuous monitor of cerebral blood flow and cerebral oxygenation at the bedside could be a valuable supplement for gathering information about a patient's condition [5] and for predicting and possibly preventing brain injury.

## 1.2 Current Neuromonitoring Techniques for Critically-Ill Neonates

Herein I highlight neuromonitoring techniques used most frequently in neonates: magnetic resonance imaging (MRI), transcranial Doppler ultrasound (TCD), positron emission tomography (PET), electroencephalography (EEG), radioactive tracers such as Xenon-133, and near-infrared spectroscopy (NIRS). A brief overview of each technique is presented, and a discussion of the advantages and disadvantages of each method for use in neonates is given. Table 1 summarizes the pertinent characteristics of each of these techniques. For further review/reference, Wintermark *et al* [11] published an

| | MRI | TCD | PET | EEG | Xe-133 | NIRS |
|---|---|---|---|---|---|---|
| Spatial Resolution | ~2 mm | N/A | 4-6 mm | N/A | Whole brain | ~10 mm |
| Brain Coverage | Whole | One per hemisphere | Whole | Whole | Whole | Few per hemisphere |
| Cost | High | Low | High | Low | Low | Low |
| Bedside (Portable) | No | Yes | No | Yes | Yes | Yes |
| Ionizing Radiation | No | No | Yes | No | Yes | No |
| Acquisition Time | 1-10 min | 10-20 min | 5-10 min | < 1 ms | 10-20 min | 1 ms -1 s |
| Continuous | No | No | No | Yes | No | Yes |
| Parameters Measured | Anatomy, water diffusion, CBF | CBFV | CBF, CBV, $CMRO_2$ | Electrical Activity | CBF | $ScO_2$, CBV |
| Contrast Agent | No | No | Yes | No | Yes | No |

Table 1, Summary of the current neuromonitoring techniques employed in neonates: CBF = Cerebral blood flow, CBFV = cerebral blood flow velocity, $CMRO_2$ = cerebral metabolic rate of oxygen extraction, $ScO_2$ = cerebral oxygen saturation, CBV = cerebral blood volume.

excellent overview of the majority of these techniques as they are used in man. The majority of this section is derived from this review.

### 1.2.1 Magnetic Resonance Imaging (MRI)

MRI is an invaluable tool for studying the brain. It provides high-resolution images of both cerebral anatomy and perfusion. However, MRI only reflects physiology at a discrete time point and cannot be used at the bedside or in the operating room for longer periods of assessment.

*Structural/Dynamical Neuroimaging*

MRI provides many pulse sequences capable of rendering structural images of the brain. Three-dimensional volumetric MRI quantifies volumes of grey matter, white matter, and cerebrospinal fluid, as well as total brain volume [12-14]. Extensive MRI research has demonstrated post-natal progression of these parameters in neonates [12, 15] (i.e., increases in myelination, increases in total brain volume, grey matter volume, etc.). Thus, volumetric MRI may be used to assess brain development of the critically ill neonate as compared to a cohort of healthy “normal” neonates.

A complimentary technique to structural scans, which reveal brain anatomy and volume, is MR diffusion-weighted imaging (DWI) which quantifies water diffusion in the neonatal brain [16]. The natural progression of the average water diffusion coefficient as well as the relative anisotropy of water diffusion (caused by both changes in water content of the brain, as well as changes in tissue microstructure) is well known in healthy brain development. Thus, DWI can be used as a tool to assess brain maturation, as well as to diagnosis brain injuries such as stroke and periventricular leukomalacia (PVL) [17].

In addition to water diffusion, cerebral perfusion may be assessed using dynamic susceptibility contrast (DSC) (see review in [18] for a detailed description of the technique). In DSC, an exogenous MRI tracer such as gadolinium is used to qualify regional cerebral blood volume based on the theory of tracer kinetics, i.e., the indicator dilution method [19]. DSC requires a relatively short imaging duration and the image processing tools are widely available. Although the technique is not quantitative, it can evaluate regional differences in cerebral blood volume, which is helpful in the identification and classification of brain tumors. However, its use in pediatrics has been limited by the need to use gadolinium contrast boluses, by the inability to make repeated measurements during a single session (secondary to cumulative effects), and by the lack of absolute quantification of blood volume [18].

A novel technique, arterial spin labeled perfusion MRI (ASL-pMRI), permits noninvasive evaluation of quantitative CBF images using electromagnetically labeled arterial blood water as an endogenous contrast agent [20-23]. One of the most significant advantages of ASL-pMRI over previous techniques is the ability to assess cerebral blood flow (CBF) without using intravascular contrast agents or radioactive labeled tracers. Measuring CBF with ASL in neonates and infants, however, poses technical challenges related to their cerebrovascular physiology. First, CBF in infants is lower than that of older children and adults. Second, the longitudinal relaxation time of blood (i.e., the time it takes for magnetically labeled blood to realign with the external magnetic field) is relatively long [21]. This combination of factors produces contaminated control images, culminating in a concentration of “negative voxels” on the final CBF map. The percentage of negative “voxels” increases as CBF decreases, and is the leading contributor to noise in ASL-MRI.

High-risk neonates have inherently low CBF [24-26]. Imaging at high field (3.0 vs. 1.5 Tesla), reducing the labeling volume, and improving tagging efficiency provides more reliable CBF maps by reducing the percentage negative voxels (SNR). Studies in normal neonates using ASL-pMRI have catalogued normal CBF in preterm- and term-infants [27], as well as age related changes throughout childhood [28]. Other studies have demonstrated expected physiological responses; for example, CBF increases with lower hemoglobin and increases predictably with hypercarbia [26]. ASL-pMRI has also been useful in assessing CBF in neonates who have suffered hypoxia-ischemia [29] and in infants and children after stroke [30].

### 1.2.2 Transcranial Doppler Ultrasound (TCD)

Other than NIRS (discussed below), ultrasound is the most convenient form of cerebral hemodynamic monitoring in critically ill neonates due to its portability. TCD measures cerebral blood flow *velocity* (CBFV) in the large cerebral arteries by monitoring the frequency shift of acoustic waves that scatter from moving red blood cells [31]. Traditionally, perfusion in the middle cerebral, anterior cerebral, and/or internal carotid arteries is monitored to assess global brain perfusion. The parameters measured with TCD include peak systolic, mean, and end diastolic velocities (i.e., PSV, MV, and EDV, respectively). The angle of isonation used to measure velocities with TCD may affect the values of PSV and EDV; thus, a resistance index (RI) is often employed as a way to eliminate the effects of the angle of probe placement [32]:

$$RI = \frac{PSV - EDV}{PSV}. \qquad [1]$$

RI is a unitless parameter that reflects cerebrovascular resistance. The natural

progression of changes in PSV, EDV, MV, and RI after birth in healthy infants has been well documented [33-35].

With additional information about the cross-sectional area ($A$) of the insonated vessel, CBFV permits calculations of arterial CBF using the formula $CBF = CBFV \times A$. However, cerebral vessels are small in size, making their diameter difficult to measure [36]. To avoid this source of error, one could focus on relative changes in flow. However, these blood vessels can change caliber over time, leading to large errors in calculations of relative change, which in turn cause errors in estimates of the amount of oxygen and nutrients delivered to the surrounding tissue [37-39]. Additionally, TCD measures cerebral blood flow/blood flow velocity in the large vessels that supply perfusion to the brain; however, regional variations in cerebral blood flow are not accessible with TCD.

### 1.2.3 Electroencephalography (EEG)

EEG is a non-invasive technique for monitoring electrical activity (*not* hemodynamics) in brain, generated by neuronal activity. Electrodes are secured to the scalp and the resultant electrical signal is monitored over time. Although the technique requires skilled clinicians/technicians for interpretation of electrical activity, EEG is a relatively inexpensive modality capable of continuous bedside neurological monitoring. It is currently the gold standard for diagnosing seizures in neonates, which may be linked to poor neurodevelopmental outcome [40]. Additionally, the normal progression with age of spontaneous EEG recorded activity is well known for healthy neonates and for infants born prematurely [41]. This evolution of EEG activity changes dramatically over the first weeks of life. Thus, abnormalities in the electroencephalogram readings as compared to those of age-matched healthy infants may be indicative of acute or chronic brain injury

and/or poor neurodevelopment [42].

### 1.2.4 Positron Emission Tomography (PET)

PET provides quantitative tomographic images of regional cerebral blood flow, regional cerebral blood volume, regional oxygen extraction fraction, and regional cerebral metabolic rate of oxygen extraction [43, 44]. The technique is quantitative (with a resolution of approximately 5 mm) and reproducible; however, PET requires either the intravenous administration or the inhalation of positron emitting radioisotopes, it exposes the patient to radiation, and it works only under steady-state hemodynamic conditions. Very little work has been done with PET in neonates [45-48], presumably due to ethical considerations, need for patient transport, need for anesthesia, etc.

### 1.2.5 Radioactive Tracers

A great deal of what we know about cerebral blood flow in babies comes from research conducted using inert gas radiopharmaceutical tracers, such as $^{133}$Xe; however, the technique is not typically employed in neonates in the present day due to exposure to ionizing radiation. In practice, $^{133}$Xe dissolved in saline is injected into a peripheral artery or vein, and scintillation detector(s) are placed over the brain to monitor gamma radiation during $^{133}$Xe uptake and clearance. The time trace of the count rate of gamma radiation can be related to cerebral blood flow via the Fick principle [32, 49-52].

This technique, while providing absolute measures of cerebral blood flow in a reliable fashion, exposes the patient to small amounts of ionizing radiation and thus cannot be repeated too frequently. Additionally, the Fick principle assumes constant and homogeneous cerebral blood flow during the entire course of data acquisition

(approximately 10-15 minutes). Thus, measurements using $^{133}Xe$ may be subject to error if the patient's cerebral blood flow is not in a steady-state or if the patient has regions of extremely heterogeneous flow [50].

### 1.2.6 Near-Infrared Spectroscopy (NIRS)

Commercially available NIRS instruments from companies, such as Hamamatsu, Somanetics, and NIRx Medical Technologies, are becoming prevalent as standard of care for cerebral monitoring in neonatal intensive care units and operating rooms across the country [53]. NIRS continuously monitors attenuation of continuous wave NIR light incident on the tissue surface. This attenuation enables experimenters to extract changes in the light absorption properties of the tissue via the modified Beer-Lambert law (see Section 2.1.5). Changes in the absorption coefficient of tissue ($\Delta\mu_a$) relative to a presumed baseline period of measurement are related to changes in chromophore concentrations. These concentrations are obtained using the following formula:

$$\Delta\mu_a(\lambda) = \sum_i \epsilon_i(\lambda)\Delta C_i, \qquad [2]$$

where $\epsilon_i$ [μM • $cm^{-1}$] is the known wavelength dependent extinction coefficient of the $i^{th}$ chromophore, and $\Delta C_i$ [μM] is the change in the $i^{th}$ chromophore concentration. The two main endogenous absorbers in tissue in the NIR spectral range are oxy- and deoxy-hemoglobin ($HbO_2$ and Hb, respectively), thus Equation 2 is typically written as $\Delta\mu_a(\lambda) = \Delta C_{Hb}\epsilon_{Hb}(\lambda) + \Delta C_{HbO_2}\epsilon_{HbO_2}(\lambda)$, where $\Delta C_{Hb}$ and $\Delta C_{HbO_2}$ are the changes in concentrations of tissue oxy- and deoxy-hemoglobin, respectively. After $\Delta\mu_a$ is obtained at multiple wavelengths, quantifying hemoglobin concentration changes only requires solving a system of linear equations.

These commercially available instruments assume baseline values of oxy- and deoxy-hemoglobin concentrations and compute changes in tissue oxygen saturation and changes in cerebral blood volume. With the help of an exogenous tracer, such as oxygen or indocyanine green dye, NIRS can also provide quantification of CBF [mL/min/100 g]. This calculation of CBF again relies on the Fick principle, which states that the total uptake of a tracer by tissue is proportional to the difference between the rates of inflow and outflow of the tracer to and from the tissue. This measurement provides a snapshot of regional tissue CBF in time; however, it does not provide continuous CBF data. Furthermore, a few assumptions must be true for this method to be valid: CBV, CBF, and cerebral oxygen extraction must remain constant during the measurement. This technique has been validated with limited success [54, 55]. The use of an exogenous tracer limits its use in the clinical setting, especially in high-risk neonates.

Commercial NIRS devices used in the clinic are highly sensitive to stray room light, to surface coupling between skin and/or hair and the optical probe, and lead to crosstalk between calculated tissue absorption and scattering [56, 57]. In addition, although reliable trends in hemodynamic changes may be obtained with these devices, accurate calculations of relative changes in chromophore concentrations are often highly influenced by the aforementioned factors. Commercial system availability is crucial for wider use of NIRS in the clinic, and there now exist a handful of CW NIRS devices approved by the Food and Drug Administration [53]. The clinical utility of these devices is promising but remains to be determined by large clinical trials.

## 1.3 Diffuse Optical and Diffuse Correlation Spectroscopies

As the previous section suggests, a handful of techniques are currently used to study cerebral hemodynamics in neonates. However, all of these techniques have pitfalls. MRI and PET are both expensive, require patient transport, and provide snapshots of hemodynamics in time as opposed to continuous monitoring; TCD only looks at the macrovasculature; EEG only provides information on electrical activity; and NIRS only works as a trend monitor of cerebral oxygenation (e.g., as opposed to providing quantitative absolute oxygenation levels or cerebral blood flow measurements).

I believe that NIRS holds promise as an extremely valuable measurement tool in neonates. However, commercial systems lack the ability to provide truly quantitative results, and they ignore the wealth of knowledge now available about the propagation of light in tissue. In this dissertation, I distinguish NIRS from Diffuse Optical Spectroscopy (DOS). Like NIRS, DOS aims to investigate tissue physiology millimeters to centimeters below the tissue surface by using the spectral "window" of low absorption in the near-infrared range (NIR, 700-900 nm). However, unlike NIRS, DOS utilizes photon diffusion theory to extract more rigorous information about both optical absorption and scattering within the tissue based on light attenuation at the tissue surface. DOS measures slow variations in cerebral absorption and scattering and is sensitive to *absolute* chromophore concentrations and therefore to *absolute* measures of cerebral oxygen saturation and cerebral blood volume (CBV).

Furthermore, DOS (or NIRS) measurements can be greatly enhanced by the addition of an independent monitor of cerebral blood flow. This dissertation focuses on the combination of DOS with a novel optical method, diffuse correlation spectroscopy (DCS), which measures changes in cerebral blood flow by monitoring the temporal

intensity autocorrelation function of diffusing light at the tissue surface. DCS is ideal for the critically ill neonate population; it can be used as a continuous, noninvasive, low-risk, readily portable bedside monitor of relative changes in regional cortical CBF. Additionally, DCS can easily be combined with other modalities, such as NIRS, Doppler ultrasound, or electroencephalography, to enhance the information gathered by other techniques about the patient's physiology. Few studies have been conducted with DCS on this population, largely because of the newness of the technology [58-60]. Ideally, a study would use a hybrid DOS and/or DCS instrument [59, 61-64] to capture both tissue oxygenation and blood flow changes. These two parameters combined enable construction of indices for measuring cerebral metabolic rate of oxygen extraction ($CMRO_2$) [62, 63].

## 1.4 Summary

Critically ill neonates are a unique population that could benefit from continuous bedside monitoring of cerebral hemodynamics to identify and potentially prevent detrimental cerebral events such as hypoxic ischemia, hemorrhage, stroke, etc. It appears that diffuse optical techniques may be well suited for monitoring this unique population. This dissertation will describe the theory behind diffuse optical spectroscopies in depth, it will discuss the instrumentation requirements for bedside monitoring, it will report on numerous validation studies performed on both preterm infants and on infants with congenital heart defects, and finally, it will highlight clinical applications of the technique with the ultimate goal of improving patient care and further understanding the complexities of the hemodynamics in the neonatal brain.

Chapters 2 and 3 review the diffuse optical techniques, namely diffuse optical

spectroscopy (DOS) and diffuse correlation spectroscopy (DCS), that are applied for neonatal neuromonitoring in the remainder of this dissertation. An effort is made to gear the theory towards that which is applicable only to these infants. Thus, the intricacies of tomographic reconstructions, etc. are not included in these chapters. These chapters highlight the relevant theory behind the spectroscopic measurements made on neonates. Chapter 4 describes, in depth, the hybrid DOS/DCS instrumentation needed to make DOS/DCS measurements.

Chapter 5 presents published validation studies of DCS in two separate pediatric populations, namely patients with congenital heart defects and preterm infants. First, during a hypercapnia intervention in children with congenital heart defects, changes in cerebral blood flow measured with DCS are shown to agree well with relative changes in blood flow in the jugular veins. Second, in preterm infants, I demonstrate a strong correlation between the absolute blood flow index quantified by DCS and blood flow velocity measurements. In patients with congenital heart defects DCS relative changes in CBF occurring due to hypercapnia agree strongly with relative changes in blood flow in the jugular veins as measured by phase-encoded velocity mapping magnetic resonance.

The last chapter (Chapter 6) highlights the translation of the DOS/DCS techniques to the intensive care unit for bedside monitoring. I focus on a collection of data obtained from infants with congenital heart defects. The chapter quantifies the cerebral effects of various interventions, namely hypercapnia, blood transfusion, and sodium bicarbonate infusion, and it also studies the evolution of cerebral oxygen saturation, total hemoglobin concentration, and reduced scattering coefficient before and after cardiac surgery.

Finally, the majority of this dissertation focuses on my work monitoring pediatric patients. I note here that I have spent a significant amount of time in collaborations with other lab members that have led to published results. I am co-author on other publications involving cerebral blood flow in adult patients with traumatic brain injury [65], and hypercapnia in neonates with congenital heart defects [59]. Additionally, I contributed heavily to the review of optical techniques in a recent review paper on perfusion imaging in the high-risk neonate by Goff *et al* [20].

# 2 Diffuse Optical Spectroscopy

The goal of diffuse optical spectroscopy (DOS) is to measure tissue chromophore concentrations (oxy-hemoglobin, deoxy-hemoglobin, water, lipids, etc.) and scattering in deep tissue, i.e., on depth scales on the order of centimeters below the tissue surface. DOS measures chromophore concentrations by taking advantage of a spectral "window" in the near-infrared (NIR) within which the absorption of light is quite low; in this spectral regime, photons experience many multiple scattering events before absorption or re-emission at the tissue surface. An example of the absorption spectra of the three main chromophores in biological tissue is seen in Figure 1. The optical absorption coefficient, $\mu_a$ defined as the inverse of the distance a photon travels before it is likely to experience an absorption event (i.e., the 1/e distance), is shown on the vertical-axis and is plotted versus the wavelength of light for oxy-hemoglobin, deoxy-hemoglobin, and water. It is evident from this figure that, outside of the NIR range of approximately 680-900 nm, the

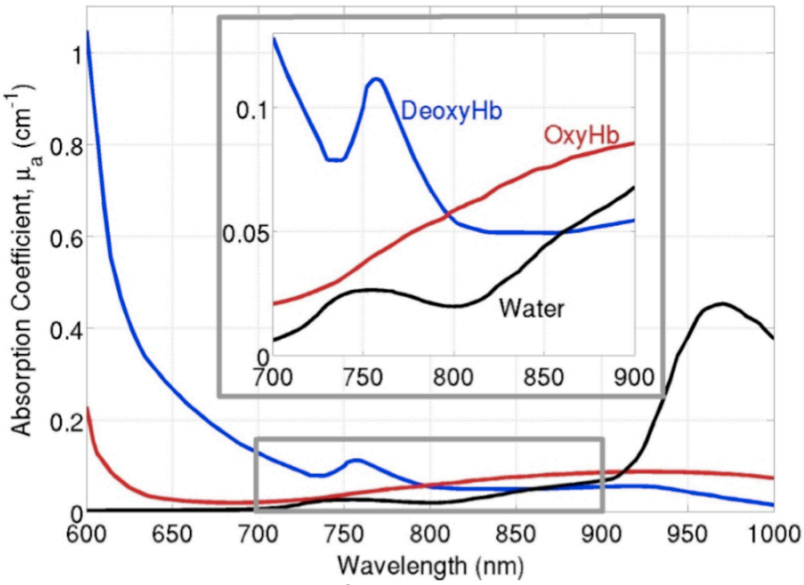


Figure 1, Sample absorption spectrum of oxy-hemoglobin, deoxy-hemoglobin, and water in tissue. A spectral "window" exists in the near-infrared range (highlighted in the gray box and enlarged above), so that scattering, rather than absorption, dominates photon propagation.

tissue absorption coefficient is high and light cannot penetrate deeply. Furthermore, within the NIR range, shown in the inset of Figure 1, the absorption coefficient is not only low, but one can also observe distinct spectral features due to each chromophore. Thus, measurement of this absorption coefficient at multiple wavelengths can provide enough information so that the concentrations of the various chromophores in the tissue can be calculated.

The analysis, however, must account for the fact that light undergoes a large number of scattering events before reaching the boundaries of the medium, and therefore the input photons will travel along a distribution of pathlengths from source to detector (as opposed to say x-ray computed tomography in which light travels straight through the medium). This chapter will discuss in detail how one separates tissue absorption from scattering in the NIR window. As the chapter title suggests, the focus here will be on spectroscopy, which aims to measure the mean bulk chromophore concentrations over a large tissue volume, as opposed to imaging, which attempts to assign this information to many volume elements within the tissue sample. Additionally, the instrumentation required to make physiological spectroscopic measurements will be discussed.

## 2.1 Photon Diffusion Equation

NIR light propagation in a highly scattering medium such as biological tissue is well modeled as a random walk process. Interference effects are usually negligible (except for the famous backscattering cone [66]), and the light trajectories are fairly accurately visualized using ray optics. It is not necessary to deal with Maxwell's equations. Thus, the starting point for most analyses of these problems is the radiation transport equation

(RTE) that describes the conservation of light radiance, $L(\boldsymbol{r}, \hat{s}, t)$ [67]:

$$\frac{1}{\nu}\frac{\partial \mathrm{L}(\mathbf{r},\hat{s},t)}{\partial t} + \hat{s}\cdot\nabla \mathrm{L}(\mathbf{r},\hat{s},t) = -\mu_t \mathrm{L}(\mathbf{r},\hat{s},t) + \mathrm{S}(\mathbf{r},\hat{s},t) + \mu_s \int \mathrm{L}(\mathbf{r},\hat{\mathrm{s}},t) f(\hat{s},\hat{s}')ds' \ . \quad [3]$$

Here the radiance [W/cm$^2$/sr] is defined as the power of light per unit area traveling in a given direction $\hat{s}$ within some infinitesimal volume element located around position $\boldsymbol{r}$ at time $t$; $\nu$ is the speed of light in the medium; $\mu_t$ is the sum of the absorption and scattering coefficients ($\mu_a$ and $\mu_s$, respectively) within the volume; $\mathrm{S}(\mathbf{r},\hat{s},t)$ is the power per volume emitted by sources into the direction $\hat{s}$; and $f(\hat{s},\hat{s}')$ is the normalized differential scattering cross-section that gives the probability that light (radiance) incident on a volume element will scatter from the $\hat{s}'$ direction into the $\hat{s}$ direction. I also define two additional quantities of interest: the photon fluence rate, $\Phi(\boldsymbol{r}, t)$ [W/cm$^2$], and the photon flux, $\boldsymbol{J}(\boldsymbol{r}, t)$ [W/cm$^2$].

$$\phi(\mathbf{r},t) = \iint L(\boldsymbol{r},\hat{s},t)d\hat{s}; \quad [4]$$

$$\boldsymbol{J}(\mathbf{r},t) = \iint L(\boldsymbol{r},\hat{s},t)\hat{s}d\hat{s}. \quad [5]$$

$\Phi(\boldsymbol{r}, t)$ is the total power per area traveling radially out of an infinitesimal volume element located around position $\boldsymbol{r}$ (at time $t$). $\boldsymbol{J}(\boldsymbol{r}, t)$ is the vector sum of the radiance emerging from this infinitesimal volume.

The RTE is quite difficult to solve analytically. Thus, in order to obtain an approximate analytical solution, the radiance and source terms are typically expanded in terms of spherical harmonics, $Y_{\ell,m}(\hat{s})$, i.e.,

$$\mathrm{L}(\mathbf{r},\hat{s},t) = \sum_{\ell=0}^{N}\sum_{m=-\ell}^{\ell} \Phi_{\ell,m}(\boldsymbol{r},t) Y_{\ell,m}(\hat{s}) \ , \quad [6]$$

$$\mathrm{S}(\mathbf{r},\hat{s},t)=\sum_{\ell=0}^{N}\sum_{m=-\ell}^{\ell}q_{\ell,m}(\boldsymbol{r},t)Y_{\ell,m}(\hat{s})\ , \qquad [7]$$

in what is known as the $P_N$ approximation. For this dissertation, we need only concern ourselves with the $P_1$ approximation, in which only the $\ell=0$ and $\ell=1$ terms are employed. Within this "nearly isotropic" approximation, the radiance is well approximated as the sum of an isotropic photon fluence rate and a small directional photon flux:

$$\mathrm{L}(\mathbf{r},\hat{s},t)=\frac{1}{4\pi}\Phi(\boldsymbol{r},t)+\frac{3}{4\pi}\boldsymbol{J}(\boldsymbol{r},t)\cdot\hat{s}. \qquad [8]$$

Here $\Phi(\boldsymbol{r},t)$ is proportional to $\Phi_{0,0}(\boldsymbol{r},t)$, and $\boldsymbol{J}(\boldsymbol{r},t)$ is proportional to the sum of the $\Phi_{1,m}(\boldsymbol{r},t)$ components of $L(\mathbf{r},\hat{s},t)$ [68, 69]. This approximation is valid when the radiance is nearly isotropic ($\phi \gg |\boldsymbol{J}|$).

Within the $P_1$ approximation (and under several other relatively innocuous assumptions[1]), the RTE is readily simplified to the photon diffusion equation for the fluence rate [68, 70-72]:

$$\nabla\cdot\big(D(\boldsymbol{r})\nabla\Phi(\boldsymbol{r},t)\big)-v\mu_a(\boldsymbol{r})\Phi(\boldsymbol{r},t)+vS(\boldsymbol{r},t)=\frac{\partial\Phi(\boldsymbol{r},t)}{\partial t}\ . \qquad [9]$$

Further, the fluence rate is related to the flux via Fick's law of diffusion:

$$\boldsymbol{J}(\boldsymbol{r},t)=-\frac{D}{v}\boldsymbol{\nabla}\Phi(\boldsymbol{r},t). \qquad [10]$$

---

[1] For this derivation, we assume 1. source isotropy, i.e., $S(\mathbf{r},\hat{s},t)=S(\boldsymbol{r},t)$; 2. slow temporal fluctuations of the photon flux, $\vec{J}(\boldsymbol{r},t)$, i.e., the photon flux varies slowly relative to the mean time between scattering events; 3. rotational symmetry, i.e., the scattering cross-section, $f(\hat{s},\hat{s}')$, depends only on the angle between the incident and outgoing scattering wavevectors, $f(\hat{s},\hat{s}')=f(\hat{s}\cdot\hat{s}')$.

Here $S(\boldsymbol{r},t)$ is now an isotropic source of photons traveling outward from a volume element located around position $\boldsymbol{r}$ at time $t$; $v$ is the speed of light in the medium [cm/s]; $\mu_a(\boldsymbol{r})$ and $\mu_s'(\boldsymbol{r})$ are the position dependent absorption coefficient and *reduced* scattering coefficients of the medium, respectively [cm$^{-1}$]. $D(\boldsymbol{r}) = v/3(\mu_s'(\boldsymbol{r}) + \mu_a(\boldsymbol{r})) \cong v/3\mu_s'(\boldsymbol{r})$ is the photon diffusion coefficient [cm$^2$/s] [73, 74]. Note that $\mu_s'(\boldsymbol{r})$ is different than $\mu_s$, i.e., $\mu_s'(\boldsymbol{r}) = \mu_s(1-g)$. Here, $g$ is the average of the cosine of the scattering angle for a typical scattering event, which is generally quite high for tissue (i.e., greater than 0.9); photons tend to scatter predominantly in the forward direction in tissue. Thus, a photon undergoes many single-scattering events (characterized by the scattering coefficient, $\mu_s$ ) in tissue before its initial direction is essentially randomized (characterized by the reduced scattering coefficient, $\mu_s'(\boldsymbol{r})$). The diffusion equation thus describes a situation wherein individual photon trajectories are random walks through the tissue. A photon, on average, travels a random walk step of length, $\ell_{tr} \equiv 1/\mu_s'$, before its direction is randomized. Photons diffuse through tissue in much the same way that ink diffuses through water.

In diffuse optical spectroscopy (DOS), tissue is usually modeled as a homogeneous medium, i.e., $D(\boldsymbol{r}) = D$, $\mu_s'(\boldsymbol{r}) = \mu_s'$ and $\mu_a(\boldsymbol{r}) = \mu_a$. $D$, $\mu_s'$, and $\mu_a$ are the average bulk optical properties of the tissue. These optical properties, of course, will change with light wavelength, but they are modeled as constants in space at each wavelength. Within this approximation, the diffusion equation simplifies even further, i.e.,

$$D\nabla^2\Phi(\boldsymbol{r},t) - v\mu_a\Phi(\boldsymbol{r},t) + vS(\boldsymbol{r},t) = \frac{\partial\Phi(\boldsymbol{r},t)}{\partial t}. \qquad [11]$$

Like the radiative transport equation, the photon diffusion equation is a conservation equation, in which the time rate of change in photon concentration in a given unit volume (right hand side) is equal to the number of photons emitted from the source in the volume ($\nu S(\boldsymbol{r},t)$) plus the photons scattered into the volume from the surroundings ($D\nabla^2\Phi(\boldsymbol{r},t)$) less the number of photons absorbed within the volume ($\nu\mu_a\Phi(\boldsymbol{r},t)$).

### 2.1.1 Source Types

As seen in Figure 2, there are three classes of sources employed for diffuse optical spectroscopy. For all source types, data are collected at multiple wavelengths, equal to or exceeding the number of chromophores measured [75]. Time-resolved DOS (Figure 2c) typically employs multiple NIR wavelength sources of sub-nanosecond pulsed light and measures photon arrival times of the reflected/transmitted diffuse light. This technique enables quantification of absolute optical properties using fits to the solution of the photon diffusion equation in the time-domain [76]. However, with the high information content of time-resolved measurements comes a high cost of instrumentation components, and a low duty cycle because the maximum count rate is on the order of 5 MHz.

Similar information, namely, absolute absorption and scattering coefficients at multiple wavelengths can be obtained in the frequency domain (Figure 2b). In this experimental configuration, NIR light sources are sinusoidally amplitude modulated in the ~100 MHz range [72, 77-79]. FD systems gather similar information as the time domain systems, as the techniques are Fourier analogs. Although the FD systems are not sensitive to stray room light, it can be sensitive to unwanted light that has leaked from the source around the sample of interest and to surface coupling between the skin

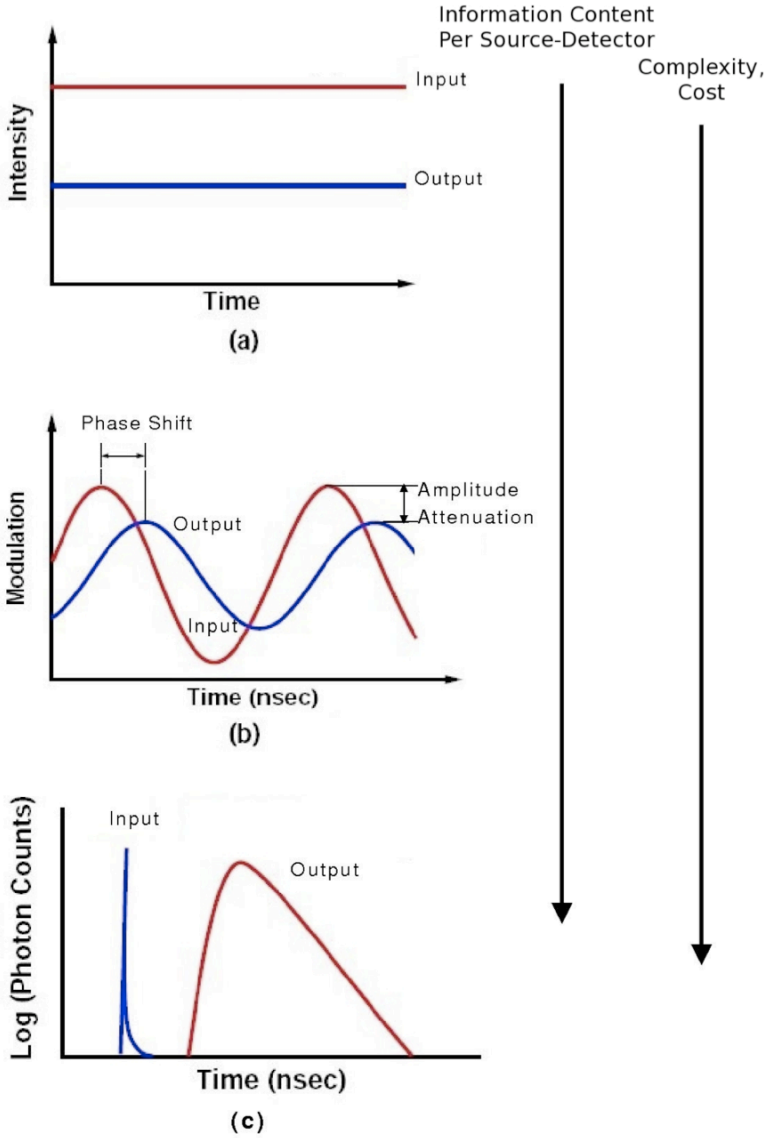


Figure 2, Graphical depiction of the three types of near infrared spectroscopy measurements (a) continuous wave, (b) frequency domain, (c) time resolved. The arrows on the right side of the figure indicate increasing data and instrumentation complexity (increasing corresponds to traveling "down" in the diagram) that accompany these techniques.

and optode [80].

Continuous wave (CW) systems measure the attenuation of constant intensity source light after it has diffused through the tissue. The CW setup offers a fast and inexpensive method for measuring relative changes in the optical properties of the

tissue; however, absorption and scattering cannot be distinguished uniquely by a single measurement.

In the studies conducted within this dissertation, the frequency domain is employed. Thus, the remainder of this section will focus on solutions of the photon diffusion equation assuming an isotropic point source at the origin whose intensity is sinusoidally modulated at angular frequency $\omega$, i.e., $S(\boldsymbol{r},t) = (S_{DC} + S_0 e^{-i\omega t})\delta(\boldsymbol{r}=0)$. Herein, we impose the restriction that $\omega/2\pi$ is much smaller than the typical frequency of the scattering events, $\nu\mu_s'$. With a source of this form, the fluence rate in the sample is also composed of an AC and DC component, $\Phi(\boldsymbol{r},t) \equiv \Phi_{DC}(\boldsymbol{r}) + \Phi(\boldsymbol{r})e^{-i\omega t}$. Examining only the AC component, the diffuse equation becomes:

$$D\nabla^2\Phi(\boldsymbol{r}) - \nu\mu_a\Phi(\boldsymbol{r}) + \nu S_0\delta(0) = -i\omega\Phi(\boldsymbol{r}). \quad [12]$$

This equation can be re-written as:

$$(\nabla^2 - k^2)\Phi(\boldsymbol{r}) = -\nu\, S_0/D\ \delta(0), \quad [13]$$

where $k^2 = (-i\omega + \nu\mu_a)/D$ and the right hand side of the equation equals 0 for all $\boldsymbol{r} \neq 0$. Isolating the DC component of $\Phi$ yields

$$D\nabla^2\Phi_{DC}(\boldsymbol{r}) - \nu\mu_a\Phi_{DC}(\boldsymbol{r}) + \nu S_{DC}\delta(0) = 0,$$

which simplifies to:

$$\left(\nabla^2 - {k_0}^2\right)\Phi(\boldsymbol{r}) = -\nu\, S_0/D\ \delta(0), \quad [14]$$

where ${k_0}^2 \equiv \nu\mu_a/D = 3\mu_a\mu_s'$. The remainder of this chapter will analytically solve these

equations to derive Helmholtz Equation-like solutions for two simple geometries relevant to the experiments we carry out.

### 2.1.2 Infinite Geometry

For the case of a point source located at the origin surrounded by a homogeneous infinite medium, the main boundary condition is that the fluence rate falls to zero as $r$ approaches infinity. The solution to Equation 14, given these boundary conditions, is the well known spherical wave:

$$\Phi(\boldsymbol{r}) = \frac{\nu S_0}{4\pi D}\frac{\mathrm{e}^{-\mathrm{kr}}}{r}. \qquad [15]$$

Actually, the solution is in the form of a damped traveling spherical wave. This wave, dubbed a diffuse photon density wave (DPDW), travels with a coherent front and has complex wave vector $k = k_r + ik_i = \sqrt{(\nu\mu_a - i\omega)/D}$ . The real and imaginary components of the wave vector can be written as:

$$k_r = \sqrt{\frac{\nu\mu_a}{2D}}\left[\sqrt{1+\left(\frac{\omega}{\nu\mu_a}\right)^2}+1\right]^{1/2} \qquad [16]$$

$$k_i = -\sqrt{\frac{\nu\mu_a}{2D}}\left[\sqrt{1+\left(\frac{\omega}{\nu\mu_a}\right)^2}-1\right]^{1/2} \qquad [17]$$

The DPDW consists of two main parts, a *phase-shift* term, $\mathrm{e}^{-\mathrm{ik_i r}}/r$, and an *attenuation* term, $\mathrm{e}^{-\mathrm{k_r r}}$. It has position-dependent amplitude, $A = \nu S_0 \mathrm{e}^{-\mathrm{k_r r}}/(4\pi D r)$, and phase, $\theta = k_i r$. The DPDW can thus be characterized by a wavelength, $\lambda$, phase velocity, $v_p$, and decay attenuation length, $L_d$:

$$\lambda = \frac{2\pi}{k_i}, \quad [18]$$

$$v_p = \frac{\omega}{k_i}, \quad [19]$$

$$L_d = \frac{1}{k_r}. \quad [20]$$

Note that all of these parameters depend on $\omega$, $\mu_a$, $\mu_s'$, and the speed of light in the medium, $v$. For typical human brain, approximate optical properties are $\mu_a = 0.1$, $\mu_s' = 10$ at 785nm; thus, with a frequency modulated source of 70 MHz, the DPDW "phase" wavelength is $\sim 35$ cm, which is almost 30 times greater than its attenuation length of 1.1 cm; the wave has a phase velocity of $2.5\times10^7$ m/s. It has been shown that DPDWs behave in many (but not all) [67] ways like traditional travelling waves, i.e., they exhibit reflection, refraction, diffraction/scattering, dispersion, and interference phenomenology [81-85].

### 2.1.3 Semi-Infinite Geometry

A remission geometry in which the source and detector fibers are placed on the $z = 0$ plane at an air-tissue interface is a more suitable (and non-invasive) model for clinical settings, albeit still quite simplistic. In this case, the medium is assumed to be optically homogeneous and to extend infinitely in the x-y plane and the positive $\hat{z}$-direction (see Figure 3); further we choose the incident beam to be located at the origin and directed in the positive $\hat{z}$-direction.

If the boundary is perfectly transmitting (i.e., the index of refraction of both media are matched), then the radiance must be zero when the $\hat{s}$-direction points into the

medium from outside (i.e., there is no reflection of diffuse light back into the medium), i.e., the total incoming diffuse radiance, $\mathrm{E}_{in}(z=0,t)$, is:

$$\mathrm{E}_{in}(z=0,t) = \int_0^{2\pi}\int_0^{\pi/2} L(z=0,\hat{s},t)\,(\hat{s}\cdot -\hat{n})\ \sin\theta\, d\theta d\phi = 0\ . \qquad [21]$$

Substituting in the P1 approximation for $L(z=0,\hat{s},t)$ and integrating, we find:

$$\mathrm{E}_{in}(z=0,t) = \frac{\phi(z=0,t)}{4} + \frac{J_z(z=0,t)}{2} = 0. \qquad [22]$$

Then, employing Fick's law for diffusion (Equation 10), we obtain what is known as the partial-current (or partial-flux) boundary condition for a perfectly transmitting boundary:

$$\phi(z=0,t) = \frac{2}{3\mu_s'}\frac{\partial\phi}{\partial z}\Big|_{z=0}. \qquad [23]$$

In addition to the boundary condition, we need to characterize our source term in order to solve the diffusion equation for this geometry. In a typical experiment, the output of a fiber or a similarly "tight" collimated beam is placed on the air/tissue interface (see Figure 3); a standard approach adopted by most researchers is to approximate the real source with an "isotropic" source at a new position located a distance $\ell_{tr}$ inside the

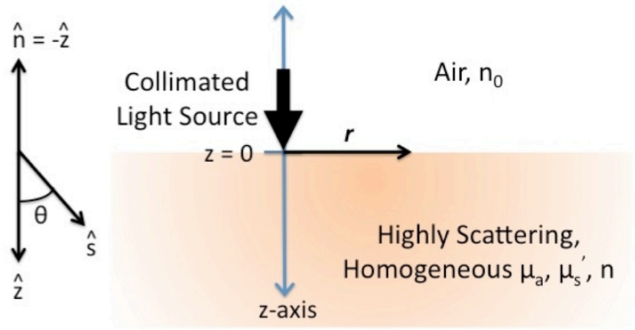


Figure 3, Diagram of a semi-infinite geometry. The air/homogeneous turbid medium interface spans the $z=0$ plane. The positive $\hat{z}$-direction extends into the turbid medium. $\theta$ is defined as the azimuthal angle between the $\hat{z}$-direction and the direction the radiance travels along ($\hat{s}$).

tissue/air boundary, where $\ell_{tr} \equiv 1/\mu_s'$ is the photon transport mean free path. The validity of this assumption for most problems has been demonstrated by [86, 87]. Thus, within this approximation the source term takes the following form:

$$S(\boldsymbol{r}, t) = (S_{DC} + S_{AC} e^{-i\omega t})\delta(x = 0, y = 0, z = \ell_{tr}). \quad [24]$$

The exact solution to the photon diffusion given the partial-current boundary condition (Equation 23) and an embedded isotropic source approximation (Equation 24) is non-trivial and involves an improper integral. However, a good approximation of the partial-current boundary condition is the so-called extrapolated-zero boundary condition, which makes an estimation for where the fluence falls to zero using the partial-current boundary condition (Equation 23). Let $z = z_b$ be the value of z for which the fluence rate falls to zero; notice this position should be in the "air" medium. To determine $z_b$, a Taylor series expansion near $z = 0$ of the fluence rate, $\phi(z)$, is used:

$$\phi(z = z_b) = \phi(z = 0) + \frac{\partial \phi}{\partial z}\Big|_{z=0} (z_b - 0) \cong 0. \quad [25]$$

Using $\frac{3\mu_s'}{2}\frac{\partial \phi}{\partial z}\Big|_{z=0} = \phi(z = 0)$ from in Equation 23 at $z = 0$, we find that the fluence falls to zero at $z = z_b = \frac{-2}{3\mu_s'}$. With this new condition for where $\phi$ is zero, we can apply the method of images.

As seen in Figure 4, when the fluence rate solution is a sum of the infinite medium solution for a source at $z = \ell_{tr}$ and an image source with the same magnitude but opposite sign at $z = -(2z_b + \ell_{tr})$, this boundary "zero" condition at $z_b$ is satisfied. Thus, the solution to the diffusion equation for a perfectly transmitting boundary given the extrapolated-zero boundary condition is (to a good approximation):

$$\phi(\boldsymbol{r},t)=\frac{\nu S_{DC}}{4\pi D}\left[\frac{\mathrm{e}^{-\mathrm{k_0 r_1}}}{r_1}-\frac{\mathrm{e}^{-\mathrm{k_0 r_2}}}{r_2}\right]+\frac{\nu S_{AC}}{4\pi D}\left[\frac{\mathrm{e}^{\mathrm{ikr_1}}}{r_1}-\frac{\mathrm{e}^{\mathrm{ikr_2}}}{r_2}\right]\mathrm{e}^{\mathrm{i\omega t}}, \quad [26]$$

where $\mathrm{r}_1=\sqrt{r^2+(z-\ell_{tr})^2}$ is the distance to the source from the detector, $\mathrm{r}_2=\sqrt{r^2+(z+\ell_{tr}+2z_b)^2}$ is the distance to the image source from the detector, $k_0=\sqrt{3\mu_a\mu_s'}$, and $k^2=(\mu_a\nu-i\omega)/D$. Here that the fluence rate is written as the sum of an AC and DC component.

If the index of refraction of the turbid medium is significantly different from that of air ($n_0=1.0$), as is the case with tissue ($n=1.4$), Fresnel reflection of diffuse light traveling out towards the interface from the turbid medium near the boundary provides a mechanism for the radiance to return to the medium. We can write the inward irradiance ($E_{in}$, or the inward radiance within the turbid medium) at the boundary, in this case, as the integral of the radiance reflected back into the turbid medium [67]:

$$\mathrm{E}_{in}=\int_0^{2\pi}\int_{\pi/2}^{\pi}R_{Fresnel}(\hat{s})L(\hat{s})\,\hat{s}\cdot\hat{n}\;\sin\theta\,d\theta d\phi. \quad [27]$$

Here $R_{fresnel}(\hat{s})$ is the Fresnel reflection coefficient for unpolarized light that is

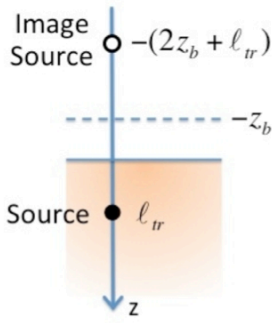


Figure 4, Diagram of the extrapolated-zero boundary condition for a semi-infinite geometry. An approximate solution involves an extrapolated boundary located at $z=z_b$ (shown by dotted line) wherein the fluence rate falls to 0. The solution for $\Phi(r,t)$ is arrived at via the method of images where the image source is positioned at $z=-(2z_b+\ell_{tr})$.

dependent on the angle of incidence, $\theta$, the refracted angle, $\theta'$ (where $n \sin\theta = n_0 \sin\theta'$), and the critical angle, $\theta_c$ (where $n \sin\theta_c = n_0$):

$$R_{Fresnel}(\theta) = \begin{cases} \frac{1}{2}\left(\frac{n\cos\theta' - n_0\cos\theta}{n\cos\theta' + n_0\cos\theta}\right)^2 + \frac{1}{2}\left(\frac{n\cos\theta - n_0\cos\theta'}{n\cos\theta + n_0\cos\theta'}\right)^2 ; 0 \le \theta \le \theta_c \\ 1 \qquad\qquad ; \theta_c \le \theta \le \pi/2 \end{cases} \quad [28]$$

After some manipulation we find [67]:

$$\mathrm{E}_{in} = \int_0^{2\pi}\int_{\pi/2}^{\pi} R_{Fresnel}(\hat{s}) L(\hat{s})\, \hat{s}\cdot\hat{n}\ \ \sin\theta\, d\theta d\phi = R_\phi \frac{\phi}{4} - R_j \frac{j_z}{2}, \quad [29]$$

Here $j_z$ is the magnitude of the photon flux in the $\hat{z}$-direction, and $R_\phi$ and $R_j$ are defined as:

$$R_\phi = \int_0^{\pi/2} 2\sin\theta\cos\theta\, R_{Fresnel}(\theta) d\theta, \quad [30]$$

$$R_j = \int_0^{\pi/2} 3\sin\theta\cos^2\theta\, R_{Fresnel}(\theta) d\theta. \quad [31]$$

Values for $R_\phi$ and $R_j$ for various index of refraction mismatches may be found in Haskell's 1994 paper [67].

As discussed in the perfectly transmitting boundary case, the inward radiance at the boundary can also be expressed as (see Equation 22):

$$\mathrm{E}_{in}(z=0,t) = \frac{\phi(z=0,t)}{4} + \frac{J_z(z=0,t)}{2}. \quad [32]$$

Thus, by setting the two equations for the irradiance at the boundary (Equations 32 and 27) equal to each other, we arrive at a "modified" partial-current boundary condition for the more realistic case of a reflecting boundary:

$$\phi = -2\frac{1+R_j}{1-R_\phi} j_z. \quad [33]$$

This boundary condition is often rewritten as:

$$\phi = \left(\frac{2}{3}\frac{1+R_{eff}}{1-R_{eff}}\ell_{tr}\right)\frac{\partial\phi}{\partial z}. \quad [34]$$

Here $R_{eff}$ represents the fraction of outward radiance (i.e., emittance, $E_{emitt}$) that is reflected back into the medium, i.e., $E_{irrad} = R_{eff}E_{emitt}$, and it is defined as $R_{eff} = (R_\phi + R_j)/(2 - R_\phi + R_j)$. For a tissue/air boundary, $R_{eff} = 0.493$ [67].

As discussed for the perfectly transmitting boundary, the exact solution to the photon diffusion given the partial-current boundary condition and embedded isotropic source approximation is quite complex and involves an improper integral. However, a good approximation of the partial-current boundary condition is the extrapolated-zero boundary condition, where the fluence falls to zero at $z = z_b$. To determine the location of $z_b$, a Taylor series expansion of the fluence rate $\phi(z)$ at $z = 0$ is used:

$$\phi(z = z_b) = \phi(z = 0) + \left.\frac{\partial\phi}{\partial z}\right|_{z=0}(z_b - 0) \cong 0. \quad [35]$$

Plugging in Equation 23 for $\phi(z = 0)$, we find that the fluence falls to zero at $z_b = \frac{2}{3}\frac{1+R_{eff}}{1-R_{eff}}\ell_{tr}$. Again, the principle of image sources, as in simple electrostatics, provides a means to extract solutions in which the fluence rate will fall to zero outside the medium at $z = z_b$. To satisfy this extrapolated zero boundary condition, an image source of equal magnitude but opposite sign is placed at a distance $-(2z_b + \ell_{tr})$ from the origin. Then the homogeneous semi-infinite medium solution within the extrapolated zero

boundary approximation is the sum of the infinite medium point source and its image source:

$$\phi(\boldsymbol{r},t)=\frac{\nu S_0}{4\pi D}\left[\frac{\mathrm{e}^{-\mathrm{k_0 r_1}}}{r_1}-\frac{\mathrm{e}^{-\mathrm{k_0 r_2}}}{r_2}\right]+\frac{\nu S_{AC}}{4\pi D}\left[\frac{\mathrm{e}^{\mathrm{ikr_1}}}{r_1}-\frac{\mathrm{e}^{\mathrm{ikr_2}}}{r_2}\right]\mathrm{e}^{\mathrm{i\omega t}}, \qquad [36]$$

where $\mathrm{r}_1=\sqrt{r^2+(z-\ell_{tr})^2}$ is the distance to the source from the detector located at $r$, $\mathrm{r}_2=\sqrt{r^2+(z+\ell_{tr}+2z_b)^2}$ is the distance to the image source from the detector, $z_b=2(1+R_{eff})/3\mu_s'(1-R_{eff})$, $k_0=\sqrt{3\mu_a\mu_s'}$, and $k^2=(\mu_a\nu-i\omega)/D$.

Finally, I would like to point out that the quantity we measure in experimental practice is the integral of the radiance $L(\boldsymbol{r},\hat{s},t)$ over the numerical aperature of the detection fiber:

$$\text{Detected signal}=\iint dxdy\iint T_{Fresnel}(\hat{s})L(x,y,z=0,\hat{s},t)(\hat{s}\cdot\hat{n})d\Omega, \qquad [37]$$

$$=\iint dxdy\iint T_{Fresnel}(\hat{s})\left(\frac{1}{4\pi}\Phi(\boldsymbol{r},t)+\frac{3}{4\pi}\boldsymbol{J}(\boldsymbol{r},t)\cdot\hat{s}\right)(\hat{s}\cdot\hat{n})d\Omega. \qquad [38]$$

Thus, the detected signal has contributions from both the photon fluence rate and photon flux. However, since these two quantities, i.e., fluence rate and flux, are proportional at the boundary (required by the boundary condition), the detected signal is also proportional to *either* the fluence rate or the flux [67] with different proportionality constants. Thus, determination of $\phi(\boldsymbol{r},t)$ gives detected signals.

### 2.1.4 Semi-Infinite Geometry in Experimental Practice

Assuming the source and detector are placed in the same plane (see Figure 5), and the source-detector separation, $|\boldsymbol{r}|$, is large compared to the transport mean free path (i.e.,

$|\boldsymbol{r}| \gg \ell_{tr}$), the distances to the source and image source can be approximated by $r\left(1 + {}^{1}/_{2}\,(\ell_{tr}/r)^2\right)$ and $r\left(1 + {}^{1}/_{2}\,(\ell_{tr} + 2z_b)^2\right)$, respectively. Equation 36 can then be simplified to the following after some algebraic rearrangement and after expanding $e^{ik{\ell_{tr}}^2/2r} \cong 1 + ik{\ell_{tr}}^2/2r$ and $e^{ik(\ell_{tr}+2z_b)^2/2r} \cong 1 + ik(\ell_{tr} + 2z_b)^2/2r$:

$$\Phi(\boldsymbol{r}, t) = \frac{\nu S_0}{4\pi D}\frac{\mathrm{e}^{-\mathrm{k_0 r}}}{r^2}\left[2k_0(\ell_{tr}z_b + z_b^2)\right] + \frac{\nu S_0}{4\pi D}\frac{\mathrm{e}^{\mathrm{ikr}}}{r^2}\left[-2ik(\ell_{tr}z_b + z_b^2)\right]\mathrm{e}^{\mathrm{i\omega t}}. \quad [39]$$

The AC component of $\Phi(\boldsymbol{r})$ can be broken up into a real and imaginary component [79]:

$$\Phi(\boldsymbol{r}) = \frac{\nu S_0}{4\pi D}\frac{e^{ikr}}{r^2}\left(-2ik\left(\ell_{tr}z_b + z_b^2\right)\right) = A(r)e^{i\theta(r)}\ , \quad [40]$$

where $A(\boldsymbol{r})$ and $\theta(\boldsymbol{r})$ are the amplitude and phase of the detected light [88, 89]. From this equation, we note the following linear relations:

$$\ln(A(\boldsymbol{r})r^2) = -k_i r + A_0\ , \quad [41]$$

$$\theta(\boldsymbol{r}) = k_r r + \theta_0. \quad [42]$$

Thus, we can measure the amplitude attenuation and phase shift at multiple source-detector separations on the tissue surface, to extract the slopes, $k_i$ and $k_r$, respectively, of $\ln\,(A(\boldsymbol{r})r^2)$ versus $r$ and $\theta$ versus $r$. Rearranging the formulas for $k_i$ and $k_r$ to solve for $\mu_a$ and $\mu_s'$ of the sample, we find:

$$\mu_a = \frac{\omega}{2\nu}\left(\frac{k_i}{k_r} - \frac{k_r}{k_i}\right),\ \mu_s' = \frac{2\nu}{3\omega}k_r k_i\ . \quad [43]$$

Figure 5 demonstrates sample data taken on a solid silicon phantom with a frequency domain instrument operating at 110 MHz in a semi-infinite geometry. The

source fiber was kept in place and the detector fiber was translated across the phantom in fixed increments. Using the semi-infinite diffusion model, the optical properties of the phantom can be readily extracted (see Appendix 2.5 for more detailed experimental methods). The calculated optical properties typically match with the expected properties of the phantom to within 10%.

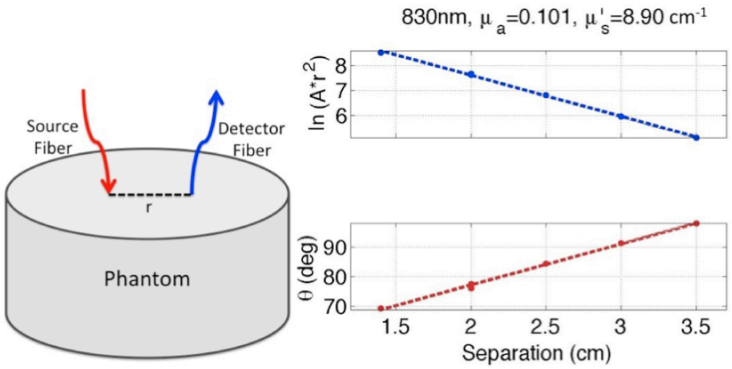


Figure 5, Amplitude and phase data (solid circles) taken on a solid phantom (setup shown on left) emulating a semi-infinite homogeneous medium at 830nm and 5 source-detector separations ranging from 1.4 to 3.5 cm. The dotted lines indicate the best linear fit lines, and the extracted optical properties from these fits are listed in the title.

### 2.1.5 Differential Pathlength Method

When multiple source-detector pairs are not an option for spectroscopy measurements, for example as a result of size limitations on the patient's head or other instrumentation limitations (i.e., limited sources or detectors), then an alternative approach to data analysis is needed to derive information about chromophore concentrations and changes thereof.

Although the Beer-Lambert law[2] cannot be accurately applied to biological tissue

[2]The Beer-Lambert law provides a well-known means to measure the concentration of absorbers in optically thin, homogenous samples that do not scatter light: $\ln\left(\frac{I}{I_0}\right) = -\mu_a \ell$. Here $I$ and $I_0$ are the intensities of the transmitted and incident light, respectively; $\mu_a$ is the absorption coefficient of the sample, equal to the concentration of the absorbers

(due to the highly scattering nature of tissue), it turns out that a modified version of the Beer-Lambert law, dubbed the modified Beer-Lambert law (MBL) can be applied to turbid medium such as tissue [88, 90]. This modified approach accounts for the distribution of light pathlengths in the turbid sample caused by multiple light scattering, and it provides an approximate means to quantify *changes* in the concentration of the chromophores within a highly scattering medium.

The MBL is traditionally written as[3] (see detailed derivation in Appendix 2.6)

$$\ln\left(\frac{I_{DC}(\boldsymbol{r},\lambda,t)}{I_{DC}(\boldsymbol{r},\lambda,0)}\right) \equiv \Delta\mathrm{OD}(\mathbf{r},\lambda,\mathrm{t}) \cong -\Delta\mu_a(\lambda,t)\, L_{eff}(\lambda). \qquad [44]$$

Here $I_{DC}(\boldsymbol{r},\lambda,t)$ is the DC intensity of the detected light at position $\boldsymbol{r}$ and time $t$, respectively; $\Delta\mu_a(\lambda)$ is change in the absorption coefficient as a function of time compared to its value at $t=0$; and $L_{eff}(\lambda)$ is called *effective* pathlength, a term that takes into account the increased optical pathlength photons travel on average caused by multiple light scattering. $L_{eff}(\lambda)$ is the mean optical pathlength a photon travels from source to detector; it depends on the source detector separation, the sample geometry, and the wavelength of light. There are many ways to determine $L_{eff}$ for a given sample geometry. Experimental data [91], Monte Carlo simulations [91], and diffusion theory relationships [88, 90] all provide a means to determine $L_{eff}$. For neonatal populations (the focus of this dissertation), population averaged values of $L_{eff}(\lambda)$ have been reported by several groups [75, 92-94].

---

within the sample times the extinction coefficient of the absorber; and $\ell$ is the length the light travels.

[3]This equation is also written as $\ln\left(\frac{I_{DC}(\boldsymbol{r},\lambda,t)}{I_{DC}(\boldsymbol{r},\lambda,0)}\right) \equiv \Delta\mathrm{OD}(\mathbf{r},\lambda,\mathrm{t}) \cong -\Delta\mu_a(\lambda,t)\, DPF(\lambda)\, r$, where $L_{eff}(\lambda) \equiv DPF(\lambda)\, r$ and $DPF(\lambda)$ is known as the differential pathlength factor.

The advantage in utilizing the modified Beer-Lambert law is that only a single source-detector separation is needed in ordered to quantify *changes* in the optical absorption coefficient over time. However, several conditions must be met in order to employ the MBL for data analysis, i.e., changes in scattering are negligible, absorption changes are global, the tissue is homogenous, and absorption changes are small relative to their baseline values ($\Delta\mu_a(\lambda,t)/\mu_a(\lambda,t=0) \ll 1$). Assuming these conditions are met, changes in the absorption coefficient at multiple wavelengths are calculated using:

$$\Delta\mu_a(\lambda,t) = \frac{1}{L_{eff}(\lambda)} \ln\left(\frac{I_{DC}(\boldsymbol{r},\lambda,0)}{I_{DC}(\boldsymbol{r},\lambda,t)}\right). \quad [45]$$

## 2.2 Frequency Domain Instrumentation

In frequency domain diffuse optical spectroscopy, a radio-frequency (RF) oscillator is typically employed to modulate the amplitude of a laser source sinusoidally in the ~100 MHz range. This modulated light, delivered to a sample via fiber optic cable, experiences both an amplitude attenuation and phase-shift in the medium. The detection optics and electronics aim to quantify the amplitude attenuation ($A$) and phase shift ($\theta$) in order to reconstruct the optical properties of the sample.

Amplitude attenuation is a relatively easy parameter to measure. Thus, the setups discussed herein are unique in their ability to detect phase shift. Because the phase shift is highly dependent on the modulation frequency (see Figure 6), care must be taken when choosing an RF driving frequency. Higher modulation frequencies yield a greater phase shift with varying source-detector separation, but also a smaller penetration depth. For typical brain measurements of absolute optical properties,

separations of $2-4$ cm or greater are used, leading to an average phase shift of more than 20° at 70 MHz. However, for animal studies or for shallow penetration depth studies in which smaller separations are used, higher frequency devices are better in order to maximize the phase shift over the separation range.

There are two main phase detection schemes that will be discussed in this section. Homodyne detection detects amplitude and phase shift at the same RF carrier frequency, which drives the laser, whereas heterodyne detection converts the detected RF signal to a lower frequency before determination of phase shift. Homodyne systems have the advantage of simplicity and lower costs, while heterodyne systems, although more complex, have greater phase shift accuracy. These two techniques are discussed in depth in Chapter 4.

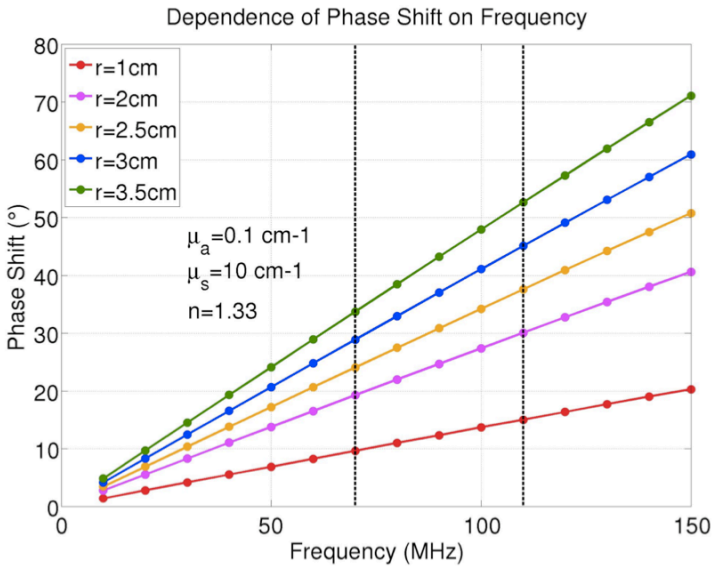


Figure 6, Relationship between phase shift and modulation frequency for absorption and scattering properties similar to that of brain tissue. Dotted vertical lines indicate the two frequencies employed in the instruments discussed in this dissertation, namely 70 and 110 MHz.

## 2.3 Measured Parameters

### 2.3.1 Chromophore Concentration

As mentioned in Section 1.2.6, the absorption coefficient in brain tissue is mainly dominated by contributions from water, oxy- and deoxy-hemoglobin. After quantifying concentrations of oxy- and deoxy-hemoglobin, $C_{Hb}$ and $C_{HbO_2}$, respectively, total hemoglobin concentration ($\mu M$] ($THC = C_{Hb} + C_{HbO_2}$) and tissue oxygen saturation [%] ($StO_2 = C_{HbO_2}/THC \times 100\%$) are easily obtained. $THC$ can, in turn, be related to cerebral blood volume [mL/100 g brain tissue] via the following formula,

$$\mathrm{CBV} = \frac{THC \times MW_{Hb}}{[HGB] \times R \times D_{bt} \times 10^5} = \frac{0.89 \times THC}{[HGB]}, \quad [46]$$

where $MW_{Hb} = 6.45 \times 10^4$ [g/moles] is the molecular weight of deoxy-hemoglobin, $[HGB]$ [g/dL] is the large vessel deoxy-hemoglobin concentration (measured by arterial blood gas), $R$ is the large vessel-to-cerebral hematocrit ratio (0.69), and $D_{bt}$ is the density of brain tissue (1.05 g/mL in neonates) [95].

### 2.3.2 Scattering

Light scattering is caused by variations in refractive index. The major scatterers in tissue are the organelles, cell nuclei, mitochondria, and red blood cells. Assuming these scatterers are homogeneous, dielectric spheres with index of refraction $n_s$ and that they are surrounded by a medium with index of refraction $n_m$, Mie theory can be used to approximate the wavelength dependence of the reduced scattering coefficient (provided that the light incident on each scatterer is a plane wave) [96, 97]. Although these assumptions are not exact for biological tissue given the wide distribution of scatterer

sizes (ranging from fractions of a micron to tens of microns in diameter), experimental measurements demonstrate that the scattering coefficient in tissue is reasonably well approximated by the following power-law wavelength dependence:

$$\mu_s'(\lambda) = \mathrm{A}\lambda^{-b}. \quad [47]$$

Here $A$ is called the scattering prefactor, which is proportional to the density of the scattering centers and their size ($A \equiv N\sigma_s$, where N is the number density of scatterers and $\sigma_s$ is the cross-sectional area of the scatterers). The scattering power, $b$, depends on the scatterers' size [97, 98]. Therefore, measurements of $\mu_s'$ at multiple optical wavelengths enable us to extract the scattering parameters $A$ and $b$ and thus gain insight into tissue morphology.

## 2.4 DOS Summary

This chapter summarizes the theory behind diffuse optical spectroscopy for use in neonatal cerebral monitoring. In a highly scattering medium such as brain tissue, photon migration is modeled as a diffusive process. The theoretical predictions provide a means to extract the absorption and reduced scattering coefficients of the tissue.

## 2.5 APPENDIX: Calibration for Absolute Optical Properties

In practice, translation of the source and/or detector fibers to yield multiple source-detector separations is not practical. The experimental probes usually consist of multiple source and/or detector fibers that are positioned at varying separations. This configuration introduces some practical problems that must be dealt with if one desires high quality data. Specifically, variations in fiber transmission and detector efficiency

(and also laser intensity for multi-spectral measurements) must be calibrated in order to generate accurate fluence rates at multiple source-detector separations. Thus, we define $s_i$ as the coupling coefficient for the $i^{th}$ source, and $d_j$ as the coupling coefficient for the $j^{th}$ detector. Thus, the measured fluence rate at detector $j$ arising from source $i$, $\phi_{ij}$, is defined as

$$\phi_{ij}^{meas}(\lambda) = s_i(\lambda) d_j(\lambda) \phi^{Theor}(\boldsymbol{r_{ij}}, \lambda). \quad [48]$$

Here $\phi^{Theor}(r_{ij}, \lambda)$ is the theoretical fluence rate at $r_{ij}$, the distance between the $i^{th}$ source and $j^{th}$ detector. Note that the coupling coefficients are complex numbers that account for both an amplitude and phase correction to the measured fluence rate, i.e., $s_i(\lambda) = s_i^A e^{is_i^p}$ and $d_j(\lambda) = d_j^A e^{id_j^p}$. We further expand Equation 48 into amplitude and phase:

$$A_{ij}^{meas}(\lambda) = s_i^A(\lambda) d_j^A(\lambda) A^{Theor}(\boldsymbol{r_{ij}}, \lambda); \;\; \theta_{ij}^{meas}(\lambda) = s_i^p(\lambda) + d_j^p(\lambda) + \theta^{Theor}(\boldsymbol{r_{ij}}, \lambda) \quad [49]$$

Here we have assumed the measured and theoretical fluence rate are complex numbers with amplitude and phase, i.e., $\phi_{ij}^{meas}(\lambda) = A_{ij}^{meas}(\lambda) e^{\theta_{ij}^{meas}(\lambda)}$ and $\phi^{Theor}(\boldsymbol{r_{ij}}, \lambda) = A^{Theor}(\boldsymbol{r_{ij}}, \lambda) e^{\theta^{Theor}(\boldsymbol{r_{ij}}, \lambda)}$.

To determine these source and detector coupling coefficients ($s_i$ and $d_j$, respectively), a phantom with known optical properties is employed. These coefficients may then be applied to all subsequent measurements on phantoms/tissue in order to extract the unknown optical properties, $\mu_a$ and $\mu_s'$. This technique is susceptible to errors from the differences in the probe/phantom interface as compared to the tissue/probe

interface. However, it has been shown to produce repeatable and accurate results [99, 100].

To demonstrate the calibration procedure, measurements were made on a phantom with known optical properties ( $\mu_a(688nm) = 0.137\ cm^{-1}$ , $\mu_a(787nm) = 0.131\ cm^{-1}$ , $\mu_a(830nm) = 0.133\ cm^{-1}$ , and $\mu_s'(688nm) = 5.2$ , $\mu_s'(787nm) = 4.6\ cm^{-1}$ , $\mu_s'(830nm) = 4.3\ cm^{-1}$) using an optical probe with one detector and four sources, where three light wavelengths are sent to each of the four sources (see Figure 7). The semi-infinite solution to the diffusion approximation with these optical properties predicts that $\ln(A(\boldsymbol{r},\lambda)r^2)$ and $\theta(\boldsymbol{r},\lambda)$ will be linear functions with respect to r (see Section 2.1.3), and that the slopes of $\ln(A(\boldsymbol{r},\lambda)r^2)$ and $\theta(\boldsymbol{r},\lambda)$ versus $r$, i.e., $k_i$ and $k_r$, are related to $\mu_a(\lambda)$ and $\mu_s'(\lambda)$. The theoretical prediction of amplitude and phase are indicated by dotted lines in Figure 7. The variations in fiber transmission and detector efficiency (and also laser intensity), and hence the need for calibration, are evident from this figure, as the raw data (shown in solid circles) does not fall on the predicted lines.

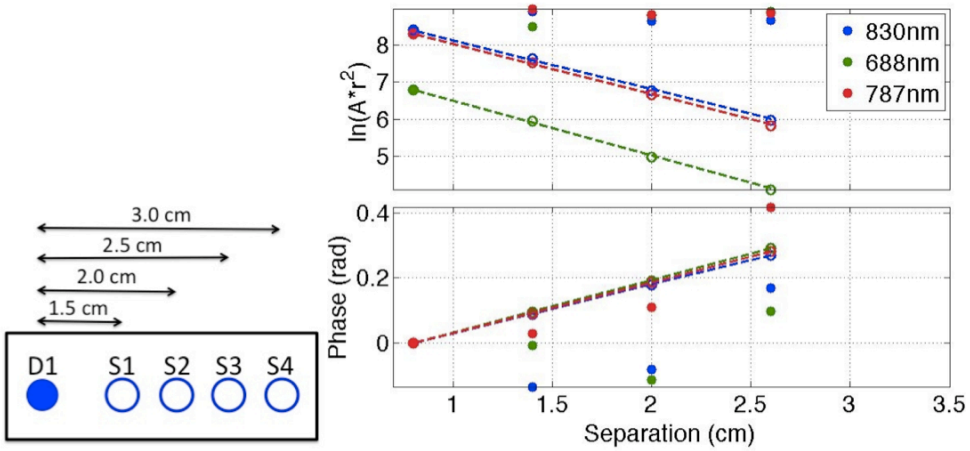


Figure 7, Amplitude and phase data taken on a solid phantom with known optical properties at multiple wavelengths and multiple source-detector separations. Solid points show raw data, while open circles show data calibrated to match the expected values (dotted lines). These calibration factors are then applied to all subsequent data.

Thus, we can compute the source and detector coupling coefficients ($s_i$ and $d_j$, respectively) from the measured amplitude and phase ($A_{ij}^{meas}(\lambda)$ and $\theta_{ij}^{meas}(\lambda)$) and the predicted amplitude and phase for the given optical properties of the phantom ($A^{Theor}(r_{ij},\lambda)$ and $\theta^{Theor}(r_{ij},\lambda)$) using Equations 48 and 49:

$$s_1^A(\lambda)d_1^A(\lambda) = A_{11}^{Meas}(\lambda)/A^{Theor}(r_{11},\lambda),\ \ s_1^p(\lambda) + d_1^p(\lambda) = \theta_{11}^{Meas}(\lambda) - \theta^{Theor}(r_{11},\lambda) \text{[50]}$$

$$s_2^A(\lambda)d_1^A(\lambda) = A_{21}^{Meas}(\lambda)/A^{Theor}(r_{21},\lambda),\ \ s_2^p(\lambda) + d_1^p(\lambda) = \theta_{21}^{Meas}(\lambda) - \theta^{Theor}(r_{21},\lambda) \text{[51]}$$

$$s_3^A(\lambda)d_1^A(\lambda) = A_{31}^{Meas}(\lambda)/A^{Theor}(r_{31},\lambda),\ \ s_3^p(\lambda) + d_1^p(\lambda) = \theta_{31}^{Meas}(\lambda) - \theta^{Theor}(r_{31},\lambda) \text{[52]}$$

$$s_4^A(\lambda)d_1^A(\lambda) = A_{41}^{Meas}(\lambda)/A^{Theor}(r_{41},\lambda),\ \ s_4^p(\lambda) + d_1^p(\lambda) = \theta_{41}^{Meas}(\lambda) - \theta^{Theor}(r_{41},\lambda). \text{[53]}$$

Once these coupling coefficients are determined, measurements can be made on other samples (with unknown optical properties), and raw amplitude and phase data from these samples can be corrected for source and detector coupling coefficients using the following formulas:

$$A_{11}(\lambda) = A_{11}^{Meas}(\lambda)/s_1^A(\lambda)d_1^A(\lambda),\ \ \theta_{11}(\lambda) = \theta_{11}^{Meas}(\lambda) - (s_1^p(\lambda) + d_1^p(\lambda)) \quad \text{[54]}$$

$$A_{21}(\lambda) = A_{21}^{Meas}(\lambda)/s_2^A(\lambda)d_1^A(\lambda),\ \ \theta_{21}(\lambda) = \theta_{21}^{Meas}(\lambda) - (s_2^p(\lambda) + d_1^p(\lambda)) \quad \text{[55]}$$

$$A_{31}(\lambda) = A_{31}^{Meas}(\lambda)/s_3^A(\lambda)d_1^A(\lambda),\ \ \theta_{31}(\lambda) = \theta_{31}^{Meas}(\lambda) - (s_3^p(\lambda) + d_1^p(\lambda)) \quad \text{[56]}$$

$$A_{41}(\lambda) = A_{41}^{Meas}(\lambda)/s_4^A(\lambda)d_1^A(\lambda),\ \ \theta_{41}(\lambda) = \theta_{41}^{Meas}(\lambda) - (s_4^p(\lambda) + d_1^p(\lambda)). \quad \text{[57]}$$

## 2.6 APPENDIX: Modified Beer-Lambert Law Derivation

The modified Beer-Lambert law (MBL) starts with the realization that the optical density (OD), defined as $\log(R)$, where $R$ is the reflectance ($R \equiv I/I_0$), is a function of $\mu_a$, $\mu_s'$, and $\boldsymbol{r}$. We assume that changes in the optical density over time are solely due to changes in $\mu_a$ and $\mu_s'$:

$$\Delta \mathrm{OD}(\mu_a, \mu_s', \mathbf{r}, \mathrm{t}) = \mathrm{OD}(\mu_a(\lambda, \mathrm{t}=0) + \Delta\mu_a(\lambda, \mathrm{t}), \mu_s'(\lambda, \mathrm{t}=0) + \Delta\mu_s'(\lambda, t), \mathbf{r})$$

$$-\mathrm{OD}(\mu_a(\lambda, \mathrm{t}=0), \mu_s'(\lambda, \mathrm{t}=0), \mathbf{r}). \quad [58]$$

Using a Taylor series expansion, i.e., $f(x+\Delta x) = f(x) + f'(x)\Delta x + f''(x)/2!\ \Delta x + \cdots$, $\mathrm{OD}(\mu_a(\lambda, \mathrm{t}=0) + \Delta\mu_a(\lambda, \mathrm{t}), \mu_s'(\lambda, \mathrm{t}=0) + \Delta\mu_s'(\lambda, t), \mathrm{r})$ is expressed as:

$$\mathrm{OD}(\mu_a(\lambda, \mathrm{t}=0) + \Delta\mu_a(\lambda, \mathrm{t}), \mu_s'(\lambda, \mathrm{t}=0) + \Delta\mu_s'(\lambda, t), \mathbf{r}) = \mathrm{OD}(\mu_a(\lambda, \mathrm{t}=0), \mu_s'(\lambda, \mathrm{t}=0), \mathbf{r}) + \frac{\partial \mathrm{OD}(\mu_a(\lambda, \mathrm{t}=0), \mu_s'(\lambda, \mathrm{t}=0), \mathbf{r})}{\partial \mu_a} \Delta\mu_a + \frac{\partial \mathrm{OD}(\mu_a(\lambda, \mathrm{t}=0), \mu_s'(\lambda, \mathrm{t}=0), \mathbf{r})}{\partial \mu_s'} \Delta\mu_s' + \frac{1}{2!} \frac{\partial^2 \mathrm{OD}(\mu_a(\lambda, \mathrm{t}=0), \mu_s'(\lambda, \mathrm{t}=0), \mathbf{r})}{\partial {\mu_a}^2} (\Delta\mu_a)^2 + \frac{1}{2!} \frac{\partial^2 \mathrm{OD}(\mu_a(\lambda, \mathrm{t}=0), \mu_s'(\lambda, \mathrm{t}=0), \mathbf{r})}{\partial {\mu_s'}^2} (\Delta\mu_s')^2 + \frac{1}{2!} \frac{\partial^2 \mathrm{OD}(\mu_a(\lambda, \mathrm{t}=0), \mu_s'(\lambda, \mathrm{t}=0), \mathbf{r})}{\partial \mu_a \partial \mu_s'} \Delta\mu_a \Delta\mu_s' + \cdots. \quad [59]$$

The modified Beer-Lambert law (MBL) approximates $\Delta \mathrm{OD}(\mu_a, \mu_s', \mathbf{r}, \mathrm{t})$ with only the first order terms of this expansion, i.e.

$$\Delta \mathrm{OD}(\mu_a, \mu_s', \mathbf{r}, \mathrm{t}) \cong \frac{\partial \mathrm{OD}(\mu_a(\lambda, \mathrm{t}=0), \mu_s'(\lambda, \mathrm{t}=0), \mathbf{r})}{\partial \mu_a} \Delta\mu_a + \frac{\partial \mathrm{OD}(\mu_a(\lambda, \mathrm{t}=0), \mu_s'(\lambda, \mathrm{t}=0), \mathbf{r})}{\partial \mu_s'} \Delta\mu_s' \quad [60]$$

In most clinical experiments, it is assumed that the absorption changes are global and homogenous so that $\Delta\mu_a(\lambda) = \sum_i \epsilon_i(\lambda)\, \Delta C_i$.

As discussed in Section 2.1.5, the MBL is formulated in terms of an *effective*

pathlength ($L_{eff}$) that photons travel on average before arriving at the detector as $\Delta \mathrm{OD}(\mu_a, \mu_s', \mathbf{r}, \mathrm{t}) = -L_{eff} \times \Delta\mu_a$. $L_{eff}$ depends on the source detector separation, $\boldsymbol{r}$, sample geometry, and the wavelength of light. There are many ways to determine $L_{eff}$ for a given sample geometry. Experimental data [75, 90], Monte Carlo simulations [101], and diffusion theory relationships [90] all provide a means to determine $L_{eff}$.

To solve for $L_{eff}$ analytically, we note that Equation 60 relates $L_{eff}$ to the partial derivative of the optical density, i.e., $L_{eff} = -\partial OD(\mu_a(\lambda, t = 0, \boldsymbol{r})/\partial\mu_a$. This partial derivative can also be written in terms of a Green's function, $G(r, \omega)$, for a given geometry [90]:

$$L_{eff} = \frac{\partial \mathrm{OD}}{\partial \mu_a} = \frac{1}{R}\frac{\partial R}{\partial \mu_a} = \frac{1}{|G(r,\omega)|}\frac{\partial |G(r,\omega)|}{\partial \mu_a},$$

$$L_{eff} = \frac{1}{|G(r,\omega)|}\frac{\partial |G(r,\omega)|}{\partial k}\frac{\partial k}{\partial \mu_a}. \qquad [61]$$

Here vertical lines indicate the magnitude of the Green's function, $k$ is the wave vector ($k = \sqrt{(\nu\mu_a - i\omega)/D}$), and $G(r, \omega)$ satisfies the equation,

$$(\nabla^2 - k^2)G(r, \omega) = -\delta(\boldsymbol{r}), \qquad [62]$$

for the geometry of interest [68].

For the case of CW light, i.e., $\omega = 0$, with a semi-infinite geometry given the extrapolated zero boundary condition, the Green's function solution is real, i.e., $|G(r, \omega = 0)| = G(r, \omega = 0)$, and it is written as:

$$\mathrm{G}(\boldsymbol{r},\omega=0)=\frac{1}{4\pi}\left[\frac{\mathrm{e}^{-\mathrm{k}_0\mathrm{r}_1}}{r_1}-\frac{\mathrm{e}^{-\mathrm{k}_0\mathrm{r}_2}}{r_2}\right], \quad [63]$$

Thus, after some algebraic manipulation, we can write the following expression for $L_{eff}$ in terms of the baseline optical properties $\mu_a$, and $\mu_s'$, and source detector separation:

$$L_{eff}=\frac{1}{|G(r,\omega)|}\frac{\partial|G(r,\omega)|}{\partial k}\frac{\partial k}{\partial \mu_a}=\frac{3\mu_s' r_1 r_2}{2k_0}\frac{\left(e^{-k_0 r_1}-e^{-k_0 r_2}\right)}{\left(r_2 e^{-k_0 r_1}-r_1 e^{-k_0 r_2}\right)}. \quad [64]$$

Fantini et al [88] have shown that in the limit that $r \gg \ell_{tr}$, $L_{eff}$ can be simplified to:

$$\mathrm{L}_{eff}\cong\frac{3\mu_s' r^2}{2(rk_0+1)}. \quad [65]$$

Thus, for CW light incident on brain tissue (here I am assuming typical brain optical properties of $\mu_a=0.1cm^{-1}$ and $\mu_s'=10cm^{-1}$) with an optode spacing of $r=2.5\,cm$, the effective optical pathlength is $\sim$17.6 cm.

When the incident light is modulated at frequency $\omega$, the Green's function solution for the semi-infinite geometry given the extrapolated boundary condition is:

$$\mathrm{G}(\boldsymbol{r},\omega)=\frac{1}{4\pi}\left[\frac{\mathrm{e}^{\mathrm{ikr}_1}}{r_1}-\frac{\mathrm{e}^{\mathrm{ikr}_2}}{r_2}\right], \quad [66]$$

In order to write this the magnitude of $\mathrm{G}(\boldsymbol{r},\omega)$, I break up $\mathrm{G}(\boldsymbol{r},\omega)$ into its real and imaginary components (using the definition of the complex wave vector: $k=k_r+ik_i$, see Section 2.1.2), i.e., $\mathrm{G}(\boldsymbol{r},\omega)=a+ib$:

$$\mathrm{G}(\boldsymbol{r},\omega)=\frac{1}{4\pi}\left[\frac{\cos(k_r r_1)}{r_1}\mathrm{e}^{-\mathrm{k}_i\mathrm{r}_1}-\frac{\cos(k_r r_2)}{r_2}\mathrm{e}^{-\mathrm{k}_i\mathrm{r}_2}\right]+\frac{i}{4\pi}\left[\frac{\sin(k_r r_1)}{r_1}\mathrm{e}^{-\mathrm{k}_i\mathrm{r}_1}-\frac{\sin(k_r r_2)}{r_2}\mathrm{e}^{-\mathrm{k}_i\mathrm{r}_2}\right], \quad [67]$$

The magnitude of $\mathrm{G}(\boldsymbol{r},\omega)$, i.e., $|\mathrm{G}(\boldsymbol{r},\omega)|=\sqrt{a^2+b^2}$ is written explicitly as:

$$|\mathrm{G}(\boldsymbol{r},\omega)| = \frac{1}{4\pi}\sqrt{\left[\frac{\cos(k_r r_1)}{r_1}\mathrm{e}^{-\mathrm{k}_i \mathrm{r}_1} - \frac{\cos(k_r r_2)}{r_2}\mathrm{e}^{-\mathrm{k}_i \mathrm{r}_2}\right]^2 + \left[\frac{\sin(k_r r_1)}{r_1}\mathrm{e}^{-\mathrm{k}_i \mathrm{r}_1} - \frac{\sin(k_r r_2)}{r_2}\mathrm{e}^{-\mathrm{k}_i \mathrm{r}_2}\right]^2} \quad ,$$

$$= \frac{1}{4\pi}\sqrt{\frac{\mathrm{e}^{-2\mathrm{k}_i \mathrm{r}_1}}{{r_1}^2} + \frac{\mathrm{e}^{-2\mathrm{k}_i \mathrm{r}_2}}{{r_2}^2} - 2\frac{\mathrm{e}^{-\mathrm{k}_i(\mathrm{r}_1+\mathrm{r}_2)}}{r_1 r_2}\cos(\mathrm{k}_r(\mathrm{r}_1-\mathrm{r}_2))}, \qquad [68]$$

Thus the expression for $L_{eff}$ in the frequency domain becomes:

$$L_{eff} = \frac{1}{2A}\frac{\partial A}{\partial \mu_a}, \qquad [69]$$

where $A$ is the term under the square root in $|\mathrm{G}(\boldsymbol{r},\omega)|$, i.e.,

$$A = \frac{\mathrm{e}^{-2\mathrm{k}_i \mathrm{r}_1}}{{r_1}^2} + \frac{\mathrm{e}^{-2\mathrm{k}_i \mathrm{r}_2}}{{r_2}^2} - 2\frac{\mathrm{e}^{-\mathrm{k}_i(\mathrm{r}_1+\mathrm{r}_2)}}{r_1 r_2}\cos(\mathrm{k}_r(\mathrm{r}_1-\mathrm{r}_2)). \qquad [70]$$

Although the expression for $L_{eff}$ in the frequency domain is quite messy, nonetheless it is still solvable.

# 3 Diffuse Correlation Spectroscopy

While the previous chapter focused on the use of diffusing photons to extract the absorption and scattering properties of biological tissue, this chapter discusses how to use diffusing photons to probe the dynamical properties of deep (> 1 cm below the tissue surface) tissue. To study tissue dynamics, we employ a technique dubbed in the biomedical optics community as diffuse correlation spectroscopy (DCS) [68, 102, 103]; the method has its origin in soft condensed matter research wherein it is known as diffusing wave spectroscopy (DWS) [104, 105].

In DCS, coherent near-infrared light is injected into a highly scattering medium, such as tissue, wherein it travels deeply and scatters multiple times before detection at some distance from the light source. The electric field at a single point on the tissue surface is built from a superposition of multiply-scattered light fields that have traveled along different paths from the light source. These fields will constructively or destructively interfere to form bright or dark (i.e., high or low intensity) spots, or speckles, on the tissue surface. If the tissue scatterers are motionless and the light source is perfectly coherent, then the intensity of light at the spot will not change over time. However, in *in-vivo* tissue experiments, although the light source is well-approximated as being perfectly coherent, some of the scattering particles (e.g., red blood cells) are moving. This motion changes the phases of the multiply-scattered light fields traveling from source to detector, which, in turn, causes the intensity of the speckle to change over time.

Thus, intensity fluctuations of the speckles at the tissue surface contain information about the motion of the scatterers within tissue [69]. Faster fluctuations (i.e.,

more rapid decay of the intensity temporal autocorrelation function) are indicative of faster motion of the scatterers. In the case of tissue, although many kinds of scatterers move, it is the motion of the red blood cells that contributes dominantly to the fluctuations in observed speckle intensity [68, 102, 103, 106]. Therefore, by characterizing the fluctuations of speckle intensity over time, we can gather information about blood flow in tissue.

In order to monitor speckle fluctuations in time, we measure the normalized intensity autocorrelation function of the multiply-scattered light, $g_2(\boldsymbol{r},\tau) \equiv \langle I(\boldsymbol{r},t)I(\boldsymbol{r},t+\tau)\rangle/\langle I(\boldsymbol{r},t)\rangle^2$. Here $I(\boldsymbol{r},t) = |E(\boldsymbol{r},t)|^2$ is the intensity at time $t$ and detector position $\boldsymbol{r}$, and $\langle\rangle$ denotes the ensemble average (approximated by a time average for the data presented herein). The more rapidly the intensity fluctuates in time, the faster the intensity will become uncorrelated, which is analogous to a faster decay in the temporal intensity autocorrelation function. The details of the DCS experimental setup and instrumentation are found in Chapter 4.

Figure 8 demonstrates experimental DCS data obtained from the head of a neonate with a congenital heart defect during a simple hypercapnia intervention. Source and detector fibers were positioned 2.5 cm apart on the patient's forehead. A normalized intensity autocorrelation curve, $g_2(\tau)$, obtained during a baseline period of room air inhalation is plotted versus lag time, $\tau$, in black. $CO_2$ is known to be a potent cerebrovascular vasodilator causing significant increases in cerebral blood flow (see Sections 5.1 and 6.4.2). Notice, when the patient inhaled the $CO_2$ gas mixture, the decay time of $g_2(\tau)$ decreased substantially, indicating an increase in cerebral blood flow. Figure 8 clearly demonstrates that blood flow has an effect on the decay rate of the

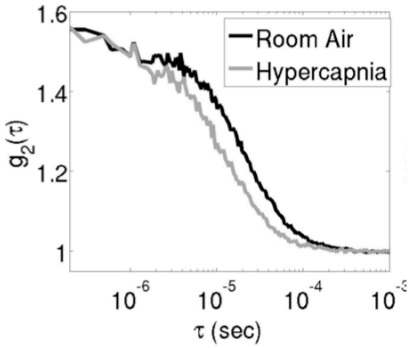


Figure 8, Sample intensity autocorrelation curves measured with DCS on a neonate with hypoplastic left heart syndrome. The black "Room Air" curve, taken on the patient's forehead during room air inhalation, decays slower than the grey "Hypercapnia" curve obtained while the patient inhaled a CO2 gas mixture. The increased decay rate of the correlation curve during hypercapnia indicates an increase in cerebral blood flow.

intensity autocorrelation function. However, to quantitatively model the effect of blood flow, we need to employ correlation transport theory for the temporal electric field autocorrelation function.

## 3.1 Correlation Diffusion Equation

Ackerson et al [107] first suggested that the un-normalized electric field temporal autocorrelation function, $G_1(\boldsymbol{r},\tau) \equiv \langle E(\boldsymbol{r},t)E^*(\boldsymbol{r},t+\tau)\rangle$, should obey a correlation transfer equation based on modifications of the radiation transport equation (RTE). Recall that the RTE describes the conservation of light radiance. Here $E(\boldsymbol{r},t)$ is the light electric field at time $t$ and position $\boldsymbol{r}$, and $\langle\rangle$ denotes the ensemble average (approximated by a time average for the data presented herein). As was the case for the RTE, the correlation transfer equation can be further reduced to a correlation diffusion equation after several assumptions are made [68, 69, 102, 103].

For an optically homogeneous, dynamic, turbid medium, the correlation diffusion equation that governs the behavior of the un-normalized electric field autocorrelation

function is [102, 103]:

$$\left[\mathrm{D}\nabla^2 - \nu\mu_a - \frac{\alpha}{3}\nu\mu_s'\kappa_0^2\langle\Delta r^2(\tau)\rangle\right] G_1(\boldsymbol{r},\tau) = -\nu S(\boldsymbol{r}). \quad [71]$$

Here $\mu_a$ [cm$^{-1}$] and $\mu_s'$ [cm$^{-1}$] are the tissue absorption and reduced scattering coefficients, respectively; $D = \nu/3(\mu_s' + \mu_a)$; $\nu$ is the speed of light in the tissue equal to the speed of light divided by the tissue index of refraction, $n$; $\kappa_0$ [cm$^{-1}$] is the magnitude of the optical wave vector, $2\pi n/\lambda$, and $\lambda$ is the wavelength of incident light; $\alpha$ represents the probability that a scattering event in the sample is off a moving scatterer; $\langle\Delta r^2(\tau)\rangle$ [cm$^2$] is the mean-squared displacement of the moving scatterers in time $\tau$. The main *moving* scatterers in tissue detected by DCS are red blood cells. Note that there is no explicit time-dependence ($t$) in Equation 71, which results from the assumptions that the light sources are CW and that the tissue dynamics are in a quasi-steady state, i.e., the scatterer dynamics are not changing over the time scale of the measurement. Also, note that in the limit that $\tau$ approaches zero, we obtain the photon diffusion equation for a continuous wave light source.

The derivation of Equation 71 and its corresponding assumptions have been described in depth elsewhere by [68, 69, 103]. Briefly, for Equation 71 to be accurate, photon propagation must be well-described as a diffusive process (i.e., the photon diffusion equation for the fluence rate should be valid), the correlation time $\tau$ must be much less than the time it takes for the scatterers to move the wavelength of light ($k_0^2\,\langle\Delta r^2(\tau)\rangle \ll 1$), and, importantly, the scatterer dynamics (i.e., $\langle\Delta r^2(\tau)\rangle$) must be isotropic. In tissue, we assume that because the capillary network is so complex and convoluted, the distribution of directions for red blood cell propagation is approximately

uniform. Thus, the motion of blood cells in tissue can be approximated as being isotropic. In larger arteries and veins, the isotropic dynamics assumption is likely violated, but because the high concentration of blood in these vessels strongly absorbs the light, most of the DCS signal will come from the capillaries, arterioles, and venules.

Notice that the correlation diffusion equation has the same form as the frequency-domain photon diffusion equation. Thus, the form of the solutions we found for the photon diffusion equation will be the same as for the correlation diffusion equation. In all studies presented in this dissertation, we assume a semi-infinite homogeneous medium with a tissue-air planar interface geometry in the plane $z = 0$. Additionally, we employ a CW point source of the form $S(r) = S_0\delta(x, y, z - z_0)$ and use the extrapolated-zero boundary condition wherein $G_1(z = -z_b, \tau) = 0$ (see Chapter 2, Section 2.1.3). The semi-infinite solution of $G_1(\boldsymbol{r}, \tau)$ to the correlation diffusion equation given this boundary condition is obtained using the method of images [108]:

$$G_1(r, \tau) = \frac{3\mu_s' S_0}{4\pi}\left(\frac{e^{-\kappa(\tau)r_1}}{r_1} - \frac{e^{-\kappa(\tau)r_2}}{r_2}\right). \quad [72]$$

Here $\kappa^2(\tau) = 3\mu_s'(\mu_a + \frac{1}{3}\alpha\mu_s' k_0^2\langle\Delta r^2(\tau)\rangle)$; $r_1$ and $r_2$ [109] are the distances between the detector and the real-source/image-source, respectively, i.e., $r_1 = \sqrt{r_2^2 + z_0^2}$ and $r_1 = \sqrt{r_2^2 + (z_0 + 2z_b)^2}$; $z_0 = 1/\mu_s'$ [109] is the depth at which a collimated source on the tissue surface can be approximated as a point source; $z_b = 2.17/\mu_s'$ [109] in the case of refraction indices of tissue and air (equal to 1.4 and 1.0, respectively). The parameters $\langle\Delta r^2(\tau)\rangle$ and $\alpha$ are related to the dynamics of the tissue. Thus, by fitting the measured $G_1(r, \tau)$ for these parameters, we determine information about blood flow in tissue.

Before going further, we stress that our instrumentation measures the intensity temporal autocorrelation function, while the correlation diffusion equation applies to the electric field temporal autocorrelation function. To compare theory with experiment, the intensity autocorrelation function must related to the normalized electric field temporal autocorrelation function, $g_1(\boldsymbol{r},\tau) = \langle E(\boldsymbol{r},t)E^*(\boldsymbol{r},t+\tau)\rangle / \langle |E(\boldsymbol{r},t)|^2 \rangle$. This connection is derived via the Siegert relation [110], $g_2(\boldsymbol{r},\tau) = 1 + \beta |g_1(\boldsymbol{r},\tau)|^2$. Here β is a constant that depends on the source coherence, detection optics, ambient light and other external factors. $\beta$ is usually approximately $1/N$, where $N$ is the number of detected speckles (or modes) [69, 111]. Experimentally, we can determine $\beta$ from the intercept of the measured $g_2(\boldsymbol{r},\tau)$ as the delay time, $\tau$, approaches zero[4].

The Siegert relation is valid if the electric field, $E(\boldsymbol{r},t)$, is a Gaussian distributed variable with zero mean [110, 112]. However, in tissue, some light arriving at the detector has only undergone static scattering. Thus, strictly speaking, the Siegert relation cannot be perfectly valid [69, 103]. Some techniques are available for addressing this problem, but, practically speaking, the contribution of statically-scattered light is a small enough fraction of the detected light in our experiments so that the Siegert relation is approximately accurate.

From many experimental observations of the intensity autocorrelation function on human subjects, we have found the mean squared displacement, $\langle \Delta r^2(\tau) \rangle$, to be linearly proportional to the lag time, $\tau$, i.e., $\langle \Delta r^2(\tau) \rangle$ behaves in a manner formally similar to the mean-squared displacement of a particle exhibiting Brownian motion [61, 62, 69, 102,

[4] In a typical experimental setup discussed within this dissertation, single mode detection fibers are used. Single mode fibers allow transmission of two orthogonal polarization modes, thus $\beta \approx \frac{1}{2} = 0.5$.

103]. Thus, we define $\langle \Delta r^2(\tau) \rangle$ to take the form of $6D_B\tau$, where $D_B$ is an *effective* Brownian diffusion coefficient. Note that, in a typical experiment with a DCS probe on a human forehead, this effective diffusion coefficient is approximately two orders of magnitude greater than the traditional definition of the Brownian diffusion coefficient of a particle the size of a red blood cell in blood[5] [68, 113].

In order to get a sense of how the absorption and scattering coefficients, source-detector separation, and tissue dynamics (here we group $\alpha$ and $D_B$ together to describe the tissue dynamics) affect the decay rate of the electric field autocorrelation function, I have varied each parameter independently and plotted the resultant $g_1(\tau)$ (see Figure 9). When varying one parameter, the other parameters were fixed to typical values for an adult human head, i.e., $\alpha D_B = 1\times10^{-8}$ cm$^2$/s, $\mu_a(785nm) = 0.1$ cm$^{-1}$, $\mu_s'(785nm) = 10$ cm$^{-1}$, $r = 2.5$ cm. It is evident from this figure that the absorption coefficient, varied within a reasonable range, has little affect on the decay of $g_1(\tau)$. On the other hand, the reduced scattering coefficient, the source-detector separation, and the tissue dynamics have a profound affect on $g_1(\tau)$ decay. Higher values of the absorption coefficient cause $g_1(\tau)$ to decay a little slower, while higher values of $\alpha D_B$, $\mu_s'$, and $r$ cause the curve to decay faster. Of course, the source-detector separation, $r$, is known to the experimenter and so causes minimal error. Sometimes, $\mu_s'$ is also known to the experimenter from independent DOS measurements.

## 3.2 Previous validation studies

[5] To get an idea of the magnitude of the $D_B$ for a red blood cell, I consider a red blood cell in water at room temperature and employ the Einstein-Stokes equation, $D_B = k_B T/6\pi\eta r$. For simplicity, I assume the red blood cell is a perfect sphere of radius 5 μm and that the viscosity of water at 293 K (20°C) is $1\times10^{-3}$ kg/m/s, thus $D_B \approx 8.6\times10^{-10}$ cm$^2$/s.

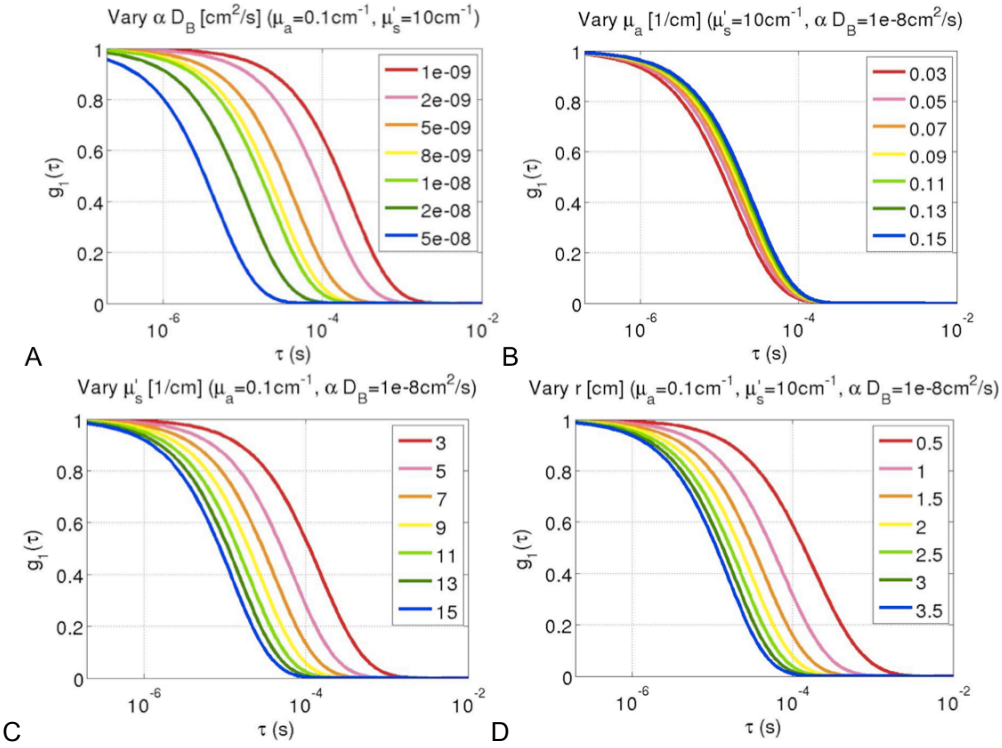


Figure 9, Dependence of the normalized electric field autocorrelation function, $g_1(\tau)$ on (A) $\alpha D_B$, (B) $\mu_a$, (C) $\mu_s'$, and (D) source-detector separation, $r$. When varying one parameter, the other parameters were fixed to typical values for an adult human head, i.e. $\alpha D_B = 1\times10^{-8}$ cm$^2$/s, $\mu_a(785nm) = 0.1$ cm$^{-1}$, $\mu_s'(785nm) = 10$ cm$^{-1}$, $r = 2.5$ cm.

For a given source detector separation and fixed absorption and scattering coefficient, the decay rate of the autocorrelation function is dictated by the tissue dynamics, i.e., blood flow in tissue. Thus, we define a blood flow index, $BFI \equiv \alpha D_B$, with units of cm$^2$/s, to quantify this decay rate. BFI reflects CBF, and changes in BFI relative to baseline measurements (i.e., rBFI) reflect analogous changes in CBF (i.e., rCBF) [114]. Although this data analysis approach is empirical, numerous studies have validated it as a measure of relative blood flow. These studies and their findings are summarized in Table 2. This dissertation highlights two validation studies conducted on pediatric populations in Sections 5.1 and 5.2.

## 3.3 Summary

DCS detects changes in blood flow *directly* by monitoring temporal fluctuations of scattered light. It does not rely on tracers to indirectly infer information about CBF, and it can be employed continuously to provide information about *microvascular* hemodynamics. DCS continuously monitors relative changes in microvascular CBF as opposed to DOS that monitors cerebral blood oxygen saturation and volume.

| | Population | Perturbation | Modality | Correlation Coefficient | Slope | References | Group |
|---|---|---|---|---|---|---|---|
| Animals | Mouse Tumor | PDT | Power Doppler Ultrasound | N/A | 0.97 | Menon C et al., Cancer Res., 2003 | UPenn |
| | Rat | Hypocapnia | Laser Doppler | 0.94 | 1.3 | Durduran T. PhD Dissertation, UPenn, 2004 | UPenn |
| | Mouse Tumor | PDT | Doppler Ultrasound | N/A | Agreement | Yu G et al., Clin. Cancer Res., 2005 | UPenn |
| | Mouse Tumor | Antivascular therapy | CEUS | N/A | Agreement | Sunar U et al., Opt. Expr., 2007 | UPenn |
| | Piglet Brain | Traumatic Brain Injury | Fluorescent Microspheres | 0.63 | 0.4 | Zhou C et al., J. Biomed. Opt., 2009 | UPenn |
| | Rat Brain | Hypercapnia | ASL-MRI | 0.81-0.86 | 0.75 | Carp S et al, Biomed. Opt. Expr. 2010 | MGH |
| | Mouse Brain | Femoral Artery Occlusion | Laser Doppler | > 0.8 | 0.96-1.07 | Mesquita RC et al., Biomed. Opt. Expr. 2010 | UPenn |
| | Piglet Brain | Hypercapnia/Carotid Occulsion | Time-Domain NIRS with ICG | 0.98 | 0.98 | Diop et al, Proc SPIE 2011 | Lawson |
| Humans | Premature Brain | Absolute Baseline | TCD US(MCA Velocity) | 0.91 | 0.9 | Buckley EM et al., Opt. Expr., 2009 | UPenn |
| | Premature Brain | Absolute Baseline | TCD (MCA Velocity) | 0.53 | N/A | Roche-Labarbe N et al., Human Brain Map., 2010 | MGH |
| | Term Brain | Hypercapnia | ASL-MRI | 0.7 | 0.85 | Durduran T et al., J. Biomed. Opt., 2010 | UPenn |
| | Child Brain | Hypercapnia | VENC MRI-Jugular | 0.86 | 0.85-1.03 | Buckley EM et al., unpublished | UPenn |
| | Calf Muscle | Cuff inflation/deflation | ASL-MRI | > 0.77 | 1.5-1.7 | Yu G et al., Opt. Expr., 2007 | UPenn |
| | Adult Brain | Pressors & Hyperventilation | Xenon-CT | 0.73 | 1.1 | Kim MN et al., Neurocrit. Care, 2010 | UPenn |
| | Adult Brain | Acetazolamide | TCD (Velocity) | N/A | Agreement | Zirak et al., Biomed. Opt. Expr., accepted | ICFO (Spain) |
| | Adult Brain | Hypercapnia/Hyperoxia | ASL-MRI | 0.95 | 0.3 | Durduran T et al., unpublished | UPenn |
| | Adult Brain | Breath-Holding | TCD (Velocity) | 0.83 | 1.13 | Mesquita RC et al., unpublished | UPenn |
| | Adult Brain | Head-of-Bed | TCD (Velocity) | 0.85-0.87 | 2.3-2.9 | Mesquita RC et al., unpublished | UPenn |

Table 2, Summary of DCS validation studies against various other modalities. Red text indicates clinical studies, whereas black indicates healthy volunteers/animal studies. Slope refers to the slope of the linear regression between DCS and the other modality.

# 4 Hybrid DOS/DCS Instrumentation

A hybrid DOS/DCS instrument has been designed in our laboratory for translation to the clinic [61, 111, 115]. I have worked on its construction and maintenance: I have also worked in a similar fashion on two other hybrid DOS/DCS instruments developed in our laboratory. This chapter describes these instruments. I will refer to these instruments, respectively, as the homodyne, heterodyne, and ISS devices. A subsection of detailed description is devoted to each instrument.

## 4.1 Homodyne Hybrid Device

The homodyne instrument consists of a homodyne detection DOS device combined with a DCS module. In the DOS homodyne detection scheme, as seen in Figure 10, phase-shifted light is detected and the resulting electronic signal is amplified and sent to the RF input of an in-phase/in-quadrature (IQ) demodulator. The IQ demodulator is *the heart of a homodyne instrument*. The outputs of the IQ demodulator,

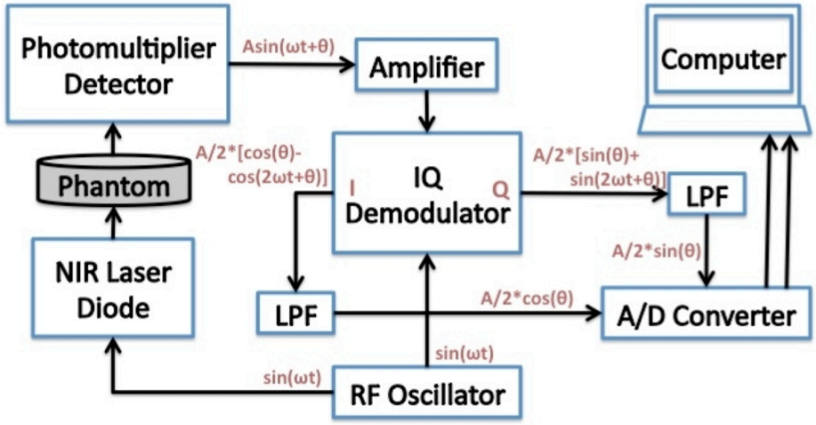


Figure 10, Illustration of a typical homodyne detection scheme used to extract $A$ and $\theta$, the amplitude attenuation and phase shift of light obtained after passing through a highly scattering medium. Abbreviations: NIR = Near-Infrared, LPF = low pass filter, RF = radio frequency, IQ = In-Phase/In-Quadrature, A/D = Analog-to-Digital.

after passing through a low pass filter (LPF), are the sine and cosine components of the signal amplitude, which can be used to derived the amplitude attenuation ($A$) and phase shift ($\theta$) of the detected signal, i.e., $A = \sqrt{I^2 + Q^2}$ and $\theta = \tan^{-1}(Q/I)$ (see Section 2.1.3). The $I$ and $Q$ signals are sent to an analog-to-digital converter for transmission to a computer.

A schematic of the front panel of the home-made instrument is shown in Figure 11. The components are mounted within a 19" rack-mount cart (Hammond Manufacturing, Ltd). Each individual DOS component, except for the Analog-to-Digital converter, is stored in a Nuclear Instrumentation (NIM) bin (Mech-tronics), shown by white rectangles in the figure. These bins provide a means for easily supplying power to each box (module), and they provide excellent shielding from electromagnetic noise.

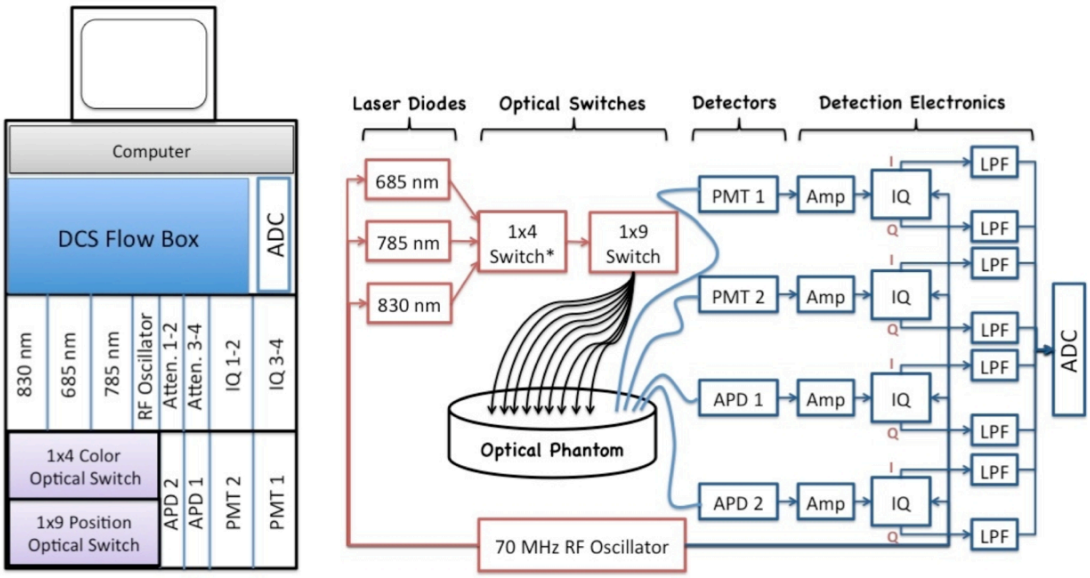


Figure 11, (Left) Front panel of the homodyne instrument consisting of both DOS and DCS modules. (Right) Wiring schematic of the DOS module of the homodyne instrument. Abbreviations: DCS = diffuse correlation spectroscopy, ADC = Analog-to-Digital converter, Atten = Electronic Attenuators, APD = Avalanche photodiode, PMT = Photomultiplier tube, Amp = Amplifier, LPF = low pass filter, RF = radio frequency, IQ = In-Phase/In-Quadrature.

The instrument is bulky, but it is, nevertheless, portable and robust for patient measurements in the clinic.

A schematic of the DOS module is shown on the right of Figure 11. The DOS module consists of three diode lasers, two optical switches, and 4 optical detectors with corresponding detection electronics. The 1x4 switch (FSM-14, Piezosystem Jena Inc) is used to alternate between light source wavelengths sent to the tissue (3 switch inputs for the 3 DOS diode lasers, plus an additional input for the DCS laser), while the 1x9 switch (FSM-19, Piezosystem Jena, Inc.) is used to send light to up to 9 different spatial positions on the optical probe(s). On the detection side are two large diameter avalanche photodiodes (APDs) and two photomultiplier tubes (PMTs). The electronic output of these detectors is amplified and then sent to an I/Q demodulator. Detailed specifications of major instrument components are described below.

**Laser Diode Sources**

The homodyne DOS module consists of three pigtail coupled diode lasers from OZ Optics that operate at 685 nm (ML1413R, Mitsubishi Electric), 785 nm (DL-4140-001S, Sanyo Electric Co., Ltd.), and 830 nm (DL-8032-001, Sanyo Electric Co., Ltd.), respectively. These diodes are driven using either homemade [116] or commercial drivers (LD-1100, Thorlabs), depending on their type.

A high-power (17dBm) sinusoidal radio-frequency (RF) oscillator (VSA-70009, Wilmanco) amplitude modulates the lasers at 70.009 MHz. This oscillator is stable within $\pm$0.003% over a very wide temperature range. The RF oscillator signal voltage is combined with the DC driving component that drives the laser in continuous wave (CW)

mode; combination is accomplished using a bias-tee from Minicircuits (ZFBT-4R2G+).

For optimal detection of this modulated laser light, long-term stability and high modulation-depth is required. To test modulation depth, a PIN diode enables easy conversion of an optical signal to an electronic one that is viewable on an oscilloscope. The modulation-depth, $\%Mod$, is defined as $\%Mod = \frac{V_{pp/2}}{V_{avg}} \times 100\%$ where $V_{pp}$ is the peak-to-peak voltage, and $V_{avg}$ is the DC mean of the modulated laser light signal. By manipulation of the DC operating current of the driver and manipulation of the strength of the RF modulation, one may obtain a desired $\%Mod$ of close to 100% while still optimizing output CW power. Typically, these lasers operate at an average power that is approximately one-half to one-quarter of the company specified CW power. Power output ranges from 10 to 40 mW.

**Optical Switch**

The 1x4 and 1x9 multimode optical switches from Piezosystems Jena Inc have a fast switching time ($\sim 2$ ms) and low insertion loss ($\sim 1.4$ dB). These switches are coupled to optical fibers with core diameter of 200/220 $\mu$m. The switches can be controlled electronically with four 5 V TTL signals.

**Detectors**

The homodyne DOS module consists of four detectors, 2 APDs and 2 PMTs. The APDs (C5331, Hamamatsu Photonics) have a 1.5 mm active area and come packaged with a high-speed/high-sensitivity current-to-voltage amplifier circuit. They were chosen for their high photo-sensitivity in the NIR (i.e., greater than 0.5 A/W in the wavelengths we

are interested in) and for their ability to operate with high efficiency at 70 MHz.

In the low photon count detection limit (in the NIR), two R928 photomultiplier tubes with extended red sensitivity from Hamamatsu Corporation were chosen. This detector features a quantum efficiency (i.e., the number of electrons produced per photon detected) of 1 to 7% in the wavelength range of interest (680-830nm) and a photosensitivity of ~0.02 A/W. Additionally, it features a very low noise equivalent power of $1.3\times10^{-16}$ W (i.e., the amount of light required to produce a signal-to-noise ratio of unity). For these reasons, as well as cost, this PMT appears to be the detector of choice in NIR DOS systems [77, 117].

**Detection Electronics**

The PMT and APD output is an electronic signal proportional to the incoming optical signal. This electronic signal is bandpass filtered at 70 MHz with a pass band of plus or minus 7 MHz (Minicircuits SBP-70), amplified 24 dB (ZFL-500LN, MiniCircuits), and then amplified 19 dB (ZFL-500HLN, Minicircuits) again (amplification in series reduces noise), before passing to the I/Q demodulator. As mentioned previously, the I/Q demodulator is the heart of the homodyne device. It extracts the variations in amplitude and phase of the detected signal using a local oscillator reference. The model we used in our instruments (ZFMIQ-70D, Mini-Circuits) consists of a 90° splitter, two double balanced mixers, and a 0° splitter/combiner as seen in Figure 12 designed to work optimally at 70 MHz. With local oscillator (LO) and detected signal (RF) as inputs (both driven at carrier frequency $\omega$) the outputs $I$ and $Q$ contain (among other things) the sine and cosine components of the complex RF signal. To extract amplitude and phase of this RF signal, $I$ and $Q$ are both fed to a low-pass filter (SLP-30, MiniCircuits) in order to remove

the $2\omega$ frequency component. After filtering the $I$ and $Q$ signals, the amplitude attenuation and phase shift of the detected light are obtained using $A = \sqrt{I^2 + Q^2}$ and $\theta = \tan^{-1}(Q/I)$.

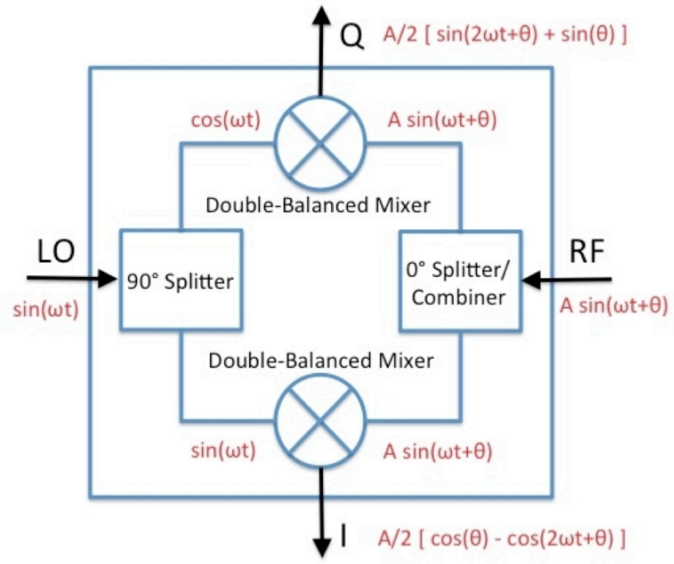


Figure 12, Schematic diagram of an I/Q demodulator for use in homodyne detection. Inputs, LO and RF, come from the oscillator and detected signal, respectively. The outputs, $I$ and $Q$, can be combined to extract the amplitude attenuation, A, and phase shift, $\theta$, of the detected signal.

**Analog-to-Digital Converter**

After low-pass filtering, the $I$ and $Q$ signals from each detector are sent to an analog-to-digital converter (ADC) for read-in by a computer. A 16-bit ADC from National Instruments, model NI-USB-6251, was chosen for this purpose due to its fast sampling rate, large number (8) of analog inputs, and USB communication with the computer. At the ADC input, additional 100 Hz low-pass filters were inserted for further noise rejection (Figure 13).

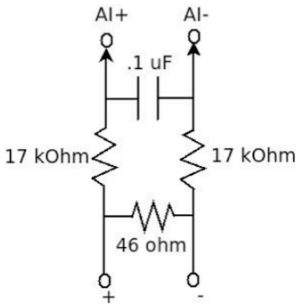


Figure 13, ~100 Hz low pass filter designed for the ADC board input.

**DCS Module**

The DCS module (seen in Figure 14 and detailed in Figure 15) consists of two long-coherence-length lasers with optical isolators (CrystaLaser, RCL785S-100-SO) operating at 785 nm to deliver light to the tissue. The coherence length of the lasers (> 50 m) is chosen to be much greater than the mean pathlength a photon travels before detection (on the order of 10 centimeters for neonates) [75, 118]. Additionally, the wavelength of 785 nm was chosen for its availability, as well as its proximity to the isosbestic point around 800 nm, i.e., where the absorption spectra of oxy- and deoxy-hemoglobin intersect (see Figure 1). This light can either be switched on/off with a TTL

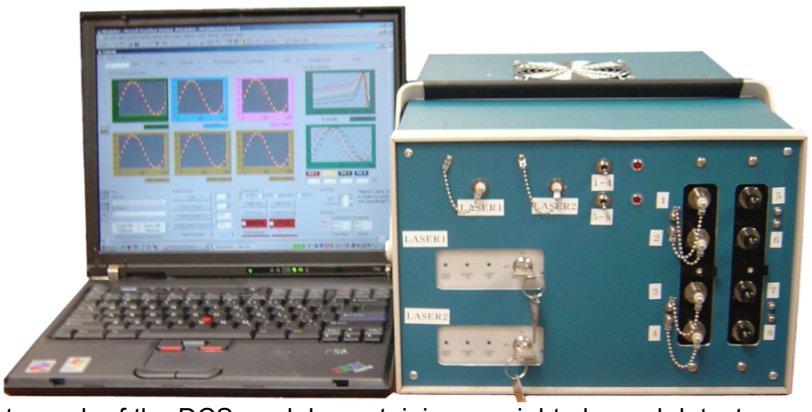


Figure 14, Photograph of the DCS module containing an eight-channel detector array.

signal directly coupled to the laser, or it can remain on and be turned on/off by the 1x4 color optical switch in the DOS module.

DCS light is detected using up to eight single mode fibers sent to two 4-channel arrays of fast photon counting silicon avalanche photodiodes (SPCM-AQ4C, Perkin-Elmer, Canada). These detectors were chosen for their ability to detect single photons with approximately 50% photon detection efficiency within the NIR wavelength we employ (785 nm). They have a low dark count rate of 500 counts/sec (i.e., low for APDs), as well as the capability of detecting up to 2 Megacounts/sec per channel; they are powered by three DC power supplies (operating at +2V, +5V and +30V, (Part numbers: LPT81 Astec, DMS-PS1-CM Murata/Datel, HSB28-1.0 Lambda, respectively). The detectors output a 25 ns TTL pulse for each detected photon via an SPCM-AQ4C-IO module with convenient BNC connector outputs. The TTL pulses are transmitted to two custom-built 4-channel multi-tau correlator boards (FLEX03OEM-8CH, correlator.com, Bridgewater, NJ) that derive the intensity autocorrelation function based

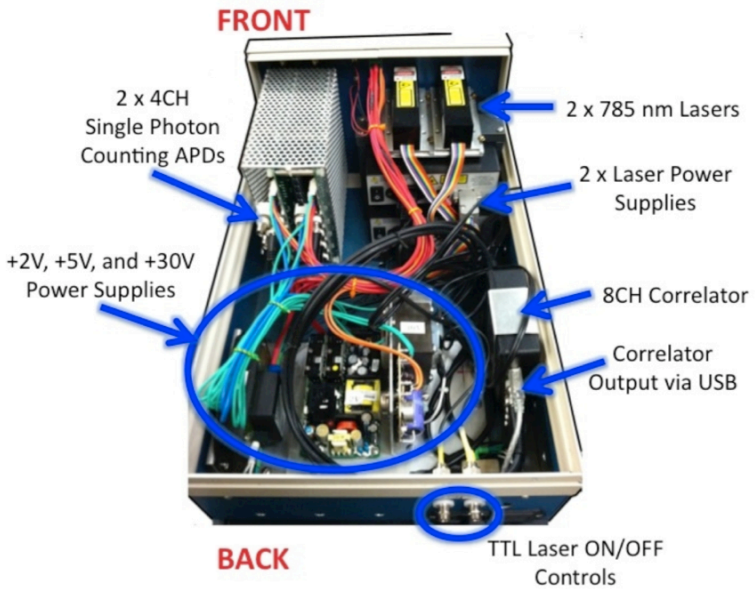


Figure 15, Interior of DCS flow box.

on the photon arrival times [111, 115, 119]. The intensity autocorrelation function is then transmitted to a computer via a USB 2.0 port. Updated data from the correlator is transmitted every 47 ms.

## 4.2 Heterodyne Hybrid Device

The heterodyne hybrid instrument consists of a heterodyne detection DOS device combined with a DCS module. A schematic of the front panel of the instrument is shown in Figure 16 (left). This instrument is much smaller than the homodyne instrument and has been mounted on a more portable cart (Convoi, Anthro Corporation). As was the case with the homodyne instrument, the DOS components of the heterodyne system are mounted within a 19" rack-mount cart and stored in NIM-bins for RF isolation. The DCS module in the heterodyne instrument is identical to the DCS module in the homodyne instrument (see Section 4.1). The remainder of this section will discuss the intricacies of

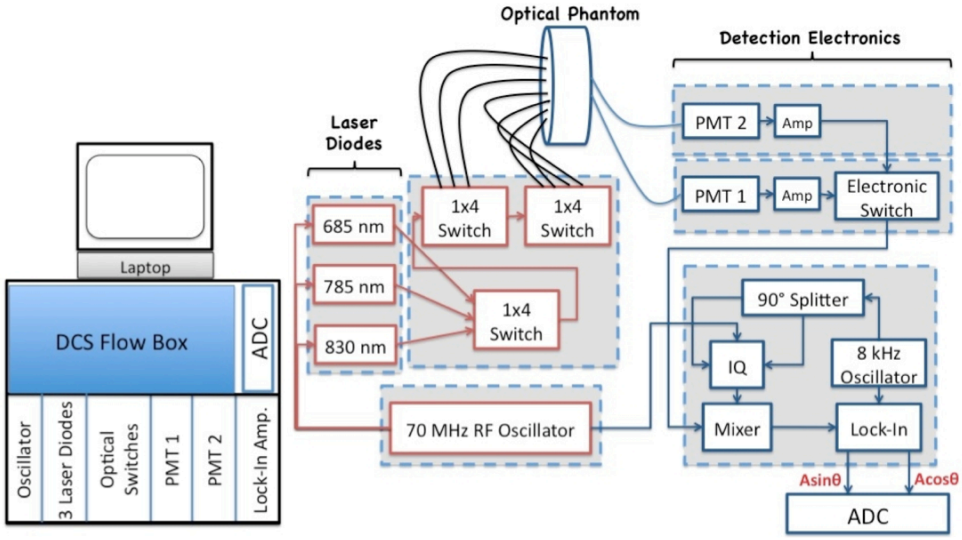


Figure 16, (Left) Front panel of the heterodyne instrument consisting of both DOS and DCS modules. (Right) Wiring schematic of the DOS module of the heterodyne instrument. Abbreviations: DCS = diffuse correlation spectroscopy, PMT = photomultiplier tube, ADC = Analog-to-Digital Converter, RF = radio frequency, Amp = amplifier.

the heterodyne DOS module.

For heterodyne detection, an RF *and* an audio frequency are employed as seen in Figure 17. Heterodyne systems have the advantage of phase shift determination at a lower frequency thus improving accuracy. The RF oscillator drives the laser diode at a carrier frequency $\omega_1$. Light from the laser diode is delivered to the tissue/sample and collected via optical fibers some distance away. The detected signal has some amplitude attenuation ($A$) and phase shift ($\theta$) as compared to the input signal, although it still oscillates at frequency $\omega_1$. This phase-shifted/ amplitude-attenuated signal is detected by a photomultiplier tube (PMT), amplified and then sent to a frequency mixer that acts as a downconverter. At the mixer, the detected $\omega_1$ signal is combined with a signal of frequency $\omega_1 - \omega_2$ created by a single sideband system (highlighted in grey in Figure 17 (top) and detailed in Figure 17 (bottom)). Here $\omega_2$ is an audio carrier frequency, provided by a second sinusoidal oscillator. The output from the mixer is filtered such that only the low frequency component $\omega_2$ remains. Thus, the resultant signal still contains amplitude attenuation and phase shift information at the audio frequency $\omega_2$. This signal is then sent to a phase sensitive detector (PSD), or lock-in amplifier, to extract amplitude attenuation ($A$) and phase shift ($\theta$) by comparing with the carrier reference frequency. The outputs of the PSD are the same as the homodyne detection, namely $I = A\sin\theta$ and $Q = A\cos\theta$. These outputs get sent to an A/D converter and to a computer to extract the values of $A$ and $\theta$.

Figure 16 (right) shows a schematic of the DOS module for the heterodyne instrument. The source side consists of the same three diode lasers as the homodyne instrument (see Section 4.1), operating at 685 nm, 785 nm, and 830 nm, respectively,

and amplitude modulated by a high-power 70.055 MHz RF oscillator (VSA-70055, Wilmanco). These lasers are all confined within a single NIM-Bin to save space, as opposed to the homodyne instrument in which each laser has its own NIM-Bin.

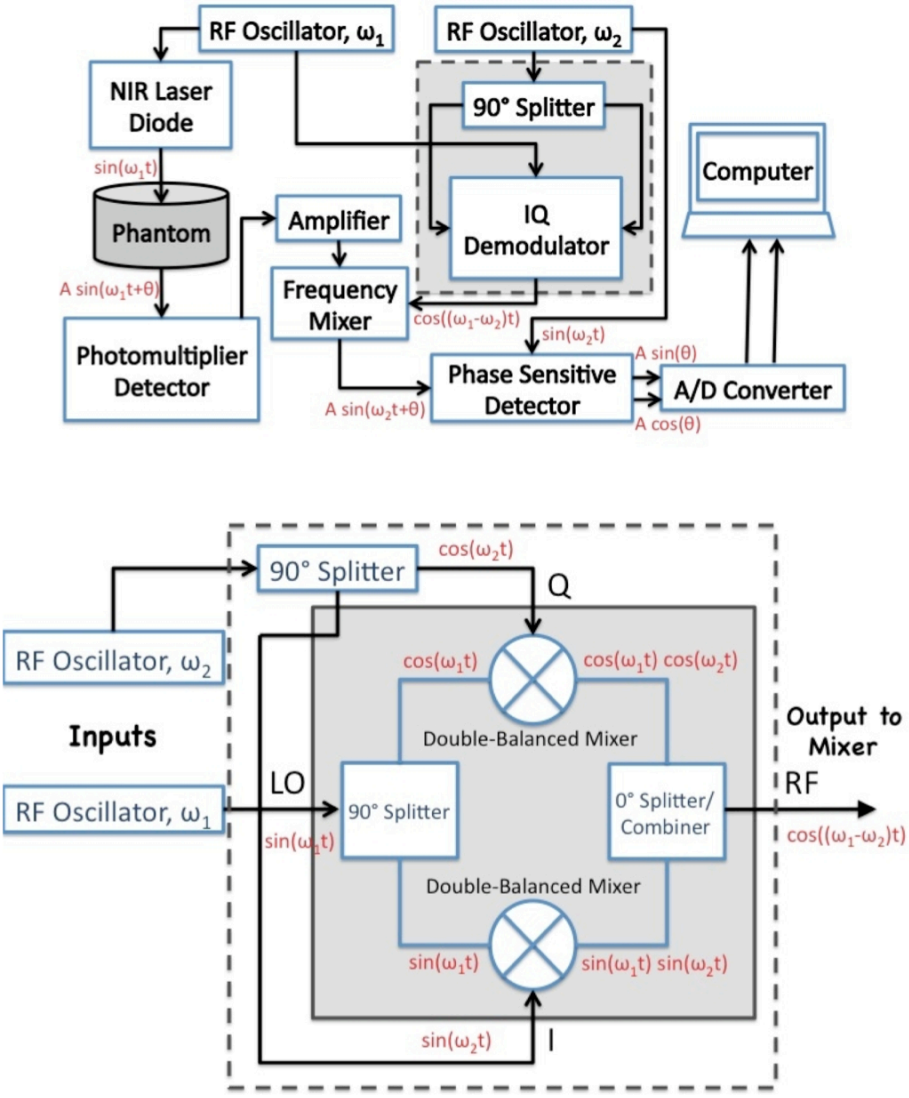


Figure 17, (TOP) Illustration of a typical heterodyne detection scheme used to extract $A$ and $\theta$, the amplitude attenuation and phase shift of light obtained after passing through a highly scattering medium. Abbreviations: NIR = Near-Infrared, RF = radio frequency, IQ = In-Phase/In-Quadrature, A/D = Analog-to-Digital. (BOTTOM) A single sideband system used to down convert the RF carrier frequency $\omega_1$ to the difference between $\omega_1 - \omega_2$.

The DOS laser outputs are sent to a 1x4 optical switch used to switch through each DOS wavelength (with an extra location for the DCS laser). The output of this color switch is sent to two 1x4 optical switches connected in series. These two switches are used to send light to up to 7 different source locations.

**Detection Electronics**

On the detection side, the heterodyne instrument employs two photomultiplier tubes (R928, Hamamatsu Photonics, discussed in Section 4.1). The detection electronics are designed to access one detector at a time. Thus the electronic output of each detector is first amplified (36 dB, part number C-5594, Hamamatsu Photonics) and then sent to a digitally controlled electronic switch (ZASW-2-50-DR, Mini-Circuits).

The 70.055 MHz output from the electronic switch is sent to a frequency mixer (ZFM-2, Mini-Circuits) where it is combined with a 70.047 MHz reference signal created by a single sideband system (discussed in Section 2.2). After passing through the low

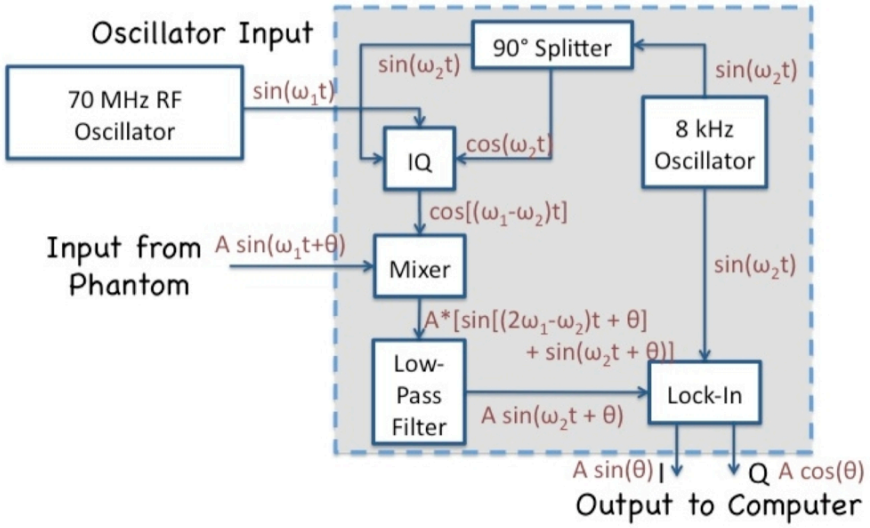


Figure 18, Detailed schematic of detection electronics NIM-Bin in heterodyne DOS module.

pass filter, the output of the mixer, as seen in Figure 18, oscillates at the 8 kHz audio frequency, and it contains the amplitude attenuation and phase-shift information needed from the detected signal. This signal is then transmitted to the lock-in amplifier for extraction of amplitude and phase.

**Lock-in Amplifier**

We chose a dual phase lock-in amplifier from Femto (LIA-BVD-150-L) for its small size and onboard reference oscillator (see Figure 19). Additionally, not only does it accept a wide range of voltage inputs (3μV to 1V), it allows for manual and digital setting of the sensitivity range based on the intensity of this input signal.

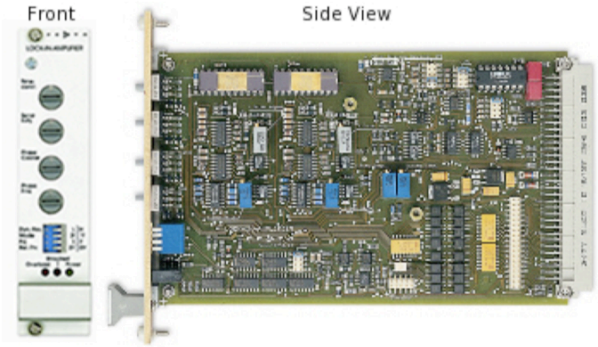


Figure 19, Photograph of the front and side view of the lock-in amplifier from Femto.

## 4.3 ISS Hybrid Device

With the help of a generous donation from the Steve and June Wolfson Family Trust, we purchased a commercial frequency domain DOS device from ISS, Inc. (Imagent™, ISS, Inc.). The device was modified slightly for integration with our DCS modules. This resultant composite instrument has been dubbed in our lab as the "ISS Instrument" (see Figure 20), and the remainder of this section will discuss its specifications. The DCS

module in the ISS instrument is identical to the DCS module in the homodyne instrument (see Section 4.1), thus the majority of this section will focus on the DOS module.

### 4.3.1 ISS Imagent™

The Imagent™ system is a frequency domain instrument, operating at a modulation frequency of 110 MHz, with heterodyne detection at a cross-correlation frequency of 5 kHz [120, 121]. It contains of 16 diode lasers sources (6 x 826 nm, 5 x 688 nm, 5 x 787 nm, respectively) all operating with output power of approximately 5 mW, and it contains two photomultiplier tube detectors, as seen in Figure 20 (right), and a 16-bit analog to digital converter. The 16 sources are rapidly multiplexed in sequence electronically, eliminating the need for optical switches like those used in the homodyne and heterodyne instruments. Approximately 0.32 seconds is required to switch through all 16 sources. This particular instrument can also be expanded to house up to 4 PMTs and 32 diode lasers if desired. Presently, 2 PMTs and 16 diode lasers accommodate our clinical experiments needs.

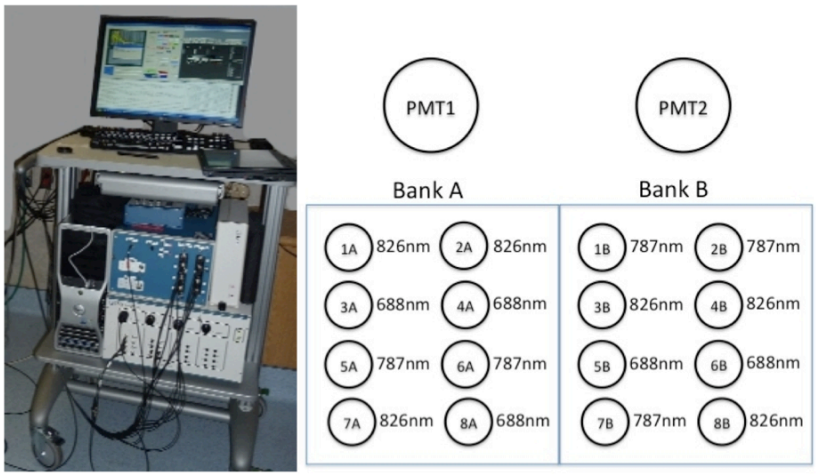


Figure 20, (Left) Photograph of the ISS Instrument. (Right) Schematic of the front panel of the Imagent™, containing16 laser diode sources and 2 PMT detectors.

### 4.3.2 Standard Operation of ISS Hybrid Instrument

For integration with the DCS module, the ISS diode lasers and PMTs are programmed to turn-off when the DCS module is acquiring data. In this way, the ISS lasers do not interfere with the DCS detectors, and the DCS laser does not saturate the ISS detector. To avoid instabilities caused by the warm up time of the PMT, two frames of data are ignored just after the ISS lasers/PMTs are turned on (here I define a frame as one sweep through all 16 lasers, ~ 320 ms). Typical operation of the hybrid ISS instrument is summarized by a flow chart in Figure 21.

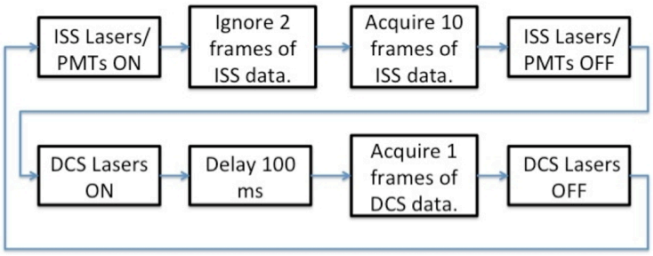


Figure 21, Flow chart describing standard operation of the ISS Imagent DOS module and DCS module in the ISS instrument.

## 4.4 Instrument Performance

To characterize the stability, dynamic range, and accuracy of each of these instruments for determining optical properties, we have quantified performance in phantom and physiological tests on human subjects. The following section describes in detail the tests performed to assess the capabilities of each instrument.

*Stability:* The amplitude/phase data should be stable within 1%/1° for the duration of a typical clinical experiment (approximately 2 to 3 hours). Several factors contribute to signal stability, including but not limited to, the repeatability of the optical

switches and the RF and CW stability of the diode lasers. To test stability, the amplitude and phase of a signal obtained from a solid phantom with static optical properties was observed over a significant time period. Additionally, we measured the long-term stability of the CW power output of the lasers using a power meter.

Figure 22 shows sample signal stability of amplitude and phase obtained on a phantom. Data was acquired at intensities akin to those seen in patient experiments. The data was taken for more than 10 hours and a mean and standard deviation of each parameter were computed during each hour. The amplitude stays stable to within < 1 % within an hour and the phase is constant to within a degree over the entire ten-hour period.

Table 3 summarizes the stability data of both the offsets and signal. Amplitude stability is reported as the average percent variation from the mean; phase stability is reported as standard deviation (in degrees). Stability data was taken at all wavelengths, and the greatest instability is listed in the table. The heterodyne and ISS instruments

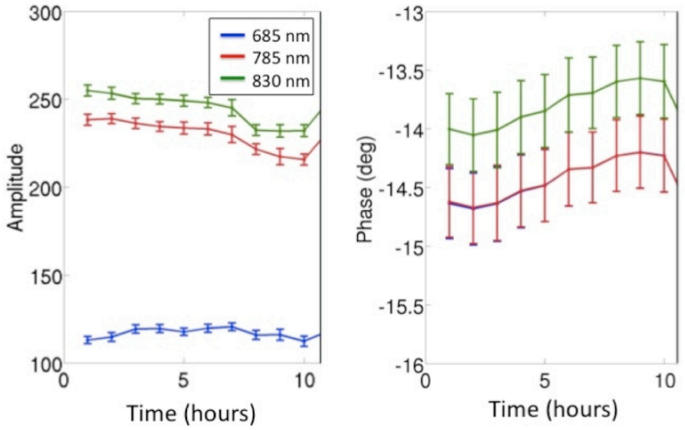


Figure 22, Stability of the AC amplitude and phase on a solid phantom measured with the ISS DOS module. Signal magnitude is typical of that seen in a clinical experiment.

| Instrument | Parameter | PMT 1 | PMT 2 | APD 1 | APD 2 |
|---|---|---|---|---|---|
| Homodyne | Offset Stability- Amplitude (%) | 1.0 | 2.4 | 1.8 | 2.3 |
| | Offset Stability- Phase (°) | 0.5 | 1.5 | 0.7 | 1.3 |
| | Signal Stability- Amplitude (%) | 9.0 | 9.2 | 9.6 | 12.6 |
| | Signal Stability- Phase (°) | 0.8 | 1.2 | 1.1 | 2.75 |
| Heterodyne | Offset Stability- Amplitude (%) | 5 | 5 | | |
| | Offset Stability- Phase (°) | 3.0 | 4.2 | | |
| | Signal Stability- Amplitude (%) | 1 | 1.5 | | |
| | Signal Stability- Phase (°) | 0.4 | 0.7 | | |
| ISS | Offset Stability- Amplitude (%) | -- | -- | | |
| | Offset Stability- Phase (°) | -- | -- | | |
| | Signal Stability- Amplitude (%) | 1.0 | 1.0 | | |
| | Signal Stability- Phase (°) | 0.8 | 1.5 | | |

Table 3, Offset and signal stability of each detector in all DOS instruments discussed. All stability data was acquired over a period of at least 10 hours.

clearly have superior signal stability for all laser wavelengths.

*Dynamic Range:* Attenuation of light falls off exponentially with source-detector separation. Thus a large instrumentation linear range is advantageous for the detection of light in a wide-range of separations. To characterize the dynamic range, the power from the laser is attenuated in 1 dB steps (monitored with an optical power meter), and the intensity and phase detected from the phantom is recorded at each step. Raw $I$ and $Q$ data are adjusted for offset to extend the linear range by subtracting $I_{off}$ and $Q_{off}$, the values of $I$ and $Q$ found when the light source is removed from the setup. New offset subtracted amplitude and phase data are computed via the new values of $I$ and $Q$, namely $I - I_{off}$ and $Q - Q_{off}$ Plotting the input power [dBmW] versus output voltage [dBmV] reveals a range in which the power and voltage are linearly related with a slope of 2 ($P = V^2/R$, thus the $\log(P)$ is proportional to $2\log(V)$). Within this range, the phase should also remain constant. To quantify the dynamic range, we impose a restriction

that, within this range, the phase must be stable to within 1° and the amplitude must not deviate more than 1% from the best linear fit. A setup to test linearity is shown in the left of Figure 23. Sample linearity data obtained from a homodyne detection device is shown in the right of Figure 23. For this particular instrument, the dynamic range of both amplitude and phase extend over approximately 52 dBmV, or about 2.5 orders of magnitude. The effect of offset subtraction on the dynamic range is most notable from data in this figure. Thus, when obtaining experimental data, offset measurements are required. If the offset stability of the instrument is sufficiently low (<1% variation over the duration of the experiment), then a single offset measurement will suffice. If the offset is not stable, it is wise to take offset data intermittently for more accurate assessment of signal changes.

Table 4 summarizes the dynamic range of each instrument discussed in this dissertation. The data was taken with a PMT voltage gain of 800 V for all instruments. For the ISS instrument, the upper limit of the dynamic range could not be reached because of the source fibers that were used. Thus the dynamic range is most likely underestimated. This table shows that all three instruments demonstrate approximately the same linear range, although there is some variation amongst detectors.

*Phantom Experiments*: Once satisfied with stability and the dynamic range of an

| **Instrument Dynamic Range (dB)** | **PMT 1** | **PMT 2** | **APD 1** | **APD 2** |
|---|---|---|---|---|
| Homodyne Instrument | 51.3 | 31.6 | 53.3 | 41.7 |
| Heterodyne Instrument | 55.3 | 48.1 | | |
| ISS Instrument | 45.1 | 46.0 | | |

Table 4, Dynamic range of all detectors in each instrument.

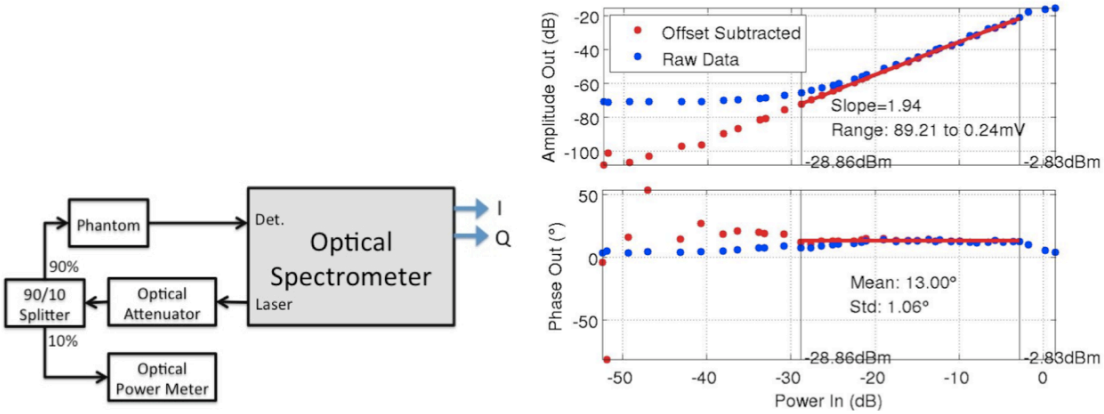


Figure 23, (LEFT) Setup for testing the dynamic range of an optical spectrometer. (RIGHT) Linearity of a homodyne instrument at 830nm. The raw data is shown in blue, while the red data has been adjusted by the offset signal.

instrument, phantom experiments must be performed to test the accuracy of the instrument in extracting accurate optical properties. Typically, a titration of both absorption and scattering of a liquid phantom are performed using ink and Intralipid, respectively. We titrate $\mu_a$ in steps of approximately 0.03 cm$^{-1}$ by adding India ink to a liquid phantom of water and intralipid while keeping $\mu_s'$ constant. To titrate $\mu_s'$, we add additional intralipid to a phantom of intralipid, water, and ink to step $\mu_s'$ in increments of 1-2 cm$^{-1}$. A detailed description of how to make liquid phantoms can be found in [116]. These measurements are unfortunately only approximate, since each batch of intralipid has slightly different optical properties.

Figure 24 demonstrates ink titration data taken with the ISS instrument. Expected values of $\mu_a$ are plotted on the x-axis (the absorbance of ink is measured using a spectrophotometer prior to titration, thus if we know the amount of ink we are adding, we can predict how much $\mu_a$ should change), and measured values are shown on the y-axis. ISS measurements are shown in red (data only obtained at 685 and 830 nm). Presumably, since only the ink concentration was changed, the reduced scattering

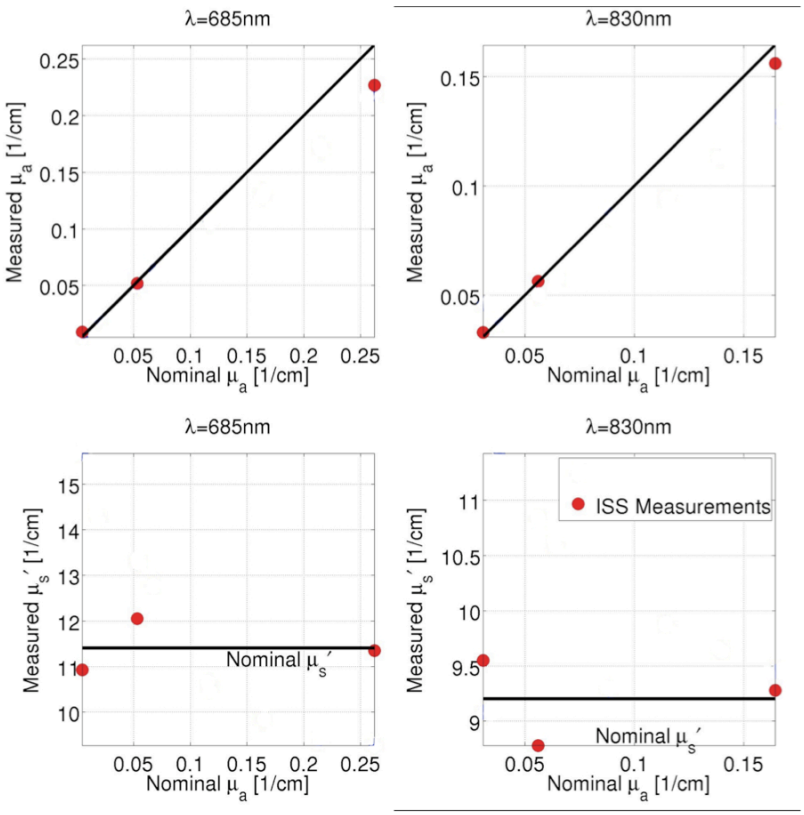


Figure 24, Ink titration results using the ISS instrument (red). Ink was added to titrate $\mu_a$ in three known steps. Expected values of $\mu_a$ are plotted on the x-axis, and measured values are shown on the y-axis. The solid black line indicates perfect agreement between our predicted $\mu_a$ and the measured $\mu_a$ or $\mu_s'$.

coefficient should remain constant throughout titrations. The ISS instrument is thus able to resolve the optical properties of the liquid phantom to within 10% of the expected values.

*Physiologic Experiments*: A blood phantom can be used to test the accuracy of the instrument in addition to Intralipid/ink phantoms. The blood is diluted with water, and then oxygen is bubbled into the blood/water solution. Yeast can be added for blood deoxygenation. A detailed description on the making and the measuring of blood phantoms can be found in the Appendix of Chapter 3 in Regine Choe's PhD Thesis [116].

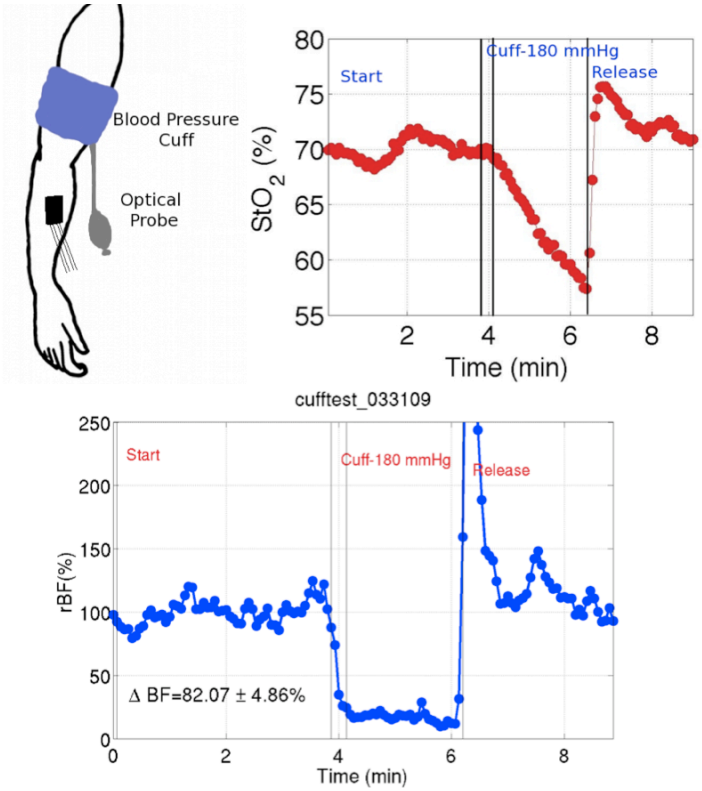


Figure 25, Cuff occlusion test using the ISS instrument. Time series of the changes in tissue oxygen saturation ($StO_2$) and relative changes in arm muscle blood flow (rBF) are shown on left and right, respectively.

Ultimately the goal of these tests is to confirm the validity of the DOS instrument in human and animal experiments. Typically, the optical probe is placed on the forearm and a cuff occlusion experiment is performed similar to that published by Yu *et al* [122, 123]. After a period of baseline monitoring for approximately 5 minutes, a blood pressure cuff is inflated on the upper arm to a pressure of above 180 mmHg to occlude arterial flow for 3 minutes. Following occlusion, one expects to see a stabile baseline, followed by a dramatic drop in tissue oxygen saturation ($StO_2$) of around 20% and a drop in blood flow (BF) of approximately 90%. Total hemoglobin concentration should remain approximately constant. After 3 minutes the cuff is released and recovery is measured for at least 3 minutes. Cuff release causes BF and $StO_2$ overshoot to significantly greater than baseline values. After a few minutes, the signal should return to baseline

values. To test a new optical probe and/or a new DOS instrument, forearm cuff occlusion should be performed to ensure accuracy and reliability. Obviously, results will vary due to physiological differences between subjects. However, the overall trend consisting of a sharp drop in flow and saturation, followed by an overshoot and return to baseline, should be observed in all healthy subjects.

Figure 25 shows sample arm cuff data taken with the ISS instrument. The experiment employed two source detector pairs, both separated 2.5 cm, one for DCS and one for DOS. The modified Beer-Lambert law was used for DOS analysis. Baseline values of tissue oxygen saturation and absorption and scattering coefficients were obtained from literature values. The figure on the left shows $StO_2$ versus time, while the right shows relative change in blood flow versus time. Both time series demonstrate the expected behavior during cuff occlusion. Similar results are found with both the homodyne and heterodyne devices (data not shown).

# 5 Validation of DCS in Critically Ill Neonates

## 5.1 rCBF correlations with Velocity Mapping MRI

Assuring adequate tissue perfusion is central to support of patients in the critical care arena. In particular, information about cerebral blood flow is valuable for assessment of brain perfusion and prevention of secondary injury. As discussed in Section 1.2, very few existing methods, however, provide clinicians bedside access to this information. Currently available perfusion diagnostics are either low-throughput, indirect, expensive, invasive and/or require patient transport [11, 124]. Diffuse correlation spectroscopy (DCS) is a new optical technique (discussed in depth in Chapter 3) that appears to be an excellent tool for assessing cerebral blood flow in a continuous and non-invasive manner at the bedside. The technique, however, must be validated in a variety of clinical settings and against myriad well-established (but still non-ideal) blood flow modalities in order for this new optical tool to gain wide acceptance.

Patients with congenital heart defects represent one population that could benefit greatly from a non-invasive bedside monitor of cerebral blood flow. Recent work, for example, has shown that when compared to healthy full-term children, patients with complex congenital heart defects have a high incidence of peri-operative brain injury and a significantly higher incidence of neurocognitive impairments as compared with healthy full-term children [125-127]. During periods of hemodynamic instability, such as in peri-operative care, a monitor of cerebral blood flow could provide insight into the timing, development, and evolution of these brain injuries

The remainder of this section validates DCS measurement of relative changes in

cerebral blood flow (CBF) against a well-established magnetic resonance technique, phase encoded velocity mapping (VENC MRI) in a population of pediatric patients with congenital heart defects. VENC MRI does not measure cerebral blood flow in the brain; rather, it measures blood flow in the main vessel supplying blood to the brain, i.e., the aortic arch, and in the main vessels draining blood from the brain, i.e., the jugular veins and the superior vena cava. These measures of flow in the jugular veins have been shown to agree strongly with other measures of cerebral blood flow [128, 129]. While VENC MRI provides high-quality, reliable blood flow data, these measurements must be carried out in the MRI scanner making them unsuitable for continuous monitoring. We find that relative changes of blood flow in the jugular veins and superior vena cava correlate strongly with relative changes in cerebral blood flow measured with DCS. These results indicate DCS may be employed as a continuous bedside monitor of CBF in patients with congenital heart defects, as well as in a wide variety of other patients.

### 5.1.1 Materials and Methods

Patients with single ventricle complex congenital heart defects at The Children's Hospital of Philadelphia were recruited for this study (approved by the Institutional Review Board). All measurements were performed on the morning of the patient's staged cardiac surgery. Immediately prior to surgery, general anesthesia was induced via mask induction with Sevoflurane. After intravenous access was obtained, 0.2 mg/kg pancuronium was administered for neuromuscular blockade. After intubation, a nasal endotracheal tube was placed. The patient was subsequently mechanically ventilated and sedation was maintained with 1-2% Sevoflurane while an arterial catheter was placed in an upper extremity. Patients were brought to the MRI scanner and a non-

invasive optical probe was placed on the forehead for continuous optical monitoring. Figure 26 shows the experimental timeline. Briefly, after a 30-minute baseline period of ventilation with $FiO_2$ (fraction inspired oxygen) of 0.21, inspired $CO_2$ was added to the room air mixture to achieve a $FiCO_2$ of approximately 30 mmHg. The $CO_2$ mixture remained on for a 30-minute hypercapnic period to allow for gas equilibration and stabilization of the higher hypercapnic blood flow. During this period of equilibration, anatomical brain MRI was obtained. Non-invasive cuff blood pressures, electrocardiogram, peripheral oxygen saturation, and $FiCO_2$ were monitored and recorded throughout the duration of the study. Arterial blood gases were obtained at the start of the baseline period and at the end of the hypercapnia period to assess changes in the partial pressure of carbon dioxide ($pCO_2$) in the blood.

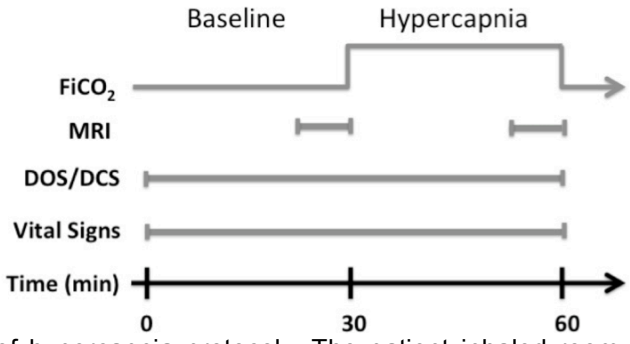


Figure 26, Timeline of hypercapnia protocol. The patient inhaled room air for 30 minutes at which point $CO_2$ was added to the gas mixture for a fraction of inspired $CO_2$ of 30 mmHg.

#### *5.1.1.1 Phase Encoded Velocity Mapping MRI*

To measure blood flow in the main vessels supplying and draining from the brain during both room air inhalation and hypercapnia, a magnetic resonance technique known as phase-encoded velocity mapping (VENC MRI) was employed [130-132]. In brief, the technique relies on the fact that magnetic spins of intravascular protons flowing along a

magnetic field acquire a phase-shift that is linearly proportional to their velocity:

$$\Delta\varphi = \gamma v \delta A_g. \quad [73]$$

Here $\Delta\varphi$ is the phase-shift, $\gamma$ is the gyromagnetic ratio, v is the velocity, $\delta$ is the time between the centers of two magnetic pulses and $A_g$ is the area of one of the gradient pulses. A magnetic field gradient is aligned along the axis of the vessel(s) of interest, namely the aorta, jugular veins, and superior vena cava in our experiments, thereby inducing a phase shift in spins that move or flow along this gradient. The phase shift accumulated by the MRI signal obtained from a specific voxel is proportional to the velocity within that voxel. The direction of flow is aligned with the use of oblique magnetic field gradients. Combined with phase error correction techniques, velocity is accurately measured.

Our investigation used a Siemens 1.5-Tesla Avanto MRI system (Siemens Medical Systems, Malvern, NJ). After localizers in multiple planes, a stack of static, steady-state free precession axial images were acquired spanning the entire thorax and neck. These images evaluated cardiovascular anatomy and were used for localized through-plane velocity mapping. The effective repetition time was the R-R interval (range, 450 to 650 ms). The echo time was 1.5-3 ms; the number of segments per heartbeat was 29; the number of excitations was 3; and the image matrix size was 128 x 128 pixels, interpolated to 256 x 256, with a field of view ranging from 180 to 200 mm and slice thickness of 3 mm. "Multiplanar reconstruction," a software package resident on the Siemens MRI system, used the transverse images to calculate the exact slice position and double-oblique angles to obtain a ventricular outflow tract view and long-axis images of the jugular veins and superior vena cava. If two ventricular outflow tracts

were present, each one was obtained separately. An imaging plane perpendicular to flow was then determined for: (1) the ventricular outflow tract at the sinotubular junction (if two were present, they were each calculated separately); (2) jugular vein above the superior vena cava; and (3) the superior vena cava proximal to the pulmonary artery anastomosis and distal to the innominate and subclavian veins. The retrospective phase encoded velocity mapping sequence was then performed with a repetition time of 35 ms, echo time of 3 ms, number of segments per heartbeat of 3, field of view of 180 mm, a slice thickness of 5 mm, obtaining 20-23 phases depending upon the heart rate utilizing parallel imaging and 5 averages. VENC MRI encoding was 60-90 cm/s.

Quantitative velocities were obtained in a region of interest (ROI) that was semi-automatically traced along the margins of the blood vessel of interest. Blood flow was computed by the sum of the product of the velocities measured in each pixel and the area of each pixel in the ROI. By integrating this flow over the cardiac cycle and multiplying by the heart rate, we obtained an average blood flow in units of liters per minute. The protocol not only included VENC MRI but also a contiguous stack of static, steady state free precession images in the axial plane; this stack was used to locate the exact slice positions for VENC MRI so that this plane was perpendicular to flow.

For each patient, velocity maps were obtained at the sinotubular junction in the aortic root, in the left and right jugular veins, and in the superior vena cava during room air inhalation and during hypercapnia (see). From these maps, we calculated a net flow (as described above) per cardiac cycle. The signal was averaged over multiple cardiac cycles to minimize effects of respiratory motion, but, in the process, averaging also had the advantage of improving the signal-to-noise ratio, yielding an average blood flow

value for each vessel acquired over approximately 1 minute. Thus, we obtained a mean blood flow with units of Liters/minute in the aorta ($BF_{Aorta}$), superior vena cava ($BF_{SVC}$), and by summing the blood flow in the right and left jugulars, the jugular veins ($BF_{Jug}$). Relative changes in blood flow (*rBF*) through these vessels due to hypercapnia were computed using the following formula, $rBF = (BF_{CO2}/BF_{Room\ Air})\times 100\ \%$ . Cerebrovascular reactivity (CVR), defined as the change in blood flow divided by the change in partial pressure of $CO_2$ ( $\Delta pCO_2$ ), was computed as $CVR = (rBF - 100\%)/\Delta pCO_2$.

#### *5.1.1.2 Diffuse Optical and Correlation Spectroscopies*

Optical measurements of both changes in oxy- and deoxy-hemoglobin concentrations and changes in cerebral blood flow were obtained continuously with a custom-made optical probe (Fiberoptic Systems, Inc., Simi Valley, CA). The probe contained two separate source-detector pairs, one for DOS and one for DCS, both separated by 2.5 cm; thus the mean penetration depth of diffusing photons reached cortical tissue. The DCS detector was a bundle of 8 single mode fibers used to improve the signal-to-noise ratio. The probe was molded to conform to the patient's head, and it was secured gently to the forehead with a soft head wrap. Additionally, a fiducial marker was placed over the probe to locate fiber positions on anatomical MRI images.

Optical data were acquired using a hybrid diffuse optical spectrometer, consisting of a commercially available diffuse optical spectroscopy (DOS) system (Imagent, ISS, Champaign, IL) and a diffuse correlation spectrometer (DCS) custom-made in our laboratory. The DOS instrument operates in the frequency domain at 110 MHz with three wavelengths, 686, 786, and 826 nm. It uses a heterodyne detection at 5 kHz to

quantify diffusive wave AC amplitude attenuation, phase shift, and average DC value of the detected light. For DOS data analysis, the modified Beer-Lambert law [91, 133],

$$\log(I(\lambda)/I_0(\lambda)) = r \times DPF(\lambda) \times \Delta\mu_a(\lambda), \quad [74]$$

was employed to compute changes in the absorption coefficient, $\Delta\mu_a(\lambda)$. Here $\mathrm{I}(\lambda)$ is the DC light intensity measured at wavelength λ and time $t$, $\mathrm{I}_0(\lambda)$ is the mean DC light intensity measured at wavelength λ during the five minutes of room air inhalation when VENC MRI scans were obtained; $DPF(\lambda)$ is the wavelength dependent diffuse pathlength factor accounting for the increase in photon pathlength due to multiple scattering, equal to 5.4, 5.0, and 4.7 for 686, 786, and 826nm, respectively [92], and $r$ is the DOS source detector separation distance (2.5 cm for this experiment). Note that the measured AC amplitude attenuation and phase-shift were not employed in this analysis. DOS data were excluded for analysis if the intensity of light detected was outside the dynamic range of the instrument.

The DCS instrument is described in depth in Section 4.1. In brief, the device uses a long-coherence-length laser (> 5 meters, CrystaLaser, RCL-080-785S) operating at 785 nm to deliver coherent light to the tissue. Light is detected at the tissue surface with a bundle of 8 single mode detection fibers and is transmitted to a fast photon counting avalanche photodiode (APD). A custom built 8-channel correlator board (FLEX03OEM-8CH, correlator.com, Bridgewater, NJ) derives the intensity autocorrelation function based on the photon arrival times from the APDs.

For DCS analysis, we used the semi-infinite homogeneous medium solution to the correlation diffusion equation to fit our intensity autocorrelation curves, $g_2(\tau)$ for a

blood flow index (BFI), where BFI is related to the motion of the moving scatterers, namely red blood cells, and their concentration [61]. The fitting procedure assumes an initial value of $\mu_a$ and $\mu_s'$ (0.1 cm$^{-1}$ and 9 cm$^{-1}$, respectively, at 785 nm) for all patients [134]. Additionally, we fit the data assuming the mean squared displacement of the moving scatterers obeys a Brownian motion model, and thus the leading exponential decay rate of $g_2(\tau)$ should be proportional to the square root of the correlation time, $\tau$ [61, 68, 135]. The reduced scattering coefficient, $\mu_s'$, was assumed to remain constant, and the measured changes in $\mu_a$ at 786 nm computed with the DOS setup were incorporated into each fit of $g_2(\tau)$. DCS data were discarded if the intensity (i.e., photon count rate) of all detectors was less than 10 kHz (i.e., if the intensity signal-to-noise ratio was less than 10) or if $g_2(\tau)$ did not decay in a manner consistent with the Brownian motion model (note, this could be due to dynamics or breakdown of the semi-infinite homogeneous medium approximation, etc.), i.e., $\chi^2 > 0.001$, where

$$\chi^2 = \sum_{i=1}^{N} \frac{\left(g_2(\tau_i) - g_2(\tau_i)_{fit}\right)^2}{\sigma(\tau_i) g_2(\tau_i)_{fit}}. \quad [75]$$

Here $g_2(\tau_i)$ and $g_2(\tau_i)_{fit}$ are the measured and fit values of the intensity autocorrelation

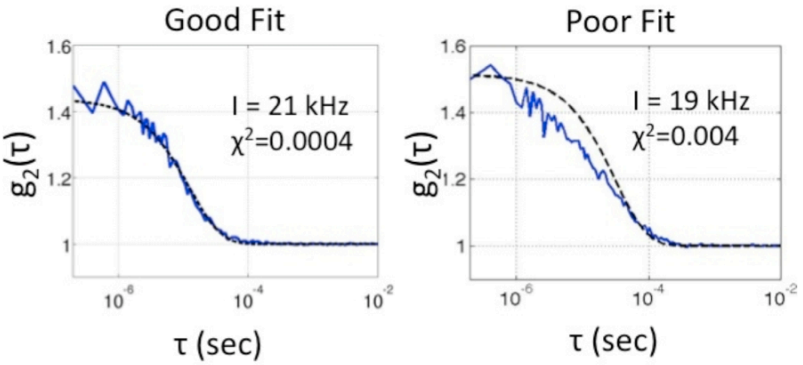


Figure 27, (Left) Sample intensity autocorrelation function, $\boldsymbol{g_2(\tau)}$, that fits well to the Brownian motion model; (Right) Sample poor $\boldsymbol{g_2(\tau)}$ fit to the Brownian motion model.

function at lag time $\tau_i$, respectively; $\sigma(\tau_i)$ is the noise of the measured correlation function at lag time $\tau_i$, computed using the formulation given in [111, 136]; and the sum is over the first N bins for which $g_2(\tau_i) > 1.05$. Examples of included and excluded $g_2(\tau)$ data along with their corresponding $\chi^2$ values are shown in Figure 27. A flow chart of DCS data inclusion/exclusion is seen in Figure 28.

For comparison with velocity mapping MRI data, a mean relative change in CBF obtained by DCS was calculated for each patient. A mean and standard deviation of the blood flow index, $\langle BFI \rangle$ and $\sigma_{BFI}$ respectively, were computed during the approximately 5 minute long room air and hypercapnia velocity mapping scans. We defined the change in CBF due to hypercapnia as $rCBF_{DCS} = (\langle BFI \rangle_{CO2} / \langle BFI \rangle_{Room\ Air}) \times 100\%$, where the subscript indicates data acquired during the hypercapnic or room air velocity mapping MRI scan. Additionally, cerebrovascular reactivity (CVR) was defined as $CVR = (rCBF_{DCS} - 100\%)/\Delta pCO_2$.

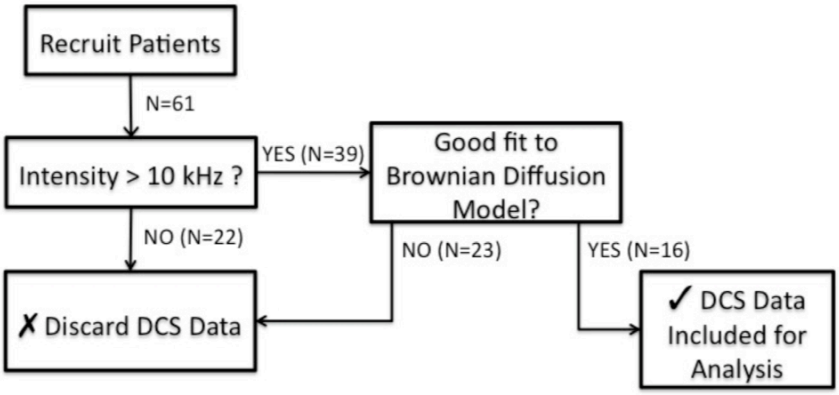


Figure 28, Flow Chart of decision criteria for including DCS data in analysis.

#### *5.1.1.3 Statistical Analysis*

To test the hypothesis that each of the relative variables differed from room air during

hypercapnia, we carried out a Wilcoxon signed rank test [137]. Analyses used R 2.11 [138]; hypotheses tests and associated p-values (*p*) were two-sided. Statistical significance was declared for p-values $< 0.05$.

To quantify the relationship between relative changes in blood flow in the jugular veins, superior vena cava, and aorta measured by velocity mapping MRI and relative changes in cerebral blood flow measured by DCS, we fit to a simple linear regression model and using this model estimated Pearson's correlation. Pearson's correlation, R, measures the extent to which a linear model explains variations in the data. Note that R could be very high, even for a case where the slope of the line between the two measures varied substantially from unity. We used Lin's concordance correlation coefficient (CCC) to measure agreement between the two measures. The CCC is, in fact, the product of Pearson's R, a measure of precision, and a bias correction factor which reflects the degree that the linear association between two variables differs from 45° through the origin, i.e., R = CCC/Bias Correction. Bland-Altman plots of the difference versus the mean of the two measures of relative flow changes were constructed as a graphical approach to assessing agreement [139].

### 5.1.2 Results

Sixty-two children with single ventricle congenital heart defects were recruited for the study. All patients were scheduled for staged surgical cardiac repair on the day of the study. Sixty-one patients completed the entire study; one was eliminated due to time constraints. Forty-five patients were also eliminated from analysis due to either low DCS light intensity or because the DCS optical data poorly fit the Brownian motion model and (see DCS methods). Sixteen of these 61 patients satisfied the inclusion criteria of

having high-quality DOS, DCS, and VENC MRI data (see Figure 28). Table 5 lists the median and interquartile range values of patient age, weight, height, head circumference, sex, and surgical procedure for the 16 patients included in this analysis as well as the 45 patients who were discarded from this analysis. The patients included for analysis had a median age of 0.5 years and were largely male (77 %). A Wilcoxon signed rank test revealed that patients included for this analysis were younger ($p = 0.004$), shorter ($p = 0.007$), and weighed significantly less ($p < 0.001$) than those who were discarded.

Figure 29 shows velocity mapping MRI and DOS/DCS data from a typical subject included in this analysis. The top images show the phase maps of the region in and around the right and left jugular veins during the room air (left) and hypercapnia (right). The veins are circled in white for ease of viewing. It is evident that during hypercapnia, the phase contrast in both vessels increases, indicating an increase in velocity in these vessels. The middle and bottom portions of Figure 29 show the continuous time trace of DOS measures of $\Delta\mathrm{Hb}$ and $\Delta\mathrm{HbO}_2$ (middle) and DCS measures of rCBF (bottom). The shaded grey regions indicate the time periods in which velocity mapping MRI scans were

| | Included Subjects: Median (IQR) | Discarded Subjects: Median (IQR) | p-value |
|---|---|---|---|
| Age (yrs) | 0.5 (0.4, 2.8) | 3.0 (2.3, 3.5) | 0.004 |
| Weight (kg) | 6.8 (5.6, 12.2) | 13.4 (11.6, 15.1) | < 0.001 |
| Height (cm) | 66.0 (63.1, 91.4) | 88.9 (83.8, 93.4) | 0.007 |
| Sex (Male:Female) | 13:3 | 26:19 | -- |
| Skull/Scalp/CSF Thickness (cm) | 0.79 (0.6, 0.9) | 0.79 (0.68, 0.96) | 0.44 |
| CSF Thickness (cm) | 0.26 (0.19, 0.5) | 0.23 (0.15, 0.3) | 0.18 |

Table 5, Patient demographics for the included (N = 16) and discarded (N = 43) subjects. Average skull, scalp and CSF thickness were computed underneath the optical probe using anatomical MRI images.

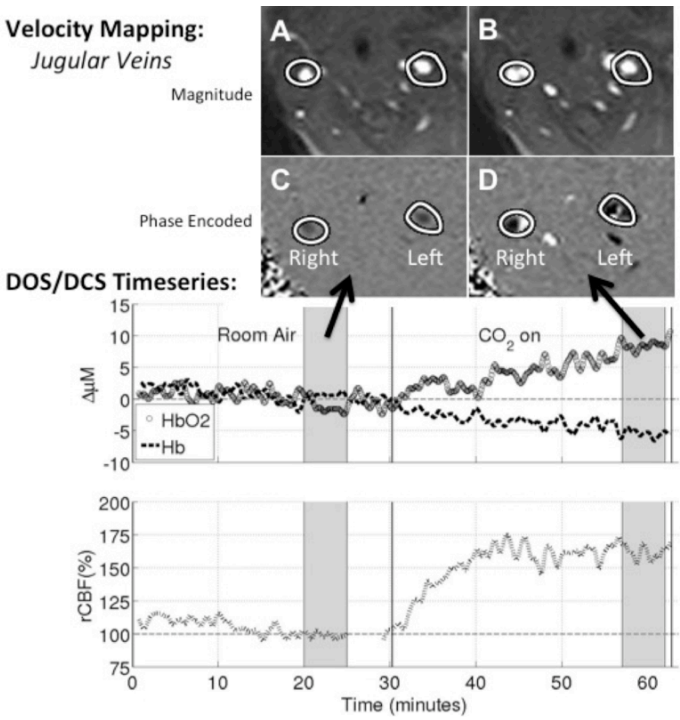


Figure 29, (Top) Phase encoded velocity mapping magnitude (A, B) and phase (C, D) images of the jugular veins taken during baseline (left) and hypercapnia (right). (Bottom) Sample time series of optical data. DOS measures of ΔHb and $\Delta HbO_2$ are shown on the top by dotted line and open circle, respectively, while DCS measures of rCBF are shown on the bottom. The grey shading indicates the time of the velocity mapping scans. Mean DCS data were acquired in these regions for comparison to VENC MRI results.

made. For comparison between DCS and velocity mapping MRI, the DCS data were averaged over the grey shaded regions to extract an average rCBF due to hypercapnia for each patient.

Table 6 summarizes the median and interquartile range of both the baseline (room air) and changes in all physiological parameters of interest. Since the DOS and DCS measures were all relative to the room air baseline, we just report changes. An asterisk (*) indicates a Wilcoxon signed rank test p-value of less than 0.05. Hypercapnia induced significant ($p < 0.01$) increases in CBF as measured by DCS and by phase-encoded velocity mapping MRI. Additionally, hypercapnia led to significant increases in

| Source | Variable | Baseline | Change due to $CO_2$ | p-value |
|---|---|---|---|---|
| Arterial Blood Gas | pH | 7.39 (0.02) | -0.18 (0.04) | < 0.001 |
| | $pCO_2$ | 38 (5) mmHg | 30 (13) mmHg | < 0.001 |
| EKG | Heart Rate | 103 (29) bpm | 8 (24) bpm | 0.021 |
| Cuff | Mean Arterial Pressure | 59 (16) mmHg | 2.5 (27) mmHg | 0.57 |
| Transcutaneous | $SpO_2$ | 78 (10) % | 1 (7) % | 0.68 |
| Velocity Mapping MRI | $BF_{Aorta}$ | 2.99 (1.21) L/min | 126.4 (23.1) % | < 0.001 |
| | $BF_{Jugular}$ | 0.59 (0.22) L/min | 151.5 (47.3) % | < 0.001 |
| | $BF_{SVC}$ | 0.84 (0.27) L/min | 146.0 (42.2) % | < 0.001 |
| | CVR-Aorta | -- | 0.8 (0.8) %/mmHg | < 0.001 |
| | CVR-Jug. | -- | 1.6 (2.9) %/mmHg | < 0.001 |
| | CVR-SVC | -- | 1.6 (2.5) %/mmHg | < 0.001 |
| DCS | CBF | -- | 141.0 (49.8) % | < 0.001 |
| | CVR | -- | 1.8 (2.7) %/mmHg | 0.001 |
| DOS | Hb | -- | 0.4 (4.8) μM | 0.85 |
| | $HbO_2$ | -- | 9.8 (5.4) μM | < 0.001 |
| | THC | -- | 10.2 (8.0) μM | < 0.001 |

Table 6, Median (interquartile range) baseline values followed by median (interquartile range) changes due to hypercapnia, and p-values obtained by Wilcoxon signed rank test.

heart rate, oxy- and total hemoglobin concentrations, and of course, $pCO_2$. Arterial pH decreased significantly with $CO_2$ administration, and no population-averaged changes were observed in deoxyhemoglobin concentration changes.

As seen in Figure 30 and summarized in Table 7, a comparison of phase encoded velocity mapping MRI measures of relative changes in cardiac output in the superior vena cava to DCS measures of changes in cerebral blood flow were linearly related with high Pearson and concordance correlation coefficients (R = 0.89, CCC = 0.89) and a slope (95% CI) of 0.92 (0.65, 1.19). A similar correlation to DCS flow changes was observed with MRI measures of relative changes in cardiac output in the jugular vein, R = 0.92, CCC = 0.91, slope (95% CI) = 0.83 (0.63, 1.03). Weaker

| Site | CCC | Bias Correction | Slope Estimate (95% CI) | Intercept Estimate (95% CI) [%] | $R^2$, p-value |
|---|---|---|---|---|---|
| Jugular Veins | 0.91 | 0.99 | 0.83 (0.63, 1.03) | 21.1 (-10.0, 52.2) | 0.84, $p < 0.001$ |
| Superior Vena Cava | 0.89 | 0.99 | 0.92 (0.65, 1.19) | 14.2 (-27.7, 55.1) | 0.79, $p < 0.001$ |
| Aorta | 0.25 | 0.50 | 1.26 (0.03, 2.50) | -9.2 (-163.0, 144.6) | 0.20, $p = 0.045$ |

Table 7, Summary of concordance correlation coefficients ($\rho_c$) and bias correction factor, along with the estimated slope and intercept for a linear regression between DCS measures of rCBF and Phase Encoded Velocity Mapping rBF and the adjusted $R^2$ and p-values.

correlations were also observed between rBF in the aorta and rCBF from DCS with a slope (95% CI) of 1.26 (0.03, 2.50) ($p = 0.045$).

### 5.1.3 Discussion

We observed significant agreement between changes in CBF measured with diffuse correlation spectroscopy and changes in blood flow in the jugular veins and superior vena cava measured with VENC MRI. Although the two techniques measure entirely different vascular structures related to cerebral hemodynamics, this strong agreement is encouraging. DCS measures cerebral blood flow in the microvasculature. The optical probe was secured to the forehead; thus, in this study we were monitoring changes in CBF at the surface of the frontal cortex. VENC MRI measures blood flow in the jugular veins and superior vena cava, both of which are capacitance vessels that accommodate the large volume of blood flowing through them. Hypercapnia induces significant global changes in cerebral blood flow in the grey and white matter [140, 141]. Therefore, in normal function, the *micro*vascular CBF changes in the frontal cortex measured by DCS should represent similar changes throughout the brain, and these *micro*vascular changes should also be reflected in the *macro*vascular changes in blood

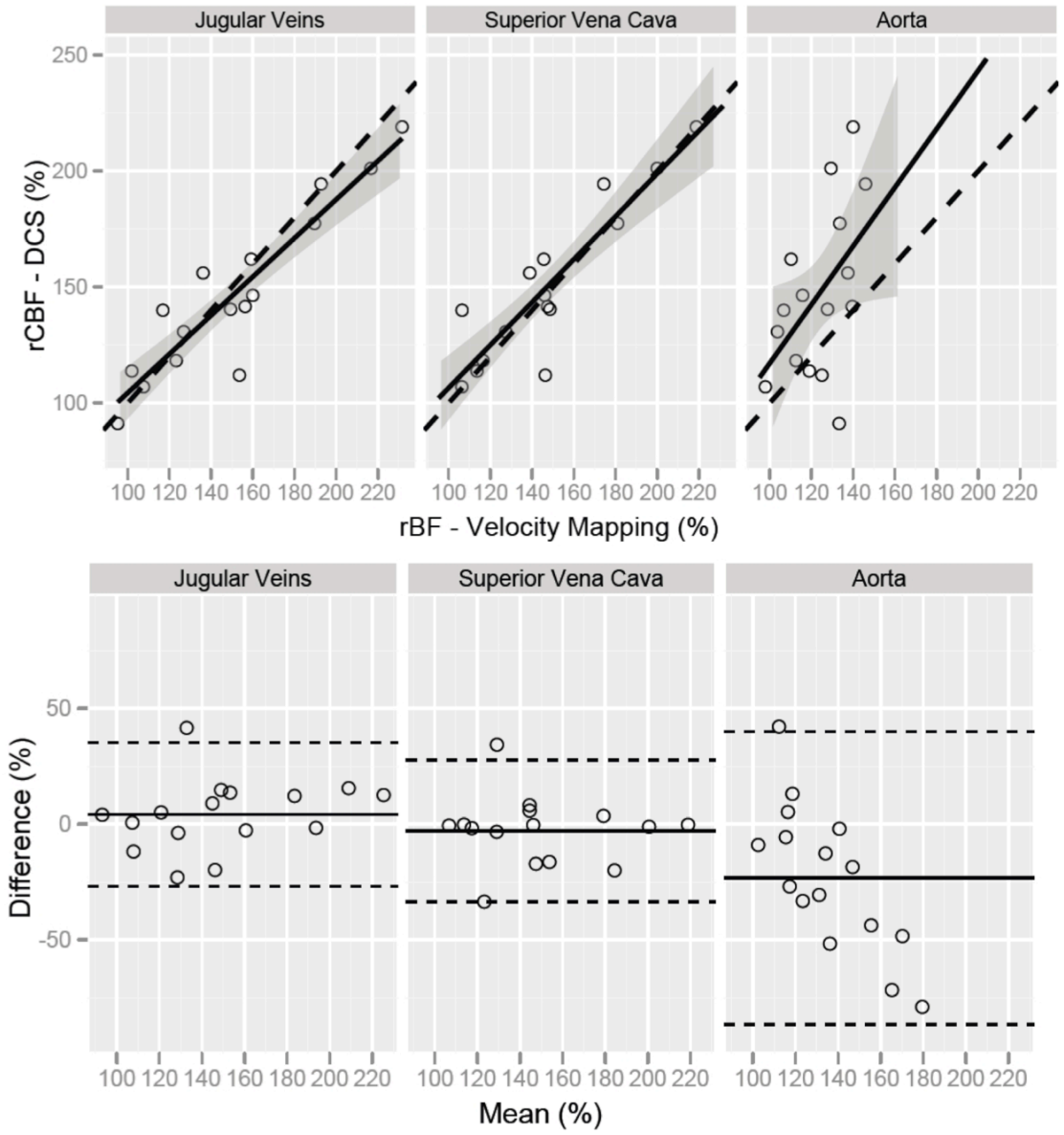


Figure 30, (TOP) Changes in blood flow measured with velocity mapping MRI in the Jugular Veins (left), Superior Vena Cava (middle), and Aorta (right) compared to $rCBF_{DCS}$. The solid line represents the best-fit line to the data, while the dotted line indicates the line of perfect concordance. The grey ribbon denotes the 95% confidence interval for the mean $rCBF_{DCS}$. (BOTTOM) Bland-Altman plots of the difference in rBF, measured with VENC-MRI, and rCBF, measured with DCS, versus the mean of these parameters. Solid horizontal lines indicate the mean difference between each VENC parameter and rCBF measured with DCS, while the dotted lines indicate the 95% limits of agreement.

flow drainage in the jugular veins [128, 129]. Naturally, this micro/macro agreement presumes the patient has a healthy brain with no regions of watershed or hypoxia that

may cause the frontal cortex to be a poor representation of the whole brain. Further, all patients were studied under conditions of general anesthesia with mechanical ventilation and neuromuscular blockade, conditions which are similar to the conditions present in the immediate post-operative recovery period. These conditions preclude regional activation of cerebral cortex due to cognitive processes or movement.

This agreement between VENC MRI and DCS is encouraging, as one of the major advantages of DCS is its portability. Thus, as opposed to the sporadic CBF measures that phase encoded velocity mapping MRI provides, these results suggest DCS may be employed to accurately assess relative changes in CBF in a continuous fashion at the patient's bedside. DCS may be a particularly attractive option for critically ill patients who are difficult to transport safely to an MRI, who are unable to have an MRI due to metallic implants, or who would benefit from continuous CBF monitoring.

As per the poor correlation between DCS and aortic flow, a priori we would not expect changes in aortic flow due to hypercapnia to accurately represent microvascular CBF changes seen with DCS. Aortic blood flow represents systemic blood flow, i.e., flow to both the brain and the body. Since CBF represents only one portion of the total cardiac output, we should expect the fractional change in CBF from the aorta during hypercapnia to be dependent on cerebrovascular reactivity, as well as the geometry of the aortic arch and its branches. Total flow changes to both body and brain should match total aortic flow changes; however, the individual components (brain and body flows) alone will not necessarily tract aortic flow changes as not all tissues respond to $CO_2$ in a uniform way.

A handful of publications have studied the cerebral hemodynamic effects of

hypercapnia on patients with congenital heart defects [59, 142-145]. Durduran *et al* [59] measured a mean (standard deviation) cerebrovascular reactivity to increased $CO_2$ of 3.1 (1.9) %/mmHg in neonates with congenital heart defects using DCS. The population studied in this work was considerably older than the neonates previously studied, ranging in age from 3 months to 5 years old. In this population we found a slightly lower mean (standard deviation) $CO_2$ reactivity of 1.8 (2.7) %/mmHg. Fogel *et al* [145] studied older CHD patients with VENC-MRI during hypercapnia, mean (standard deviation) age of 2.2(0.5) years. They found a mean increase in jugular flows of 230 % with a mean change in $pCO_2$ of 23 mmHg, indicating a cerebrovascular reactivity of approximately 5%/mmHg. Our results thus fall within the published values for this patient population of infants with congenital heart defects.

***Optical Data Quality***

While 61 patients who underwent optical monitoring during hypercapnia, only 16 had data that stood up to the stringent requirements we placed on data quality. The main reasons for exclusion from the study were either low intensities of detected light by DOS/DCS (N = 22) and/or poor fits of the DCS data to the semi-infinite homogeneous medium correlation diffusion equation solution (N = 23). The problem with low intensities was typically due to limited time for probe placement. The problem with poor quality fits is currently not as well understood. For example, we have used this particular DCS instrumentation and optical probe on numerous other studies [65, 146], and these data have yielded intensity correlations that fit nicely to the effective Brownian diffusion model. Therefore, we believe the unusual correlation curves in these patients are caused by the anatomy and/or optical properties of the brain in this unique population.

One possible structural source of error along these lines would arise from patients with excessive amounts of cerebrospinal fluid and/or thicker skulls; our population falls into this group, having a median (IQR) skull thickness of 0.79 (0.30) and csf thickness of 0.26 (0.31) cm. We are currently working on Monte Carlo modeling of light propagation using anatomical images segmented by brain, cerebrospinal fluid, and skull/scalp as the input geometry. Additionally, we are performing bench-top experiments with phantoms to attempt to replicate these slow decaying correlation curves and to understand their origin. However, because this paper aims to further validate DCS against VENC MRI, we only included the data that fit well to the theory of effective Brownian motion and that are representative of the experimental DCS correlation curves we observe in most of the other populations we have studied [59-61, 63, 65].

Correlations between rCBF measured with DCS and rBF measured with VENC MRI for all patients, regardless of the quality of the DCS data fits (N = 39) were computed and the results can be found in Appendix 5.1.5. Including data from patients with poor intensity autocorrelation function fits significantly reduces (although does not negate) the agreement and correlation between DCS and VENC MRI.

***Optical Approximations***

Due to limitations in probe size, we were restricted to a single source-detector separation for DOS measurements. Thus, the modified Beer-Lambert law was used to quantify changes in the absorption coefficient and thus changes in oxy- and deoxy-hemoglobin. However, many assumptions are required to employ the modified Beer-Lambert Law. In particular, it is assumed that $\Delta\mu_a$ is small relative to its baseline value, and we assume that $\mu_s'$ remains constant. These assumptions appear to be valid in the

present experiment. On average, $\Delta\mu_a$ at 786 nm was 0.015 $cm^{-1}$, a change of approximately 15% of the presumed baseline value of $\Delta\mu_a$ = 0.1 $cm^{-1}$ at 786 nm. Similar results were found for 688 and 826 nm. Additionally, although $\mu_s'$ was not explicitly measured in this experiment, we feel justified in assuming $\mu_s'$ does not change due to hypercapnia [147]. Red blood cells contribute very little to the total cell volume of brain tissue, thus the majority of light scattering events are most likely due to mitochondria and other organelles as well as cell nuclei [96, 97]. Even if the blood volume increases substantially due to hypercapnia, this increase would have a small effect on the net scattering coefficient.

To fit the DCS data for a blood flow index, we assumed initial values for the absorption and reduced scattering coefficients ($\mu_a$ and $\mu_s'$). Because we are only interested in relative changes in the BFI, our choice of initial $\mu_a$ and $\mu_s'$ has little to no effect on the resulting value of rCBF. However, changes from these initial values of $\mu_a$ and $\mu_s'$ that occur during the duration of the study may influence the magnitude of rCBF. Thus, we incorporated changes in $\mu_a$ obtained with DOS into our fitting procedure for BFI. However, as mentioned previously, our DOS analysis assumed that the scattering coefficient remained constant during the duration of the study. This assumption is most likely valid for hypercapnia. However, if false, a 10% increase in the scattering coefficient could alter the magnitude of rCBF by approximately 20%. Thus, future work would benefit greatly from the use of multiple source detector DOS amplitude and phase measurements used to continuously quantify $\mu_a$ and $\mu_s'$.

We have anatomical brain images of each patient, and we computed the mean (standard deviation) skull/scalp/CSF thickness underneath our optical probe to be 0.81

(0.31) cm. Because of the 2.5 cm source-detector separations used for both DOS and DCS, photons travel on average a depth of 1 to 1.25 cm into the tissue. Thus, we are confident the optical measurements are probing the surface of the cortex. However, in the future, DCS quantification of rCBF can be further improved. A semi-infinite model was used to fit DCS data. As known from the anatomical scans, this model greatly simplifies the head geometry of these patients. In reality, the scalp, skull, cerebral spinal fluid, grey matter, and white matter possess different optical properties that can be accounted for, at least partially, in Monte Carlo simulations of light propagation [148-150]. Although the semi-infinite model can be improved upon, it provides a sufficient approximation for this pilot study.

***MRI Assumptions***

VENC MRI is a very accurate technique that does not depend on assumptions of flow profiles. Nevertheless, eddy currents and higher order Maxwell terms can introduce errors into the measurements. In addition, if a blood vessel is tortuous, flow may not be perpendicular to the imaging plane and this may introduce errors as well. Finally, partial volume effects will “average out” velocities in a given voxel, decreasing the accuracy of the measurement. In our study, eddy currents and Maxwell terms were minimized and the authors took great pains to ensure the imaging plane was perpendicular to flow. The dimensions of our VENC MRI images were 1 x 1 x 5 mm, well within accepted norms. Prior to each MRI scan, phantoms were used to calibrate the system.

### 5.1.4 Conclusions

We have demonstrated a highly significant correlation between measures of relative

changes in cerebral blood flow measured with diffuse correlation spectroscopy and relative changes in blood flow in the jugular veins and superior vena cava in pediatric patients with congenital heart defects. This agreement further strengthens the promise of DCS as an accurate and non-invasive modality for continuous CBF monitoring at the bedside.

### 5.1.5 APPENDIX: Results with All Patients Included

For comparison to the results presented herein, I have also computed the correlations between rCBF measured with DCS and rBF measured with VENC MRI for all patients, regardless of the $\chi^2$-value of the fit to the DCS intensity autocorrelation function. Thirty-nine patients had DCS intensities greater than 10 kHz and were thus included in this analysis.

| Site | CCC | Bias Correction | Slope Estimate (95% CI) | Intercept Estimate (95% CI) [%] | $R^2$, p-value |
|---|---|---|---|---|---|
| Jugular Veins | 0.68 | 0.94 | 0.52 (0.33, 0.72) | 78.3 (47.6, 109.1) | 0.29, $p < 0.001$ |
| Superior Vena Cava | 0.56 | 0.91 | 0.59 (0.30, 0.87) | 75.3 (32.9, 117.8) | 0.36, $p < 0.001$ |
| Aorta | 0.22 | 0.41 | 1.26 (0.51, 2.01) | -0.2 (-95.1, 94.7) | 0.26, $p = 0.002$ |

Table 8, Summary of concordance correlation coefficients ($\boldsymbol{\rho_c}$) and bias correction factor, along with the estimated slope and intercept for a linear regression between DCS measures of rCBF and Phase Encoded Velocity Mapping rBF and the adjusted $R^2$ and p-values for the N = 39 patients with intensity of DCS data > 10 kHz (regardless of the quality of the DCS data fit).

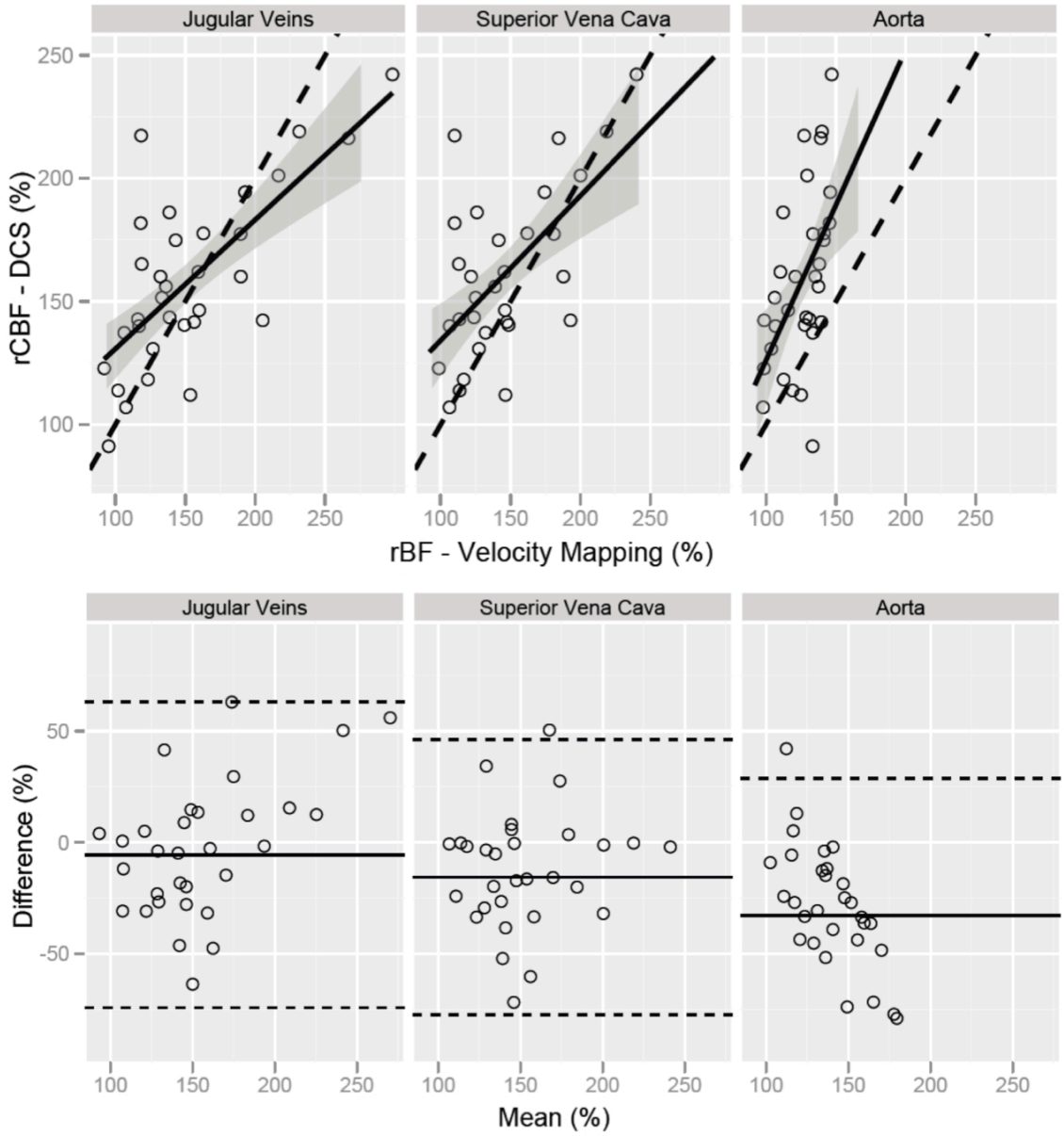


Figure 31, (TOP) Changes in blood flow measured with velocity mapping MRI in the Jugular Veins (left), Superior Vena Cava (middle), and Aorta (right) compared to $rCBF_{DCS}$ for the N = 39 patients with intensity of DCS data > 10 kHz (regardless of the quality of the DCS data fit). The solid line represents the best-fit line to the data, while the dotted line indicates the line of perfect concordance. The grey ribbon denotes the 95% confidence interval for the mean $rCBF_{DCS}$. (BOTTOM) Bland-Altman plots of the difference in rBF, measured with VENC-MRI, and rCBF, measured with DCS, versus the mean of these parameters. Solid horizontal lines indicate the mean difference between each VENC parameter and rCBF measured with DCS, while the dotted lines indicate the 95% limits of agreement.

Figure 31 and Table 8 summarize the comparison of phase encoded velocity

mapping MRI measures of relative changes in cardiac output in the superior vena cava, jugular veins, and aorta to DCS measures of changes in cerebral blood flow. As evident from these plots, including data from patients with poor intensity autocorrelation function fits significantly reduces (although does not negate) the agreement and correlation between DCS and VENC MRI.

## 5.2 BFI correlations with Doppler ultrasound velocities

Between 1990 and 2005 the percentage of preterm births in the United States rose by 20% [1]. Preterm births now account for almost half of children with cerebral palsy, as well as a significant portion of children with cognitive, visual, and hearing impairments [151]. Three forms of acquired brain injury affect the likelihood of mortality and neurodevelopmental deficits in very low birth weight (< 1500 g), very preterm (< 32 weeks gestation age) neonates: hypoxic ischemic insult, periventricular leukomalacia (PVL) and intraventricular hemorrhage (IVH) [2, 3]. PVL is a specific form of necrosis of the cerebral white matter adjacent to the lateral ventricles that is often associated with impaired motor development and is a major cause of cerebral palsy. During the early stages of brain development, this region of white matter is highly susceptible to injury from lack of blood flow and oxygen delivery due to the maturation stage of the supporting cells (oligodendrocytes) [4]. IVH refers to hemorrhaging from the germinal matrix, an immature bed of vascular tissue along the ventricular wall that is typically present only in preterm infants less than 32 weeks gestation age. Such hemorrhages are caused by fluctuations in cerebral blood flow (CBF) and may induce profound cognitive and physical handicaps. A continuous monitor of CBF at the bedside could therefore be a valuable supplement for gathering information about a patient's condition [5] and for

guiding treatment. *Microvascular* information about cerebral perfusion, in particular, is attractive because the microvasculature controls oxygen and nutrient delivery to relevant tissues.

Currently, transcranial Doppler ultrasound (TCD) and near-infrared spectroscopy (NIRS) are the only techniques deemed feasible for the estimation of CBF in this clinical population. TCD measures cerebral blood flow velocity (CBFV) in the cerebral arteries by monitoring the frequency shift of acoustic waves that scatter from moving red blood cells [31, 152]. With additional information about the cross-sectional area of the insonated vessel, CBFV permits calculations of arterial CBF. However, cerebral vessels are small in size, making their diameter difficult to measure [36]. To avoid this source of error, one could focus on relative changes in flow. However, these blood vessels can change caliber over time, leading to large errors in calculations of relative change, which in turn cause errors in estimates or

Near-infrared spectroscopy measures tissue oxy- and deoxy-hemoglobin concentrations, taking advantage of the tissue absorption “window” in the near-infrared [153]. A comprehensive review of near-infrared spectroscopy in the neonate was recently published by Wolfberg and du Plessis [154]. Although NIRS measurements of tissue oxygenation and total hemoglobin concentration are increasingly more common in the clinic, the calculation of CBF from NIRS data is indirect and relies on the Fick principle, which states that the total uptake of a tracer by tissue is proportional to the difference between the rates of inflow and outflow of the tracer to and from the tissue [155]. This calculation requires the use of a tracer, typically oxygen or indocyanine green, and requires certain assumptions to be valid, namely that cerebral blood volume, CBF,

and cerebral oxygen extraction must remain constant.

In this chapter we employ another recently developed optical technique to measure CBF: diffuse correlation spectroscopy (DCS). DCS [102, 104, 105, 115, 135] has shown promise as a monitor of relative changes in blood flow (see Table 2). Like NIRS, DCS also employs near-infrared light to probe the dynamics of deep tissues. However, DCS detects changes in CBF *directly* by monitoring temporal fluctuations of scattered light. It does not rely on tracers to indirectly infer information about CBF, and it can be employed continuously. Finally, in contrast to TCD, DCS provides information about *microvascular* hemodynamics.

In the present investigation, diffuse correlation spectroscopy and transcranial Doppler ultrasound monitor the hemodynamics of four very low birth weight, very preterm neonates during a 0º to 12º postural change. Because this study is a feasibility test, we limited head of bed elevation to values within the range of the clinical isolette beds. Many studies have been conducted to determine the physiological response of preterm infants to postural manipulations [37, 156-164]. Most of this work has focused on changes in vitals signs, such as heart rate, blood pressure, and/or arterial oxygen saturation, although some groups have also used near-infrared spectroscopy to probe cerebrovascular oxygenation during postural change [161-163]. To this author's knowledge, only one study by Anthony *et al.* has been done with Doppler ultrasound to monitor the effects of HOB elevation to cerebral blood flow velocity in the main arteries [37], and no experiment has examined the resulting changes in microvascular cerebral blood flow. Anthony et al. defined four classifications of peak systolic velocity response within 30 seconds of a 20º HOB elevation: (1) a sudden change within 5 seconds, (2) a

sudden change within 5 seconds, followed by a corrective change, (3) no change, (4) cycling or no discernible trace. Responses 2 and 3 were the most common. Two major questions raised by this finding are: what relationships exist between these large-vessel changes and the microvascular cerebral blood flow, and what impact, if any, does postural manipulation have on this microvascular flow. Our present study aims to address both of these questions by examining the use of diffuse correlation spectroscopy on preterm neonates.

Our results indicate that on a measurement by measurement basis, significant correlations were found between absolute values of the blood flow index (BFI) measured by DCS and peak systolic velocity (PSV) and mean velocity (MV) measured by TCD; a weaker, but still significant, correlation was found between BFI and end diastolic velocity (EDV) measured by TCD. As per the entire patient population, both modalities found no significant relative changes in hemodynamics during this relatively small (12°) postural intervention. Thus we demonstrate the use of DCS on this population of preterm infants, we show agreement between DCS and TCD for the first time, and we suggest that such small postural changes do not significantly affect cerebral blood flow in this population.

### 5.2.1 Methods and materials

The DCS instrument uses a long-coherence-length laser (CrystaLaser, RCL-080-785S) operating at 785 nm to deliver light to the tissue. A single mode fiber secured by a black foam pad detects light 1.5 cm from the source. The fiber is custom designed with a 90° bend on the patient end, permitting the probe to rest adjacent to the forehead. Light is detected by a fast photon counting avalanche photodiode that outputs a TTL signal for every photon received. This TTL signal is transmitted to a custom built 2-channel

correlator board (FLEX03OEM-2CH, correlator.com, Bridgewater, NJ) which derives the intensity autocorrelation function based on the photon arrival times [165]. Figure 32 shows a sketch of the probe on the infant's head.

Protocols for both DCS and TCD measurements are shown in Figure 33. Head-of-bed (HOB) angle manipulations were limited by the range of the isolette beds (Ohio Care, Ohmeda Isolette). These beds easily adjust from an angle of 0º to approximately 12º in seconds.

For DCS, data were acquired for 30 minutes: three 5 minute HOB = 0º sessions, alternating with three 5 minute HOB = 12º sessions. Intensity autocorrelation curves were averaged over a period of 3 seconds and were acquired every 7 seconds, resulting in around 300 BFI data points per study. These curves were then converted to electric field autocorrelation functions using the Siegert relation with a fitted value for $\beta$ of approximately 0.5. Theoretically, we expect β to be approximately equal to the inverse of the number of modes allowed to pass through the detection optics. In our case of single mode detection fibers, the number of modes is two. For analysis, we solved the

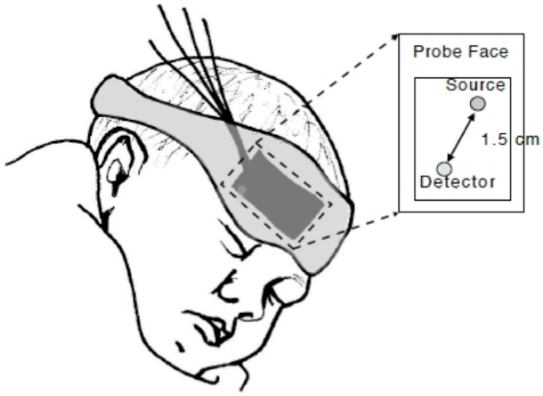


Figure 32, The fibers used to deliver and detect light are secured to the infant's forehead using a soft black pad. The pad is held in place with a mask that wraps around the head.

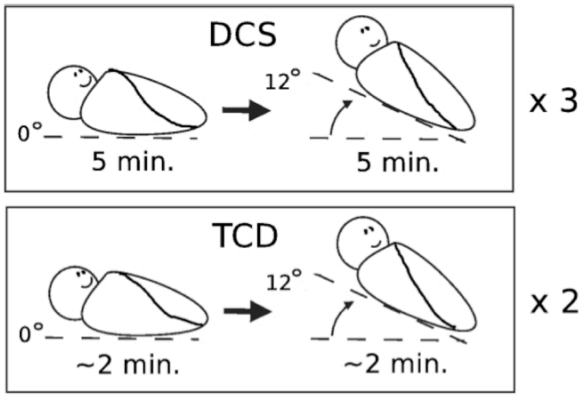


Figure 33, Diagram of the protocol used for DCS (top) and TCD (bottom) measurements. DCS and TCD measurements were NOT taken at the same time. For DCS, data was taken continuously (8 data points per minute) for 5 minutes at each head of bed angle adjustment. The head of bed 0° to 12° elevation was repeated 3 times, making the total study time 35 minutes. By comparison, for TCD only 3 data points were taken at each HOB angle before the bed was repositioned, and the HOB angle was only elevated twice.

correlation diffusion equation analytically, assuming the sample geometry was a homogeneous, semi-infinite medium. We used the semi-infinite solution (Equation 1) to fit our data for BFI. This fit is made possible by assuming constant values for $\mu_a$ and $\mu_s'$ (0.1 $cm^{-1}$ and 10 $cm^{-1}$, respectively, at 785 nm) for the whole population and throughout the study. These values were chosen from literature references [166, 167].

A mean relative change in CBF was calculated after each HOB = 12º event using the preceding HOB = 0º event for a baseline, i.e., for the $i^{th}$ repetition, $rCBF_i = BFI_i(12°)/BFI_i(0°) \times 100\%$, where $BFI_i(\theta)$ indicates the mean BFI over all data points taken at the $i^{th}$ HOB = $\theta$ event. After $rCBF_i$ was calculated for each HOB change (3 total per day of study), a mean relative change in cerebral blood flow, $\langle rCBF \rangle$, was determined for each day. Here <> denotes the mean value over all $rCBF_i$ measured on a given day. Additionally, to compare absolute measurements of BFI to the velocities found from TCD, a mean blood flow index, $BFI$, was calculated for each day of study. For the purposes of this analysis, we used the initial HOB=0º data to calculate BFI, i.e., $BFI = BFI_{i=1}(0°)$, since the baby was most peaceful during this time period.

The protocol for TCD measurements differed slightly from the DCS protocol. Only two or three measurements of peak systolic velocity (PSV), end diastolic velocity (EDV), and mean velocity (MV = (PSV −EDV)/PI, where PI is the pulsatility index measured by the ultrasound scanner), were obtained at each head of bed angle. A Philips ATL HDI 5000 ultrasound scanner (Philips Medical Systems, Bothell, WA) with a C8-5 MHz broadband curved array transducer was used for data acquisition. Typically this process was repeated twice. As in the case of the mean rCBF calculation, mean relative changes of each parameter for the i$^{th}$ repetition ($rPSV_i$, $rEDV_i$, $rMV_i$) comparing the responses at elevated HOB to lying flat were computed after each HOB change, i.e., $rPSV_i = PSV_i(12°)/PSV_i(0°) \times 100\%$. Daily mean changes in velocities, $\langle rPSV \rangle$, $\langle rEDV \rangle$, $\langle rMV \rangle$, were calculated in the same manner as $\langle rCBF \rangle$. For comparison to DCS, mean velocities at the initial HOB = 0º event ($PSV = PSV_{i=1}(0°)$, $EDV = EDV_{i=1}(0°)$, and $MV = MV_{i=1}(0°)$) were calculated for each day of study. Unfortunately TCD and DCS data could *not* be collected at the same time due to the size of the infant's head. However, the data were acquired on the same day by both modalities.

For the purpose of this analysis, we considered each of the nine days of data acquisition to be independent observations. To test for an association between $BFI$ and each of $PSV$, $EDV$, and $MV$, as well as between $\langle rCBF \rangle$ and each of $\langle rPSV \rangle$, $\langle rEDV \rangle$, and $\langle rMV \rangle$, we used Spearman's rank-based non-parametric approach [168]. Rejection of the null hypothesis in this case implies a positive or negative, and possibly non-linear, association between the variables. Pearson's correlation coefficient was used to estimate a linear association between $BFI$, and each of $PSV$, $EDV$, and $MV$. To test the hypothesis that each of the four relative variables differed from baseline during HOB elevation, we conducted a Wilcoxon signed rank test [137]. Analyses were carried out

using R 2.8 [138]; hypotheses tests and associated p-values (*p*) were two-sided. A family-wise error rate of 0.05 was maintained using Hochberg's method [169] to adjust for multiple comparisons within each of the three sets of analyses (associations with $BFI$, associations with $\langle rCBF \rangle$, and comparison with baseline); adjusted p-values, $p_A$, are also reported.

### 5.2.2 Results

In total, we acquired nine days of data sets on four preterm infants with both DCS and TCD. The mean gestation age of our population was 26.3 weeks (range = 25-27 weeks) and the mean birth weight was 896 g (range = 640-1150 g). At the time of the study, the mean weight was 1185 g (range = 650-1900 g), and the mean corrected gestational age, defined as gestational age plus the time since birth, was 29.2 weeks (range = 26-34 weeks).

#### *5.2.2.1 Results-DCS*

Diffuse light signals (~100,000-500,000 photons/sec) were sufficient for all patients. Autocorrelation curves were averaged over a period of 3 s, leading to fairly smooth data and good signal-to-noise ratio. Sample autocorrelation curves are shown in Figure 34. The solid black line is the raw data. The dotted black line shows the fit to the data. The median (range) $BFI$ for all nine days of measurement at the initial HOB = 0º position was $1.62\times10^{-8}$ ($0.98-3.31\times10^{-8}$) $cm^2/s$. Median $\langle rCBF \rangle$ over the nine days of measurements was 93.4 (87.3 to 112.8) % (see Table 9).

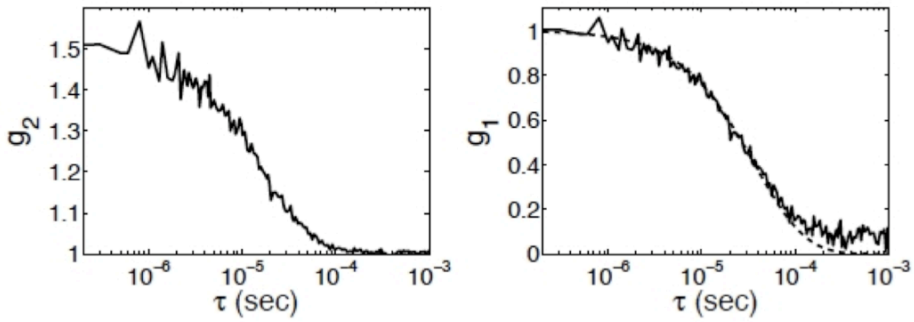


Figure 34, (Left) Typical normalized intensity autocorrelation curve derived directly from the correlator board as a function of time, $\tau$ (data measured on the forehead of a preterm infant). (Right) The corresponding normalized electric field autocorrelation curve, $g_1(\mathbf{r},\tau)$, calculated using the Siegert relation with a fitted value for $\beta$. The solid line shows the raw data. The dotted line is the best-fit curve to a Brownian motion model, which we use to derive the blood flow index (BFI).

#### *5.2.2.2 Results-TCD*

The TCD data at the initial HOB=0◦ event revealed a median (range) $PSV$ of 44.1 (20.9 to 70.3) cm/s; median $EDV$ was 8.3 (5.1 to 12.8) cm/s; median $MV$ was 21.3 (11.4 to 30.6) cm/s. Median relative changes in these parameters ($\langle rPSV \rangle$, $\langle rEDV \rangle$, and $\langle rMV \rangle$) after the postural intervention are shown in Table 9. A Wilcoxon signed rank test on these relative parameters revealed no significant changes from baseline values during HOB elevation.

#### *5.2.2.3 Comparison of DCS and TCD*

Figure 35 (left) shows the relationship between baseline *PSV* and *BFI* for TCD and DCS. The error bars in the horizontal and vertical directions represent the standard deviation in the mean value of the given parameter over all data points recorded at the first HOB=0º event. The estimated Spearman rank correlation coefficient, $r_s$, was 0.76, indicating a significant positive correlation ($p$ = 0.018, $p_A$ = .036) between $PSV$ and $BFI$. Baseline $MV$ and $BFI$ (Figure 35, center) revealed a significant correlation as well with $r_s$

| | Median (%) | Range (%) | p-value |
|---|---|---|---|
| $\langle rCBF \rangle$ | 93.4 | 87.3 to 112.8 | 0.12* |
| $\langle rPSV \rangle$ | 103.0 | 91.1 to 128 | 0.34** |
| $\langle rEDV \rangle$ | 104.0 | 61 to 138 | 0.91** |
| $\langle rMV \rangle$ | 100.1 | 80 to 125 | 0.53** |

Table 9, Median and range of average daily hemodynamic response to postural elevation

= 0.78 ($p$ = 0.013, $p_A$ = .036). As seen in Figure 35 (right), the relationship between $BFI$ and $EDV$ also achieved significance ($r_s$ = 0.67, $p$ = 0.047, $p_A$ = .047). The solid grey lines in Figure 35 depict the best linear fit to the data. Pearson's correlation coefficient, $R^2$, was calculated, and modest positive linear correlations between $PSV$ and $BFI$, $MV$ and $BFI$, and $EDV$ and $BFI$ were detected ($R^2$ =0.58, 0.44, 0.13).

Both techniques showed no significant hemodynamic population-averaged changes during HOB elevation as compared to HOB flat (Table 9). In addition, correlations between $\langle rCBF \rangle$ and relative ultrasound parameters did not reach statistical

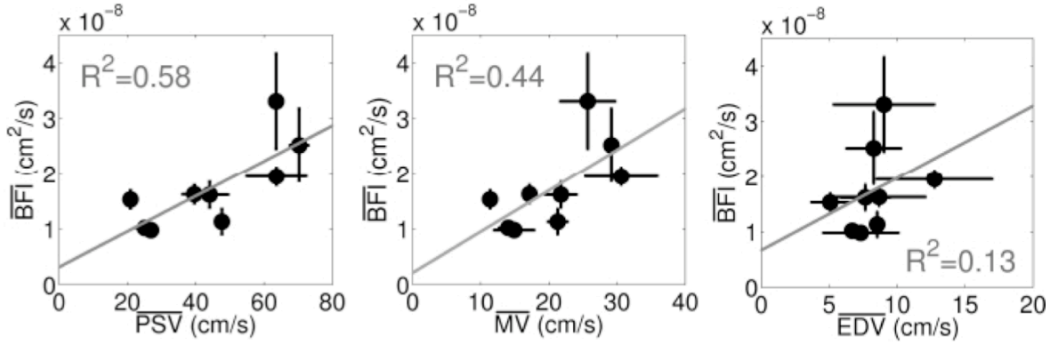


Figure 35, (Left) Correlation between population averaged mean TCD PSV taken at the initial HOB=0º (*PSV*) and population averaged mean DCS BFI also taken at the initial HOB=0º (*BFI*). (Center) Correlation between population averaged mean TCD MV taken at the initial HOB=0º (*MV*) and DCS *BFI*. (Right) Correlation between population averaged mean TCD EDV taken at first HOB=0º event (*EDV*) and DCS *BFI*. The solid line in each plot shows the best linear fit between the two variables. Both Pearson's and Spearman's correlation coefficients ($R^2$ and $r_s$, respectively) were calculated. The $R^2$ Pearson values are displayed for each plot.

significance for the HOB perturbation (i.e., $\langle rCBF \rangle$ and $\langle rPSV \rangle$, $r_s$ = 0.52, $p$ = 0.15, $p_A$ = 0.19; $\langle rCBF \rangle$ and $\langle rEDV \rangle$, $r_s$ = 0.55, $p$ = 0.12, $p_A$ = 0.19; $\langle rCBF \rangle$ and $\langle rMV \rangle$, $r_s$ = 0.49, $p$ = 0.19, $p_A$ = 0.19).

### 5.2.3 Discussion

The study was conducted to demonstrate the feasibility of diffuse correlation spectroscopy (DCS) for continuous monitoring of cerebral blood flow (CBF) in preterm infants and to compare measurements of DCS with transcranial Doppler ultrasound (TCD); the latter technique is used routinely for this population. A priori, the two modalities need not be strongly correlated since they measure different quantities: TCD measures flow in primary arteries, and DCS measures flow in tissue microvasculature. Our results show that a correlation exists between TCD measurements of peak systolic and mean velocities in the middle cerebral artery and DCS measurements of blood flow index, and that this correlation is statistically significant in this population. Furthermore, a weak but significant correlation exists between BFI and end diastolic velocity. The relative weakness of this correlation is due primarily to the low signal-to-noise ratio (SNR) of the EDV measurements for this population. Intuitively, one might expect BFI to correlate most strongly with MV, given that BFI is extracted from an autocorrelation curve which is averaged over three seconds (approximately 7 cardiac cycles). However, since MV is derived from EDV, it is strongly influenced by the low SNR of the EDV data.

While absolute values of BFI from DCS and velocities from TCD correlate significantly, correlations between relative changes in these parameters did not achieve significance. It is not entirely clear why the absolute velocity measurements correlate well with BFI, while relative changes do not correlate with rCBF. We hypothesize that

there may have been insufficient statistical power given the limited sample size and relatively large physiological and measurement noise as well as inter- and intra-subject variability. Future experiments would benefit from concurrent TCD and DCS data acquisition. Our TCD results of relative velocity changes concur with Anthony et al. [37], who showed that most infants showed little or no middle cerebral artery velocity response to postural changes. However, a direct comparison between the studies is difficult because Anthony et al. used a larger bed elevation (20°) and monitored continuously before and after the bed tilt for only 30 seconds. For the future, DCS quantification can be improved. For example, a semi-infinite model was used to fit DCS data. This model simplifies the head geometry of the infants. In reality, the scalp, skull, cerebral spinal fluid, grey matter, and white matter possess different optical properties that can be accounted for, at least partially, in calculations [115, 149, 170]. Although the semi-infinite model can be improved upon, it provides a sufficient approximation for this pilot study. Finally, throughout our measurements we have assumed a constant absorption and reduced scattering coefficient ($\mu_a$ and $\mu_s'$) for all patients and for the duration of the study [166, 167]. The exact values used, however, had little affect on our results. For example, a tenfold change in $\mu_a$ and tripling $\mu_s'$ (0.01-0.15 $cm^{-1}$ and 5-15 $cm^{-1}$ respectively) did not significantly affect $\langle rCBF \rangle$ or the correlations between $BFI$ and $PSV$, $MV$, and $EDV$. Of course, individual deviations of $\mu_a$ and $\mu_s'$ from the population average could affect the strength of these correlations. Because our population of preterm infants was fairly homogeneous, i.e., clinically stable with no life threatening conditions and of approximately the same gestational age, we felt some justification in assuming $\mu_a$ and $\mu_s'$ to have little variation (i.e., less than 15%) across subjects, as is the case for full term neonates [100, 171]. Future work would, however, benefit from the use of a hybrid

DCS/DOS instrument [63, 64, 115, 172] to gather absolute optical properties from DOS for each patient individually and then employ them when fitting for BFI.

### 5.2.4 Conclusion

We have demonstrated the feasibility of diffuse correlation spectroscopy to continuously monitor changes in cerebral blood flow in very low birth weight preterm infants. The skull anatomy of preterm infants enables us to probe a significant amount of the cortex, making them an attractive patient population for bedside DCS measurements. Physiologically, we also showed that when posed with a small head of bed angle challenge of 12º, the infants maintained a constant blood flow on the *microvascular* scale. This result was corroborated in the macrovasculature by findings from transcranial Doppler ultrasound measurements. Measurements of blood flow index as measured by DCS were found to correlate significantly with measurements of peak systolic, end diastolic, and mean velocities of the middle cerebral artery calculated with TCD. These results further validate diffuse correlation spectroscopy as an accurate monitor of cerebral blood flow.

# 6 Applications of DOS/DCS in Patients with Heart Defects

## 6.1 Introduction

Approximately 35,000 infants are diagnosed yearly with congenital heart defects (CHD) [6]. A third of these infants will have severe, complex cardiac lesions that will require surgical repair in the first few months of life. Importantly, cardiac surgery for serious forms of CHD in the neonatal period has progressed to the point wherein mortality is minimal. Thus, clinicians are now focusing on the prevention of neurologic injury and the improvement of neurocognitive outcome in these high-risk infants. This chapter is structured as follows: Section 6.1 briefly motivates the need for cerebral monitoring of patients with congenital heart defects; Section 6.2 describes the study protocol used to monitor these patients before and after cardiac surgery; Section 6.3 describes the patient population recruited for our studies; and Section 6.4 summarizes four preliminary results obtained from these measurements, namely the effects of hypercapnia, blood transfusion, and sodium bicarbonate bolus, as well as the progression of tissue oxygen saturation and cerebral blood volume following cardiac surgery.

### 6.1.1 Neurological Injury Accompanying CHD: Periventricular Leukomalacia & Structural Brain Immaturity

Patients with severe forms of CHDs encounter both short-term and/or longer-term neurological consequences related to their heart defect. Recent literature has shown that patients with complex CHDs have immature brain development for their gestational age [126, 173]. Additionally, seizures, stroke, hemorrhages, and periventricular leukomalacia are observed post-operatively in a fraction of these patients [125, 174-

176].

Periventricular leukomalacia (PVL) is a specific form of necrosis of the cerebral white matter adjacent to the lateral ventricles. During the early stages of brain development, immature cells within this region of white matter are highly susceptible to injury from lack of blood flow and oxygen delivery [4, 177]. PVL is most often considered to be a neurological consequence of preterm birth because it occurs with high frequency in preterm infants [178]. The neurodevelopmental consequences of PVL in preterm infants include impaired motor function, developmental delay, microcephaly (a condition characterized by a significantly smaller brain than normal), cerebral palsy, and attention deficit/hyperactivity disorder (ADHD).

Patients with complex CHD requiring surgical repair in infancy have neurodevelopmental outcomes that are remarkably similar to those of preterm infants. At school age, these patients are at higher risk for impaired cognitive and fine motor skills, learning and speech problems, attention deficit/hyperactivity disorder (ADHD), and potentially lower IQ than the general population [7-10]. Since CHD patients share a common brain injury with preterm infants, i.e., PVL, it is thought that the presence of PVL leads to the neurodevelopmental deficits found in CHD patients.

Furthermore, recent work on CHD neonates has revealed structural brain immaturity. Examples of structural brain immaturity include delays in myelination (the insulation surrounding neurons), delays in cortical development, and delays in maturation of the germinal matrix and glial cell migration [126, 173]. These effects are similar to the immature brain development observed in preterm infants, and they have been linked with the development of post-operative PVL [127]. Thus, by further

understanding the risk factors and the causes of development of new or worsened PVL in CHD patients, we may also gain new understanding of PVL in premature infants.

The incidence of preoperative PVL in CHD patients is thought to be about 25% [26, 179]. Risk factors for this injury have been discovered. McQuillen *et al* have reported that the use of balloon atrial septostomy, a procedure performed to further open the atrial septal defect (see Section 6.1.3), was highly correlated with pre-operative injury in patients with transposition of the great arteries, a specific form of CHD (see Section 6.1.4) [180, 181]. Furthermore, recent evidence points to longer time-to-surgery and low oxygen content in the arterial blood as predictors of preoperative PVL [182].

Data from post-operative MRI scans reveal a substantially higher incidence (i.e., greater than 50 %) of new or worsened post-operative injury, mainly in the form of PVL [26, 125, 179]. Perioperative risk factors for this post-operative injury include high base deficit (indicating excessive acid in the body) during cardiopulmonary bypass (CPB), low cerebral tissue oxygen saturations [180], and prolonged exposure to CPB [180]. Risk factors in the early (i.e., less than 48 hours) post-operative period include diastolic hypotension, hypoxemia, and tissue oxygen saturations that remained low, i.e., < 45 % for longer than 180 minutes [125, 174, 180].

This chapter highlights the use of both pre- and post-operative DOS/DCS monitoring in an effort to further elucidate the effects of CHD physiology on cerebral hemodynamics and to potentially predict and/or avoid adverse outcome in the form of PVL. Our clinical studies focus on two main congenital heart defects: Transposition of the Great Arteries (TGA) and Hypoplastic Left Heart Syndrome (HLHS). Both diagnoses are forms of ductal dependent heart lesions, i.e., legions dependent on the ductus

arteriosus for systemic or pulmonary blood flow. As of 2000, these ductal dependent heart legions occur in approximately 7 out of 10,000 live births [6, 183]. These defects are dependent on an open ductus arteriosus (a shunt connecting the pulmonary artery to the aorta) and an open atrial septal defect (a shunt connecting the right and left atria) for mixing of systemic and pulmonary blood to provide oxygenated blood flow to the brain and body. Additionally, for survival, both of these defects require surgical repair (TGA) or palliation (HLHS) within the first week of life. The remainder of Section 6.1 will provide a brief review of normal circulation and will discuss these two defects and their surgical repair in more depth.

### 6.1.2 Physiology of a Healthy Heart

Figure 36 shows a schematic of healthy circulation in a healthy heart. In a healthy heart, the right side of the heart pumps deoxygenated blood to the lungs, while the left side of the heart pumps oxygenated blood to the brain and body. Deoxygenated (venous) blood returns from the brain and body to the right atrium and is pumped to the lungs via the right ventricle and the pulmonary arteries. Oxygenated blood then returns from the lungs to the heart via the pulmonary veins into the left atrium, passes to the left ventricle, and is then pumped through the aorta to the brain and body [184].

### 6.1.3 Hypoplastic Left Heart Syndrome (HLHS)

HLHS is a particularly severe form of CHD characterized by an underdeveloped, or hypoplastic, left ventricle, and stenosed or atretic (closed) mitral and aortic valves [185]. Due to the lack of blood flow out of the left side of the heart, the aortic valve (the valve separating the aorta and left ventricle) and the ascending aorta (the portion of the aorta

immediately coming off of the left ventricle) becomes hypoplastic or atretic. These malformations are fatal if not corrected and require surgery within the first week of life.

Palliative cardiac surgery for HLHS is performed in a series of three staged reconstructions. All patients included in our studies undergo the first stage of surgery, known as the Stage I/Norwood procedure. The goal of the Norwood procedure is to build a new aorta (dubbed a "neoaorta") to carry blood to the body, brain, and lungs. Since the aorta is severely hypoplastic, the pulmonary artery is connected to the aorta to permit adequate systemic outflow. An artificial shunt is then connected to the first vessel that arises from the aorta with the other end connected to the pulmonary artery to provide blood flow to the lungs. Since the left ventricle is inadequate in size (or there is no left ventricle at all), the right ventricle serves as the systemic ventricle to pump blood through the new outflow tract. In addition, with only one ventricle, there must be adequate mixing of both deoxygenated and oxygenated blood. An atrial septectomy is

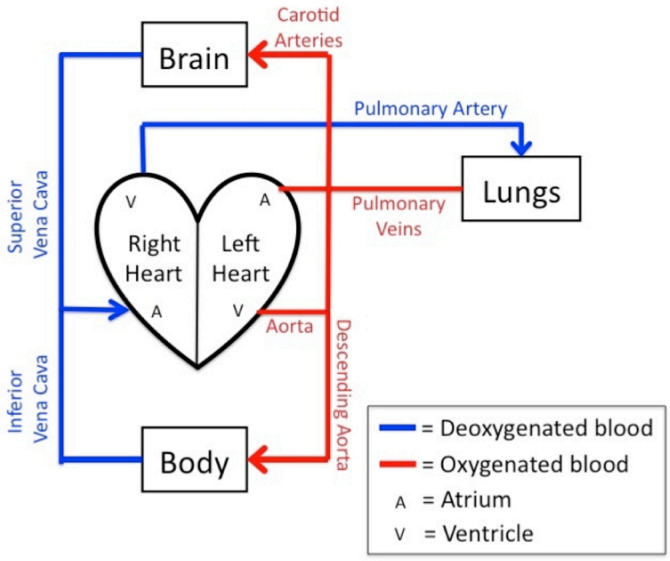


Figure 36, Schematic of healthy circulation in a normal heart. The aorta carries oxygen rich blood from the left ventricle to the systemic circulation. Venous blood returns from the systemic circulation into the right atrium and is pumped to the lungs via the pulmonary arteries. Oxygenated blood from the lungs returns to the heart via the pulmonary veins.

performed to permanently open the connection between the atria and to create an unobstructed source of systemic (oxygenated) blood flow and a stable source of blood flow to the lungs. In practice, patients are first anesthetized (isoflurane, fentanyl, pancuronium) and orally intubated. Then they are cooled to approximately 25 to 28°C and placed on cardiopulmonary bypass, whereby a cannula is placed in the aorta and in the right atria to bypass the heart. Because of the intricacies of the surgical technique, the heart must be stopped. Thus, the patient is cooled further to 18 to 20°C, and the heart is isolated from the rest of the body by clamping the pulmonary artery. Deep hypothermic circulatory arrest is maintained for approximately 45 to 60 minutes to complete the surgical procedure, at which time the patient is re-warmed to 34°C and is separated from cardiopulmonary bypass.

### 6.1.4 Transposition of the Great Arteries (TGA)

As the name suggests, TGA involves the transposition of the aorta and the pulmonary artery [185]. The aorta stems from the right ventricle and the pulmonary artery comes off the left ventricle. These malformations are typically repaired during the first few days of the first week of life in order to preserve the left ventricle's ability to support systemic circulation.

Surgical repair to correct for TGA is called the arterial switch procedure. This procedure effectively moves the aorta and pulmonary artery so that deoxygenated blood is pumped to the lungs and oxygenated blood is pumped to the brain and body. Patients are first anesthetized (isoflurane, fentanyl, pancuronium) and orally intubated. Then they are cooled to approximately 25 to 28°C and placed on cardiopulmonary bypass, whence a cannula is placed in the aorta and in the right atria to bypass the heart. The aorta and

pulmonary arteries are clamped off and then detached from their defective anatomy and finally reattached in the correct manner. The coronary arteries are excised from the aorta above the right ventricle and mobilized to the left ventricle outflow track. The patient is then re-warmed to 34°C and separated from cardiopulmonary bypass.

## 6.2 Study Protocol

With institutional review board (IRB) approval, all full-term newborn infants with complex CHD admitted to the cardiac intensive care unit at The Children's Hospital of Philadelphia were screened for participation in this study. Inclusion criteria included full term age (gestational age $40 \pm 4$ weeks), an intention to undergo surgery with cardiopulmonary bypass (CPB) with or without deep hypothermic circulatory arrest (DHCA), medical stability for 24 hours prior to surgery, and admission CHD diagnosis of hypoplastic left heart syndrome (HLHS) or transposition of the great arteries (TGA). Exclusion criteria included: small for gestational age (< 2 kg), a history of neonatal depression (5 minute APGAR score < 5 or umbilical cord pH < 7.0), or evidence of other end-organ dysfunction. In addition, subjects should not have experienced pre-operative cardiac arrest requiring chest compressions, and subjects with HLHS must not have been clinically treated with hypercarbia (increased inhalation of $CO_2$) for over-circulation to the lungs.

An overview of the clinical study timeline is shown in Figure 37. In brief, once parental consent was obtained, the patient underwent a pre-operative MRI on the morning of surgery to assess the extent, if any, of pre-operative brain injury, as well as to measure cerebrovascular reactivity during a hypercapnia intervention. Then, the patient was taken for cardiac surgery.

Following surgery, the patient was returned to the cardiac intensive care unit (CICU). Once stabilized, continuous monitoring of optical parameters, namely relative changes in cerebral blood flow (rCBF), changes in oxy-hemoglobin concentration ($\Delta C_{HbO_2}$), changes in deoxy-hemoglobin concentration ($\Delta C_{Hb}$), and changes in total hemoglobin concentration ($\Delta THC$), as well as continuous monitoring of vital signs (heart rate, arterial blood pressure, right atrial pressure, transcutaneous arterial oxygen saturations, temperature, and respiration rate) commenced for the next 10 to 12 hours while the patients underwent standard CICU post-operative management. Finally, a second MRI was performed 3 to 7 days after surgery to assess post-operative brain injury.

### 6.2.1 DOS/DCS Instrumentation

A hybrid DOS/DCS instrument (described in Section 2.2) was used for all optical measurements. Two separate optical probes are employed in this study (Figure 38). The first probe is intended solely for DOS measurement of *absolute* tissue absorption


Figure 37, Time line of study participation. Patients are monitored both pre- and post-operatively on the day of cardiac surgery, and are then imaged once more 3-7 days post-surgery. Blue arrows indicate acquisition of anatomical MRI images, green indicates surgery, and orange indicates continuous optical and vital sign monitoring (note the orange arrow prior to surgery indicates the monitoring performed during a hypercapnia intervention)

and reduced scattering coefficients. Herein we will refer to this DOS probe as the ISS infant probe, as it was purchased from ISS, Inc. The second probe is intended to quantify relative changes of both DOS and DCS parameters (i.e., not absolute

measures). Herein we will refer to this probe as the "flat probe" due to its slim geometry.

As shown in Figure 38A, the ISS infant probe (Infant Flexible Sensor, ISS, Inc.) consists of 8 source fibers and 1 detector fiber, and a total of 4 source-detector separations (1.5, 2.0, 2.5, and 3.0 cm). Two-wavelength (688 and 826 nm) DOS measurements are made at each separation. To quantify absolute optical properties using this probe, calibration measurements are made on a solid phantom prior to patient measurements. Specifically, the probe is placed on two separate solid ("semi-infinite") phantoms for calibration, and the semi-infinite geometry diffusion model is used to extract phantom optical properties and thus compute calibration corrections (see Section

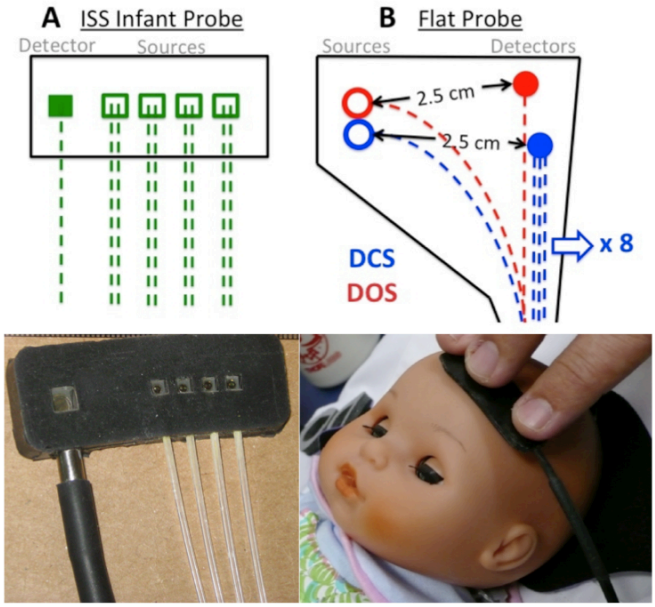


Figure 38, (TOP) A. Schematic of source/detector configuration for the ISS infant probe (separations 1.5, 2.0, 2.5, 3.0 cm) used for intermittent DOS measurements, B. Schematic of the flat probe used for DOS/DCS long term monitoring. (BOTTOM) Photos of the ISS neonate probe (left) and the flat probe on a baby doll (right).

2.1.3). The calibration coefficients computed with the solid phantoms are used to correct AC amplitude and phase-shift data obtained on the patient's forehead. Equations 41 and 42 are used to fit the slopes of AC amplitude ($A$) and phase shift ($\theta$) versus

separation for $\mu_a$ and $\mu_s'$ at 688 and 826 nm. Data is discarded if the Pearson's $R^2$ correlation coefficient for the relationship between $\ln(Ar^2)$ vs. $r$ or $\theta$ vs. $r$ is less than 0.975. Poor fit to the model may arise from poor probe contact, or possibly from laser light reaching the detectors without traversing through the tissue [99].

The flat probe was custom-made by Fiberoptic Systems (Simi Valley, CA). A schematic of the flat probe is given in Figure 38B. It consists of side-firing fibers cut at 45° angles to reduce the probe thickness to approximately 3 mm. Two source detector pairs, both separated by 2.5 cm, are imbedded in the probe for DOS and DCS measurements, respectively. The DOS source fiber is 200 μm in diameter, while the detector fiber diameter is 600μm. The DCS source fiber diameter is also 200 μm, but on the detector side we employ a bundle of 8 single mode detectors (these single mode fibers are used increase the signal-to-noise ratio by averaging over all 8 detectors). The optical probe was secured to the patient's forehead using a soft foam mask.

### 6.2.2 MRI Measurements

MRI images were acquired on a Siemens Avanto 1.5-Tesla MRI. Anatomical MRI sequences included multiplanar reconstructed (MPR) volumetric $T_1$ and $T_2$ SPACE (Sampling Perfection with Application optimized Contrasts using different flip-angle Evolutions) sequences acquired in the axial plane and later reconstructed in the sagittal and coronal planes. Susceptibility (both standard echo gradient and susceptibility weighted imaging), and diffusion weighted imaging (DWI) sequences were also acquired. A clinical neurologist (DJL) reviewed all images for presence/absence of new and/or worsened periventricular leukomalacia (PVL), stroke, and/or hemorrhages. Abnormalities were identified and localized using their signal intensity, appearance,

anatomic location, and presence or absence of diffusion positivity on diffusion weight images (indicating acute injury and low water motion).

### 6.2.3 Pre-Operative Measurements

On the morning of surgery, anesthesia induction and endotracheal intubation were performed in either the cardiac operating room or the cardiac intensive care unit. Sedation and neuromuscular blockage were maintained with 5-10 μg/kg fentanyl and 0.2 mg/kg pancuronium, respectively. If not already placed, arterial and venous lines for blood gases were also obtained.

For a subset of patients, baseline absolute optical property measurements were made while obtaining vascular access once the patient was sedated. For the measurements, the probe was manually held in place over the right and then left frontal cortices for 20 seconds. A black cloth was held over the probe to reduce the effects of stray room light. Measurements were repeated 4 times on each side for a total of 8 data points per patient. Data was discarded if the patient was moving, crying, or irritable during data collection. For the $j^{th}$ measurement (where j = 1 to 8) on the patient, the following system of equations was solved for concentrations of tissue oxy- and deoxy-hemoglobin, $C_{HbO_2}{}_j$ and $C_{Hb}{}_j$, respectively:

$$\mu_{a}{}_j(\lambda_i) = \epsilon_{Hb}(\lambda_i)C_{Hb}{}_j + \epsilon_{HbO_2}(\lambda_i)C_{HbO_2}{}_j + 0.75\mu_{a}{}_{H_2O}(\lambda_i). \quad [76]$$

Here $\epsilon_{HbO_2}(\lambda_i)$ and $\epsilon_{Hb}(\lambda_i)$ are the extinction coefficients of oxy- and deoxy-hemoglobin at the wavelengths, $\lambda_i$, employed (688 and 826 nm). The absorption effects of water ($\mu_{a}{}_{H_2O}(\lambda_i)$) were accounted for by assuming a tissue water content of approximately

75% [99, 186]. Total hemoglobin concentration of the j[th] measurement, $THC_j$, was defined as $THC_j \equiv C_{Hb_j} + C_{HbO_{2_j}}$, and cerebral oxygen saturation, $ScO_{2_j}$, was defined as $ScO_{2_j} \equiv C_{HbO_{2_j}}/THC_j \times 100\%$. Finally, for each patient, a simple mean and standard deviation were computed over all 8 measurements (assuming that no data was thrown out because of poor data quality or patient motion). Sample pre-operative THC and $ScO_2$ data is seen in Figure 39. Note that although data is collected on both right and left head, for the purposes of this analysis, we are averaging over all data to obtain a global mean.

The subject was then transported to the MRI suite. On arrival at the MRI suite an arterial blood sample was drawn to assess baseline arterial partial pressure of carbon

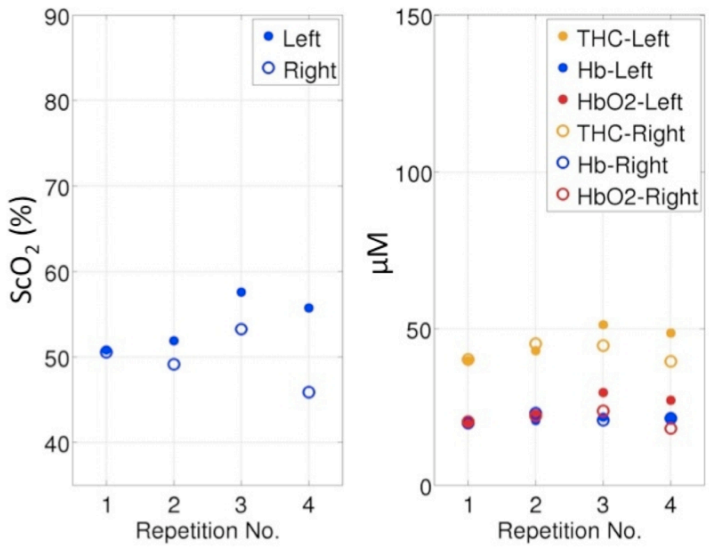


Figure 39, Pre-operative measurements of baseline $ScO_2$, $C_{HbO_2}$, $C_{Hb}$, and THC using the ISS infant probe.

dioxide ($pCO_2$) and arterial oxygen saturations using co-oximetry (AVOX 1000, Opti Medical Systems). A venous blood sample is also drawn to assess venous oxygen saturations using co-oximetry.

Figure 40 shows the hypercapnia study protocol that commenced once the patient arrived at the MRI scanner (also described by Durduran et al [59]). The flat optical probe was placed on the patient's forehead off-of-midline and secured gently with a foam mask for continuous DOS/DCS monitoring of relative changes in cerebral blood flow, oxy- and deoxy-hemoglobin concentrations. Optical data was acquired every 3.5 seconds. After a 30-minute baseline period of room air inhalation, supplemental $CO_2$ was added to the inspired gas mixture until an inspired $CO_2$ of 2.7% was achieved (measured by a capnometer, a device that measures partial pressure of $CO_2$ in the inspired gas mixture). $CO_2$ remained on for approximately 30 minutes. Vital signs were continuously captured during the procedure, i.e., electrocardiogram, cuff blood pressure, transcutaneous oxygen saturations, and fractional inspired $CO_2$. Anatomical MRI scans were obtained throughout the experiment too (see Section 6.2.2). Arterial blood samples are drawn during the baseline period and again at the end of hypercarbia in order to assess changes in $pCO_2$. Venous and arterial blood gas co-oximetry was obtained for accurate blood oxygen saturations.

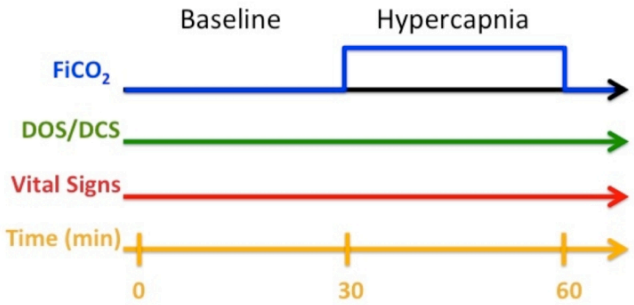


Figure 40, Timeline of the preoperative hypercapnia experiment. Optical (DOS/DCS) measurements, along with vital signs were captured continuously for the duration of the 60-minute study. $CO_2$ was added to the inspired gas mixture at 30 minutes to produce hypercapnia.

### 6.2.4 Post-operative Continuous Monitoring

The patient returned to the cardiac intensive care unit following surgery and was

stabilized before the start of any post-operative measurements. Following stabilization, the flat optical probe was secured to the patient's forehead with a foam mask for continuous monitoring of relative changes in cerebral blood flow, and oxy- and deoxy-hemoglobin concentrations. Complete sets of optical data were acquired every 7.5 seconds. The flat probe was repositioned every 2 hours to the contralateral side of the forehead to minimize risk of burns or pressure sores. A researcher was at the bedside for the duration of the post-operative monitoring. Marks were made in the optical data files to denote any interventions or manipulations that might occur, i.e., drug delivery, movement, examinations, etc.

Vital signs were also captured continuously using a Component Neuromonitoring System from Moberg Research, Inc. Heart rate, arterial blood pressure, transcutaneous oxygen saturations, respiration rate, temperature, and right atrial pressures were all recorded at a rate of 0.5 Hz. Vital sign data was manually time-locked with optical data at the start of recording.

For a subset of patients recruited most recently (N=10), absolute measurements of absorption and reduced scattering coefficients were made intermittently using the ISS infant probe (note that for the other patients, absolute measurements were not acquired, only relative changes from a presumed baseline absorption coefficient value were obtained). When the patient returned from surgery, absolute measurements were made to assess baseline values; then the flat probe was placed on the patient to measure relative changes in the absorption coefficient. Subsequently, every 2 hours when the flat probe is repositioned, we made an absolute DOS measurement with the ISS probe using the procedures listed in Section 6.2.1. Note, the ISS probe and the flat probe were

never used at the same time on the infant's head due to size constraints.

## 6.3 Patient Population

To date, we have recruited twenty-nine full term infants with complex congenital heart disease. Fourteen were diagnosed with HLHS, and fifteen were diagnosed with TGA. One patient was not measured because his condition worsened before the day of surgery. Median and interquartile range (IQR) of all patient demographics are summarized for the 28 patients studied in Table 10.

Table 11 lists the portion(s) of the study in which each patient participated. As seen from this table, twenty-eight patients completed the pre-operative MRI to assess pre-operative brain injury. All twenty-eight patients also completed the pre-operative hypercapnia portion (listed as "Pre-Op $CO_2$ Study" in Table 11) of the study as well, although the data from one patient (Patient ID = 3) was discarded due to poor optical data quality (low intensities of both DCS and DCS detected light). Twenty-seven patients completed the post-operative optical/vital-sign monitoring portion of the study, although only 25 were included for analysis due to poor optical data (low intensity of either DOS and/or DCS data). Additionally, absolute optical properties were obtained prior to the pre-MRI hypercapnia experiment as well as intermittently throughout the

| | Median (IQR) |
|---|---|
| Cardiac Diagnosis (HLHS/TGA) | N = 14/15 |
| Sex (Male/Female) | N = 16/13 |
| Gestation Age (weeks) | 39 (1.6) |
| Day of Life | 3 (2) |
| Birth weight (kg) | 3.26 (0.55) |
| Head Circumference (cm) | 34 (1.1) |

Table 10, Patient characteristics summarizing all 28 patients studied. Data is reported as median (interquartile range).

post-operative MRI for the last ten patients. Finally, 25 patients completed the post-operative MRI assessment of brain injury.

## 6.4 Initial Results

### 6.4.1 Pre/Post-operative Cerebral Oxygenation & Cerebral Blood Flow

#### *6.4.1.1 Motivation - Cerebral Oxygenation & Cerebral Blood Flow*

For patients with congenital heart defects, several publications have implicated low tissue, venous, and/or arterial oxygen saturations in the pre- and post-operative periods as contributors to adverse outcome (e.g., longer hospital stay, extracorporeal membrane oxygenation support, organ failure, death) or brain injury [174, 182, 187-192]. However, several difficulties arise when relying on arterial and/or venous oxygen saturations to predict adverse outcome. Arterial oxygen saturations are poor indicators of actual oxygen delivery at the brain tissue level in patients with cyanotic congenital heart defects [188, 192, 193]. Thus if one is monitoring only arterial oxygen saturations, then one may overlook poor oxygen extraction at the tissue level as a predictor of adverse outcome. Alternatively, while cerebral venous saturations are a valuable measure indicative of cerebral oxygen extraction, [189, 190, 192, 193] monitoring cerebral venous saturations requires invasive and potentially dangerous catheterization of the superior vena cava.

| ID | Cardiac Dx | Pre-Op MRI | Pre-Op $CO_2$ Study | Post-Op Vital-Sign & Optical Monitoring | Absolute Optical Properties | Post-Op MRI | Study Portion |
|---|---|---|---|---|---|---|---|
| 1 | HLHS | X | X | X | | X | b |
| 2 | TGA | | | | | | |
| 3 | HLHS | X | X | X | | X | |
| 4 | HLHS | X | X | X | | X | b,d |
| 5 | HLHS | X | X | X | | X | b,c |
| 6 | HLHS | X | X | X | | X | b,c |
| 7 | TGA | X | X | X | | X | b |
| 8 | TGA | X | X | | | X | b |
| 9 | TGA | X | X | X | | X | b |
| 10 | TGA | X | X | X | | X | b |
| 11 | TGA | X | X | X | | | b |
| 12 | HLHS | X | X | X | | X | b,c,d |
| 13 | TGA | X | X | X | | X | b |
| 14 | TGA | X | X | X | | X | b,c,d |
| 15 | HLHS | X | X | X | | | B,c |
| 16 | TGA | X | X | X | | X | b |
| 17 | HLHS | X | X | X | | X | b,c |
| 18 | TGA | X | X | X | | X | b |
| 19 | TGA | X | X | X | | X | b,d |
| 20 | TGA | X | X | X | X | X | a,b |
| 21 | HLHS | X | X | X | X | X | a,b,c,d |
| 22 | HLHS | X | X | X | X | X | a,b,c |
| 23 | HLHS | X | X | X | X | X | a,b,d |
| 24 | TGA | X | X | X | X | X | a,b |
| 25 | TGA | X | X | X | X | X | a,b,c |
| 26 | HLHS | X | X | X | X | X | a,b,c |
| 27 | TGA | X | X | X | X | X | a,b |
| 28 | HLHS | X | X | X | X | X | a,b,c,d |
| 29 | HLHS | X | X | X | X | | a,b,c |
| | 14/15 | 28 | 28 | 27 | 10 | 25 | |

Table 11, Summary of the patients recruited and measured for each portion of the study. An X indicates that optical and/or MRI data was obtained. A red X indicates that optical data quality was too poor for patient inclusion in our final analysis. The far right column indicates the portion(s) of the study in which each patient participated: a = absolute optical properties (Section 6.4.1), b = hypercapnia (Section 6.4.2), c = sodium bicarbonate (Section 6.4.3), d = blood transfusion (Section 6.4.4).

Non-invasive cerebral tissue saturations ($ScO_2$) measured by NIRS offer a natural compromise to monitoring arterial or venous saturations. However, to my knowledge, all $ScO_2$ data reported to date were obtained with commercially available NIRS devices, which are fairly reliable as trend monitors, but are not reliable for absolute quantification as they operate in the CW domain (see Section 2.1.1).

| | Median (IQR) |
|---|---|
| Sex (M/F) | N = 6/4 |
| Gestation Age (weeks) | 39.1 (1.4) |
| Day of Life (days) | 3 (1.5) |
| Birth Weight (kg) | 3.24 (0.32) |
| Head Circumference (cm) | 33.8 (1.0) |

Table 12, Patient characteristics.

Thus, in the present investigation we aim to monitor pre- and post-operative cerebral oxygen saturations, $ScO_2$, in patients with CHD using a frequency domain, multi-separation DOS instrument that is much more sophisticated and provides substantially more comprehensive information than the commercially available NIRS products used in previous work [174, 191]. In particular, our DOS instrumentation permits quantification of not only $ScO_2$, but also of total hemoglobin concentration, THC, a parameter related to cerebral blood volume, and of the reduced scattering coefficient of the tissue, a parameter related to the cellular structure and density. We hypothesize that patients with sustained low tissue oxygen saturations ($ScO_2$), low cerebral blood volume (THC), and/or low tissue scattering will be more susceptible to developing new or worsened PVL as seen by MRI 3-7 days post-surgery (see Section 6.2.2).

#### *6.4.1.2 Optical Measurements- Cerebral Oxygenation & Cerebral Blood Flow*

The protocol for making absolute measurements of pre- and post-operative $ScO_2$, THC, and $\mu_s'(\lambda)$ using the ISS neonate probe is described in detail in Section 6.2. Each patient had a pre-operative measurement of THC and $ScO_2$ taken approximately 3 hours before surgery, followed by multiple post-operative measurements obtained when time and personnel permitted.

To quantify the blood flow index (BFI), the flat probe was secured to the forehead

following each session of absolute measurements. DCS intensity autocorrelation curves were acquired for approximately 2 minutes. This data was fit for the BFI by using the semi-infinite solution to the correlation diffusion equation with the optical properties, i.e., $\mu_a$ and $\mu_s'$, measured with the ISS neonate probe. A mean and standard deviation BFI was computed over the 2 minutes of monitoring

To standardize time lines for each patient, we define $t = 0$ as the time in which the patient was disconnected from the cardiopulmonary bypass (CPB) machine. For statistical analysis, post-operative measurements were binned into one of 3 categories: measurements made 0-4 hours post CPB, measurements made 4-8 hours post CPB, and measurements made 8-12 hours post CPB. If a patient had multiple measurements taken within one of these time periods, the measurements were averaged together.

A two-sided Wilcoxon rank sum test was used to test for differences between the distributions of pre-operative $ScO_2$, THC, $\mu_s'(\lambda)$, and BFI values and binned post-operative values. To test for differences in THC, $\mu_s'(\lambda)$, BFI and $ScO_2$ in patients with and without brain injury, data was binned according to presence or absence of injury and a two-sided Wilcoxon rank sum test was employed. A p-value of less than $0.05$ was deemed statistically significant.

#### *6.4.1.3 Results - Cerebral Oxygenation & Cerebral Blood Flow*

Ten patients were recruited for this study at the Children's Hospital of Philadelphia, N = 6 with hypoplastic left heart syndrome and N = 4 with transposition of the great arteries. Patient characteristics are summarized in Table 12. All ten patients underwent pre-operative MRI scans for neurological assessment. Periventricular leukomalacia (PVL)

| Brain Injury | Pre-Surgery | 1 Week Post-Surgery |
|---|---|---|
| Periventricular Leukomalacia (Yes/No) | N = 1/9 | N = 3/6 |
| Stroke (Yes/No) | N = 0/10 | N = 0/9 |
| Hemorrhage (Yes/No) | N = 0/10 | N = 7/2 |

Table 13, Summary of brain injury in our cohort pre- and post-operatively.

was diagnosed in 1 out of the 10 pre-operative images. One patient opted out of the post-operative MRI. New or worsened PVL was revealed in 3/9 post-operative scans, microhemorrhages were seen in 7/9 post-operative scans, and stroke was observed in 0/9 post-operative scans, as seen in Table 13.

Median (range) of the pre-operative absorption and reduced scattering coefficients are summarized in Table 14. Note here that both absorption and scattering values are considerably lower than those of healthy neonates [100].

Figure 41 shows the progressions of $ScO_2$, THC, $\mu_s'(688\,nm)$, and BFI over time. Data is broken up into segments of time, i.e., pre-surgery (N = 10), 0-4 hours (N = 9), 4-8 hours (N = 9), and 8-12 hours (N = 9), and a boxplot of mean values of $ScO_2$, THC, $\mu_s'(688\,nm)$, and BFI is shown. It is evident from these figures that $ScO_2$ drops significantly in almost all patients 0-4 hours post-CPB as compared to pre-operative values ($p = 0.038$). Likewise, THC increases substantially 0-4 hours post-CPB as

| | Pre-Operative Median (Range) |
|---|---|
| $\mu_a(688\,nm)$ ($cm^{-1}$) | 0.078 (0.060 to 0.114) |
| $\mu_a(828\,nm)$ ($cm^{-1}$) | 0.075 (0.043 to 0.1103) |
| $\mu_s'(688\,nm)$ ($cm^{-1}$) | 4.5 (3.2 to 7.5) |
| $\mu_s'(828\,nm)$ ($cm^{-1}$) | 3.8 (1.3 to 6.1) |

Table 14, Median (range) values of the mean absorption and reduced scattering coefficients for N=10 pre-operative measurements.

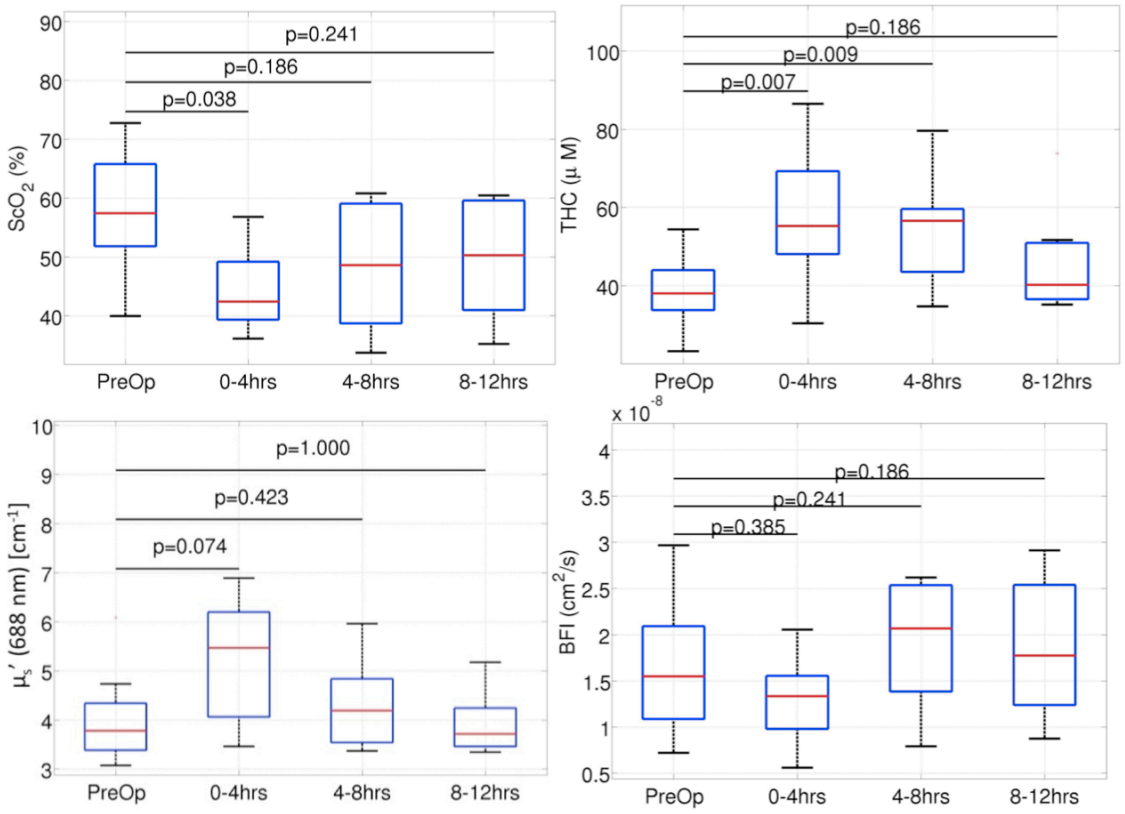


Figure 41, From top left to bottom right, boxplots of progressions of $ScO_2$, THC, $\boldsymbol{\mu_s'(688\,nm)}$, and BFI changes over time after cardiac surgery. For each box, the red line marks the median of the distribution, the blue box contains the 25th to 75th percentile of the data, and the whiskers extend to the most extreme data points not considered outliers. p-values less than 0.05 indicate a significant difference between the post-operative data in a given time bin and the pre-operative data.

compared to pre-operative values (p = 0.007). Both $ScO_2$ and THC appear to return back to pre-operative levels over the course of 8-12 hours post-CPB (p = 0.241 and p = 0.121, respectively). No significant differences were observed between pre- and post-operative values of the blood flow index or reduced scattering coefficient. However, $\mu_s'(688\,nm)$ does increase slightly in the first 0 to 4 hours after surgery as compared to pre-operative values (p = 0.074), after which time $\mu_s'(688\,nm)$ returns to pre-operative levels.

Dichotomizing patients by the presence of absence of PVL revealed differences

between populations by 8-12 hours post-CPB (see Figure 42). While the results do not quite reach statistical significance, the trend in $ScO_2$ looks promising. These preliminary results, although they are only from a small number of patients, suggest that patients who develop new or worsened post-operative PVL have lower oxygen saturations 8-12 hours after surgery when compared to those without PVL. No differences were observed in THC, $\mu_s'(\lambda)$, or BFI between patients with and without PVL (data not shown).

#### *6.4.1.4 Discussion - Cerebral Oxygenation & Cerebral Blood Flow*

This study has examined the progression of pre- and post-operative measures of cerebral tissue oxygen saturation ($ScO_2$) and total hemoglobin concentration (THC). $ScO_2$ decreases significantly between 0 to 4 hours after surgery in all patients and then returns to pre-operative values in most patients. Cerebral blood volume, represented by THC, increases substantially in the 0 to 8 hour period after cardiac surgery and does not

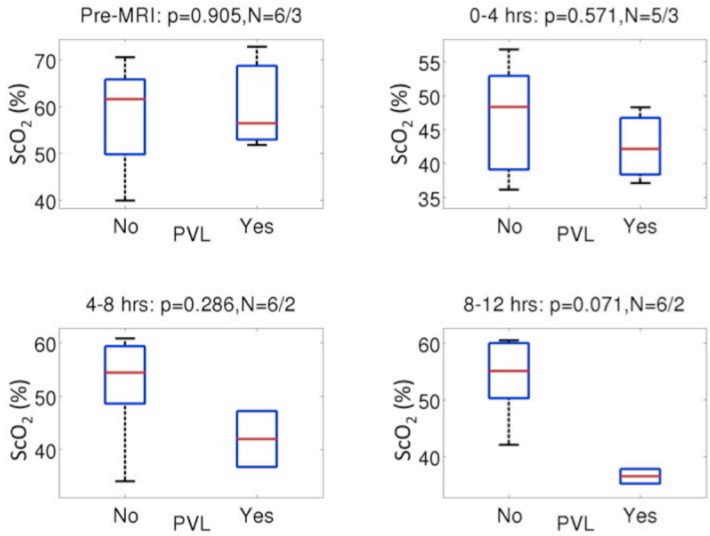


Figure 42, Comparison of $ScO_2$ values of patients with and without white matter brain injury (PVL). Titles of each subplot reflect the time period being plotted and the number of patients in the No PVL/PVL groups. By 8-12 hours post-surgery, patients with PVL may have lower $ScO_2$ values than those without injury.

return to pre-operative levels until 8 to 12 hours post-surgery. A decrease in $ScO_2$, despite the increase in cerebral blood volume, may suggest a problem with gas exchange in the lungs in the early post-operative period (~0 to 8 hours). Swelling in the lungs, which is often observed in the post-operative period in these patients, may potentially cause insufficient oxygen exchange in the lungs. Alternatively, increased cerebral oxygen consumption due to increased neuronal metabolic rate during recovery from cardiopulmonary bypass may explain the fall in $ScO_2$ and rise in THC. Further investigations into pulmonary gas exchange and post-operative cerebral metabolism will clarify the mechanisms for the behavior of $ScO_2$ and THC after surgery.

Additionally, we observed that patients who develop post-operative periventricular leukomalacia (PVL) have the lowest tissue oxygen saturations 8 to 12 hours after surgery. While these results do not quite reach statistical significance, they are promising and consistent with the idea that PVL is a form of brain injury caused by lack of oxygen. Patient recruitment is ongoing in order to improve our statistics and to investigate the relationship between post-operative $ScO_2$ values and the extent of the PVL legion.

Arterial oxygen saturations are poor indicators of actual oxygen delivery at the brain tissue level [188, 192, 193]. The results of our study strengthen the argument for monitoring $ScO_2$ continuously in the post-operative period, rather than just monitoring transcutaneous $SaO_2$. After surgery, all TGA patients had $SaO_2$ of ~100%. Therefore, low cerebral saturations would be undetectable by pure pulse-oximetry or arterial blood gas readings. Furthermore, if while monitoring $ScO_2$, it is determined that cerebral saturations are lower than desired, then there are clinical methods to improve $ScO_2$, e.g.

by increasing oxygen delivery or by decreasing oxygen metabolism. Transfusion of blood products may increase oxygen delivery. Neuromuscular blockades, sedation, mechanical ventilation to reduce the burden of respiration, afterload reducers to improve diastolic function, and/or controlled cooling may be suitable options to decrease oxygen metabolism.

One other striking finding from this work is the very low reduced scattering coefficient measured at both wavelengths employed. Zhao et al has published absorption and reduced scattering coefficients for healthy term infants using a homodyne frequency domain instrument at 3 wavelengths, 788, 814, and 832 nm [100]. While the absorption coefficients measured by Zhao were comparable to our pre-operative values, they observed a mean reduced scattering coefficient (N = 23) of almost twice our measured pre-operative median value (3.8 $cm^{-1}$ versus 8.4 $cm^{-1}$ at 830 nm). The scattering coefficient we observed in this population is actually much more similar to that of preterm infants (5 $cm^{-1}$ [194]). This low scattering value may therefore be due to the relative immaturity of these patient's brains and the lesser degree of myelination [93, 126, 195, 196].

Finally, we note that several assumptions went in to the optical measurements of $ScO_2$, THC, and $\mu_s'$. The region under the optical probe was assumed to be a semi-infinite medium with homogenous optical properties. This assumption appears to be valid, as the mean distance to the cortex measured via anatomical MRI scans of 0.57 (0.13) cm, approximately 1/3 the distance of our smallest source-detector separation (1.5 cm). Thus, photons launched and received by all source-detector pairs spend the majority of their time in the cortex [197]. Additionally, we also assumed the coupling

coefficient between the phantom and the probe was roughly equivalent to the coupling between the optode and the skin; this assumption enabled us to calibrate the probe and to extract absolute optical properties. Despite these assumptions, our measurements of $ScO_2$ and THC fall well within the ranges measured in other neonatal populations [99, 100, 174, 191, 198].

#### *6.4.1.5 Conclusions - Cerebral Oxygenation & Cerebral Blood Flow*

Cerebral oxygen saturation, total hemoglobin concentration, reduced scattering coefficient, and blood flow index were measured in ten neonates with congenital heart defects before and intermittently for 12 hours following cardiopulmonary bypass surgery. Pre-operative reduced scattering coefficients in this population were considerably lower than literature values for healthy term infants, perhaps reflecting the relative brain immaturity in these infants as compared to healthy controls. Post-operatively, $ScO_2$ decreased significantly 0 to 4 hours after CPB compared with pre-operative values, and then $ScO_2$ slowly returned to pre-operative values. Post-operatively THC increased significantly and remained elevated compared to pre-operative values for up to 8 hours after CPB. Additionally, patients with periventricular leukomalacia, a specific form of hypoxic ischemic white matter injury, were distinguishable by a failure to recover to pre-operative $ScO_2$ levels by 8 to 12 hours.

By monitoring $ScO_2$ in CHD patients post-operatively, we can potentially predict PVL in future patients and develop treatment algorithms to prevent the injury. However, in order for these results to be clinically significant, we must increase the number of patients included in this analysis to account for factors that may confound our results, e.g. the influence of cardiac diagnosis. Thus, recruitment for this study is ongoing. We

hope to recruit at least twenty patients with both TGA and HLHS in order to dichotomize the population by both cardiac diagnosis and presence/absence of brain injury and to increase the statistical power of our results.

### 6.4.2 Hypercapnia

#### *6.4.2.1 Motivation - Hypercapnia*

$CO_2$ is the most potent regulator of cerebral circulation [199, 200]. The presence of elevated levels of $CO_2$ causes cerebral vasodilation, while low $CO_2$ levels causes cerebral vasoconstriction. $CO_2$ reactivity, defined as the change in cerebral blood flow (CBF) per change in arterial $pCO_2$, is a property of the physiologic reserve of cerebral blood flow in the cerebrovascular bed. Impaired $CO_2$ reactivity has been associated with poor neurodevelopmental outcome and a higher risk of death in all age groups [201-203].

CHD patients have a significant incidence of stroke and periventricular leukomalacia [125, 174-176, 179]. However, routine MRI scans of these patients to assess the presence of brain injury is not performed due to prohibitive cost. The onsets of both stroke and periventricular leukomalacia may be highly dependent on cerebral circulation, which, in turn, is highly dependent on changes in arterial $pCO_2$. In the following investigation of hypercapnia in our CHD population, we hypothesize that patients with lower than average $CO_2$ reactivity (i.e., those patients who have difficulty responding to fluctuations in $CO_2$) will be more likely to have some form of brain injury, e.g., stroke or PVL. If correct, impaired $CO_2$ reactivity could used as a clinical indicator of be measured as part of standard clinical practice to indicate the presence or absence

of brain injury, with impaired reactivity requiring further imaging tests to identify the specific form and extent of injury.

DOS and DCS are ideal modalities to non-invasively assess $CO_2$ reactivity at the bedside. Thus, in this investigation we employ concurrent DOS and DCS monitoring in neonates with congenital heart defects before cardiac surgery and during a hypercapnic intervention. Herein we describe the cerebral hemodynamic response to hypercapnia in these neonates, we obtain empirical data about cerebrovascular reactivity to hypercapnia, and we explore the relation of measured reactivity to brain injury in patients with ductal dependent CHD.

#### *6.4.2.2 Data Analysis - Hypercapnia*

For the DOS data analysis, we assume the scattering coefficient does not change during hypercapnia, and that the changes in the absorption coefficient are small compared to the baseline absorption coefficient values. Thus, we are effectively assuming that the modified Beer-Lambert (MBL) law can be employed for our patient population under the hypercapnia perturbation (see Sections 2.1.5 and 5.1), i.e.

$$\log\left(\frac{I(t,\lambda)}{I_0(\lambda)}\right) = -\Delta\mu_a(t,\lambda)L_{eff}(\lambda).$$

Here $I(t,\lambda)$ is the DC intensity of the detected diffuse light at wavelength $\lambda$ and time $t$, $I_0(\lambda)$ is the mean DC intensity at wavelength $\lambda$ during the baseline room air inhalation period, and $\Delta\mu_a(t,\lambda)$ is the change in absorption coefficient at wavelength $\lambda$ and time $t$ compared to at $t = 0$. To determine $L_{eff}(\lambda)$, baseline optical properties, i.e., tissue absorption and reduced scattering coefficients, were quantified approximately 30

minutes prior to the hypercapnia experiment in a subset of N=10 patients (see Sections 6.2.1 and 6.2.3). For these patients, $L_{eff}(\lambda)$ in the MBL law were computed exactly. Alternatively, if absolute optical properties were not measured, a mean $L_{eff}(\lambda)$ (calculated from the subset of the 10 CHD patients with absolute measures) was used.

For DCS data analysis, we solved the correlation diffusion equation analytically, assuming the sample geometry was a homogeneous, semi-infinite turbid medium. We then used the semi-infinite solution (see Section 3.1) to fit our data for a blood flow index (BFI). In the subset of patients for whom baseline $\mu_a$ and $\mu_s$' were measured (see Section 6.2), evolving optical properties were introduced as inputs into the DCS fits. In those patients for whom baseline $\mu_a$ and $\mu_s$' were not measured, a mean value from the measured subset of patients was employed along with the changes in $\mu_a$ computed with the MBL law, were input into the DCS fits (see Table 14). $rCBF$ was quantified using the following formula, $rCBF(t) = [BFI(t)/BFI_{BL}]\times 100\%$, where $BFI_{BL}$ is the mean blood flow index during the baseline room air inhalation period. Therefore, $rCBF(t)$ of 100% would indicate no change from baseline values.

A sample time series of DOS and DCS data from a single patient is seen in Figure 43 top and bottom, respectively. Changes in oxy-hemoglobin concentrations are in red, deoxy-hemoglobin concentrations is in blue, and cerebral blood flow is in green. $CO_2$ was added to the gas mixture at the ventilator inlet at approximately 40 minutes into the study. Data is missing around 25 minutes into the measurement due to an MRI sequence that caused a substantial motion artifact in the optical data.

To quantify the cerebral response to $CO_2$, mean values of the various optical parameters were computed before the onset of $CO_2$ and during a five-minute period after

stabilization of the response to $CO_2$ (~20 minutes). These five-minute periods for averaging are denoted with grey shaded rectangles in Figure 43. Changes in mean DOS measures of oxy-hemoglobin ($\Delta C_{HbO_2}$), deoxy-hemoglobin ($\Delta C_{Hb}$), and total hemoglobin ($\Delta THC = \Delta C_{HbO_2} + \Delta C_{Hb}$) were calculated as a difference between hypercapnia and baseline means. The mean relative change in CBF ($rCBF$) was found using a ratio of hypercapnic DCS blood flow index to baseline DCS blood flow index. $CO_2$ reactivity was quantified as the ratio of $\Delta rCBF$ per change in $pCO_2$ as measured with arterial blood gas, where $\Delta rCBF \equiv rCBF - 100\%$. A Wilcoxon signed rank test was used to test if the median of each variable's distribution was significantly different from zero ($p < 0.05$) [137].

In the subset of 10 patients, from whom we obtained absolute baseline optical properties, relative changes in the cerebral metabolic rate of oxygen extraction ($rCMRO_2$) was quantified. $rCMRO_2$ was calculated using the following formula (discussed and derived in depth in [62, 68]:

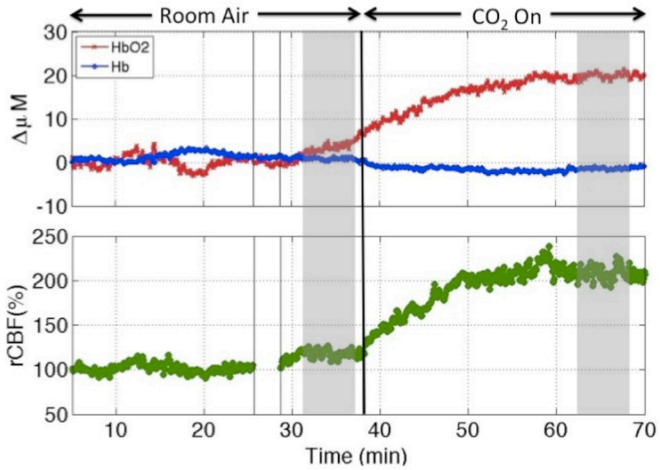


Figure 43, Sample time series of hypercapnia data. $CO_2$ is turned on at approximately 39 minutes. Grey rectangles indicate the time period that is averaged for statistical analysis.

$$rCMRO_2 = \left(\frac{SaO_{2_{HC}} - StO_{2_{HC}}}{SaO_{2_{BL}} - StO_{2_{BL}}}\right) \times rCBF - 100\%. \quad [77]$$

Here the subscript *HC* indicates a mean during hypercapnia and *BL* indicates a mean during the baseline period, $SaO_2$ is the arterial oxygen saturation calculated using co-oximetry on arterial blood samples, and $ScO_2$ is the tissue oxygen saturation discussed in Section 6.2. Again, an $rCMRO_2$ value of 100% would indicate no change in metabolism due to hypercapnia.

Additionally, Grubb's non-linear relation [204], which describes the relationship between relative changes in total hemoglobin concentration ($rTHC$) and $rCBF$, was tested in this population with a multivariate fit for $b$ in the following equation:

$$rCBF = rTHC^b. \quad [78]$$

Here we define $rTHC = (\Delta THC + THC_{BL})/THC_{BL}$, where $THC_{BL}$ is the baseline THC. For a subset of N=10 patients, $THC_{BL}$ was measured using a multi-distance fitting algorithm based on analytic solutions in the frequency domain semi-infinite homogeneous medium diffusion approximation (see Sections 6.2.1 and 6.2.3). For the other patients for whom we did not obtain baseline THC values, $THC_{BL}$ was estimated using hemoglobin concentrations measured from arterial blood gas samples[6].

Structural MRI scans (see Section 6.2.2) determined the presence and the extent of periventricular leukomalacia (PVL). Patients were grouped according to the presence

[6] For the subset of patients with measured $THC_{BL}$, we observed a significant linear relationship between $THC_{BL}$ and arterial hemoglobin concentration (Hb) obtained from arterial blood gas samples ($R = 0.70$, $p < 0.05$). Thus, for patients without measured $THC_{BL}$, the value of $THC_{BL}$ was extrapolated based on baseline hemoglobin levels gathered from arterial blood gas samples.

or absence of PVL, and Wilcoxon rank sum tests explored differences in $CO_2$ reactivity between groups. Patients were also grouped according to cardiac diagnosis, and Wilcoxon rank sum tests explored differences between groups.

#### *6.4.2.3 Results- Hypercapnia*

As seen in the histograms in Figure 44, hypercapnia induced significant increases in $\Delta C_{HbO_2}$, $\Delta THC$, and $\Delta rCBF$ in almost all subjects ($p < 0.001$). Because each patient received slightly different amounts of $CO_2$, data is reported as change in the parameter of interest per unit change in $pCO_2$ in order to compare between subjects in a more objective manner. For reference, vertical dotted lines are added to denote no change due to hypercapnia. On average, $rCMRO_2$ and $\Delta Hb$ showed no significant changes due to hypercapnia ($p = 0.32$ and 0.29, respectively), although some individual patients exhibited substantial responses of these parameters in both the positive and negative

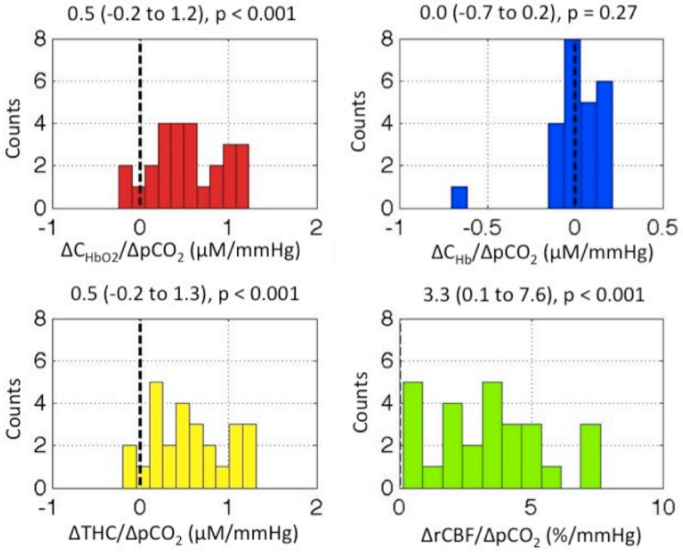


Figure 44, Histograms of mean changes in $\Delta C_{HbO_2}$, $\Delta C_{Hb}$, $\Delta THC$ and $\Delta rCBF$ per change in arterial $pCO_2$. For reference, vertical dotted lines are added to denote no change due to hypercapnia. The title of each subplot indicates median (range) $CO_2$ reacitivities, along with p-values.

| Parameter | Median (IQR) | p-value |
|---|---|---|
| $\boldsymbol{\Delta pCO_2}$ (mmHg) | 26 (16) | <0.001 |
| Δ rCBF (%) | 79.5 (54.4) | <0.001 |
| $\boldsymbol{\Delta HbO_2}$ (μM) | 13.4 (9.0) | <0.001 |
| $\boldsymbol{\Delta Hb}$ (μM) | 0.8 (3.7) | 0.29 |
| $\boldsymbol{\Delta THC}$ (μM) | 13.8 (9.6) | <0.001 |
| $CO_2$ Reactivity (%/mmHg) | 3.3 (2.9) | <0.001 |
| $rCMRO_2$ (%)* | 7.1 (53.8) | 0.32 |

Table 15, Median and interquartile range changes in the measured hemodynamic parameters. p-values were computed using a Wilcoxon signed rank test. *Note that $rCMRO_2$ was only measured in 10 out of 27 patients.

directions. Median (interquartile range) changes and p-values obtained from Wilcoxon signed rank test are summarized in Table 15.

To explore the relation between changes in blood volume and changes in blood flow, Figure 45 is a scatterplot depicting the non-linear relationship between $rCBV$ and $rCBF$ along with error bars of each variable. In order to estimate the Grubb's exponent, a linear regression of $\log(rCBF)$ versus $\log(rCBV)$ was performed and revealed an estimate (95% confidence interval) of the Grubb exponent of 0.35 (0.11, 0.58). This relationship is significant ($p = 0.005$), albeit with an $R^2$ of only $0.28$. Our value of the

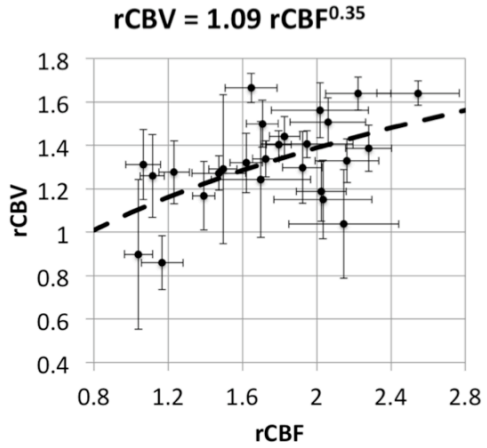


Figure 45, Relationship between $\boldsymbol{rCBV}$ and $\boldsymbol{rCBF}$ during hypercapnia.

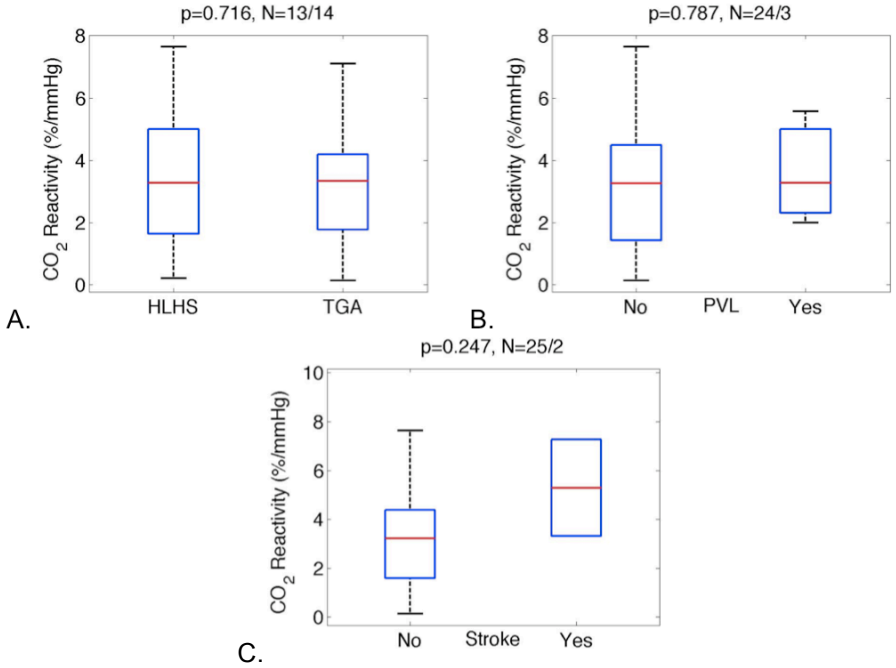


Figure 46, Differences in $CO_2$ reactivity between A. patients with HLHS versus TGA, B. patients without pre-operative PVL and with pre-operative PVL, C. patients without and with pre-operative stroke.

Grubb's exponent agrees fairly well with previously published results, which range from 0.28 to 0.38 [205].

As shown in Figure 46, when grouped according to cardiac diagnosis, no significant differences in $CO_2$ reactivity were observed, i.e., patients with TGA (N=14) or with HLHS (N=13) react in a similar fashion to hypercapnia (p=0.72). When grouped according to presence (N=3) or absence (N = 24) of PVL, no significant difference in $CO_2$ reactivity was identified (p=0.79); however, N = 3 is small and probably adversely affects the statistics. Similarly, no differences in $CO_2$ reactivity were observed between patients with pre-operative stroke (N=2) and those without stroke (N = 25, p = 0.25). Again the small number of patients with pre-operative stroke may adversely affect the statistics.

#### *6.4.2.4 Discussion- Hypercapnia*

This work has demonstrated the effects of hypercapnia on neonates born with two particular forms of cyanotic heart defects: hypoplastic left heart syndrome and transposition of the great arteries. Significant increases in cerebral blood flow, concentration of oxy-hemoglobin, and total hemoglobin concentrations were observed during the hypercapnia perturbation. Deoxy-hemoglobin concentrations and cerebral metabolic rate of oxygen extraction showed no population averaged changes due to hypercapnia, an observation which agrees quite well with the handful of publications that have studied cerebrovascular reactivity to hypercapnia in patients with congenital heart defects using a variety of different measurement techniques, including NIRS, velocity mapping MRI, ASL-MRI, DOS and DCS [59, 142-145]. Durduran *et al* also used DCS to measure a mean (standard deviation) cerebrovascular reactivity to increased $CO_2$ of 3.1 (1.9) %/mmHg in neonates with congenital heart defects [59]. Our population of neonates is similar to that published by Durduran, and we found a comparable median (IQR) $CO_2$ reactivity of 3.3 (2.9) %/mmHg.

While the median $CO_2$ reactivity of these infants agrees well with other literature values, it should be noted that the values spanned a large range (0.15 to 7.6 %/mmHg). Thus, there exists a subset of the populations, with low $CO_2$ reactivity, suggesting a small cerebrovascular reserve of cerebral blood flow. We hypothesized that these patients would have the highest incidence of brain injury, an effect that has been seen [201-203]. Yet, as Figure 46 suggests, this hypothesis was not supported by the data in our study. No significant differences in the distributions of $CO_2$ reactivity were observed in patients with and without brain injury. One caveat, of course, is that we have a rather

small sample size of the injured population (less than 10% of our patients had injury). Alternatively, the injury suffered by our patient population is much less severe than that reported in the previous works that cited a relation between impaired $CO_2$ reactivity and adverse outcome. Perhaps this population with more "minor" brain injury does not have impaired $CO_2$ reactivity.

The results presented herein also demonstrate a cross-validation between the parameters measured by the diffuse optical methods. A significant correlation was observed between relative changes in CBF (rCBF) and relative changes in cerebral blood volume (rCBV). The relationship between rCBF and rCBV is typically referred to as Grubb's relation [204]. Grubb's relation is frequently employed when a measure of only one of these two parameters is available. Boas and Payne provide a nice summary of published values Grubb's exponent in both humans and animals, ranging from 0.28 to 0.38 [205]. Our value of the Grubb's exponent agrees fairly well with previously published results. However, the 95% confidence interval for our Grubb's exponent is quite large (0.11 to 0.58). Thus, this data makes the argument for employing both DOS and DCS monitoring in order to have access to both rCBV and rCBF data. In the present population, Grubb's relation has a substantial amount of variation. Thus, if one employs only rCBF or rCBV alone in computations, the estimation of $rCMRO_2$ could have substantial errors.

*Other Limitations of Optical Data*

Due to the head size of the neonates studied, plus the fact that all measurements were performed in an MRI scanner, we were restricted to a single source-detector separation for the DOS measurements. Thus, the modified Beer-Lambert law was used

to quantify changes in the absorption coefficient and ergo changes in oxy- and deoxy-hemoglobin. However, many assumptions are required to employ the modified Beer-Lambert Law. In particular, it is assumed that $\Delta\mu_a$ is small relative to its baseline value, and we assume that $\mu_s'$ remains constant. These assumptions appear to be valid in the present experiment. On average, $\Delta\mu_a$ at 786 nm was 0.015 $cm^{-1}$, a change of approximately 15% of the presumed baseline value of $\mu_a$ = 0.1 $cm^{-1}$ at 786 nm. Similar results were found for 688 and 826 nm. Although we did not explicitly measure $\Delta\mu_s'$, other researchers have observed little or no change in $\mu_s'$ during similar experimental conditions [147, 171]. Thus we feel our assumption of constant $\mu_s'$ is justified.

To fit the DCS data for a blood flow index, we assumed initial values for the absorption and reduced scattering coefficients ($\mu_a$ and $\mu_s'$). Because we are only interested in relative changes in the BFI, our choice of initial $\mu_a$ and $\mu_s'$ has little to no effect on the resulting value of rCBF. However, changes of $\mu_a$ and $\mu_s'$ that occur during the duration of the study may influence the magnitude of rCBF. For this reason, we incorporated changes in $\mu_a$ obtained with DOS into our fitting procedure for BFI. However, as mentioned previously, our DOS analysis assumed that the scattering coefficient remained constant for the duration of the study. This assumption is most likely valid for hypercapnia (see Section 5.1). However, if false, a 10% increase in the scattering coefficient could alter the magnitude of rCBF by as much as 20%. Thus, future work would benefit greatly from the use of multiple source detector DOS amplitude and phase measurements used to continuously quantify $\mu_a$ and $\mu_s'$.

We also have anatomical brain MRI images of each patient, and we computed the mean (standard deviation) skull/scalp/CSF thickness underneath our optical probe to

be 0.57 (0.13) cm. Because of the 2.5 cm source-detector separations used for both DOS and DCS, photons travel on average a depth of 1 to 1.25 cm into the tissue. Thus, we are confident the optical measurements are probing the surface of the cortex. However, in the future, DCS quantification of rCBF can be further improved. A semi-infinite model was used to fit DCS data. As known from the anatomical scans, such a model greatly simplifies the head geometry of these patients. In reality, the scalp, skull, cerebral spinal fluid, grey matter, and white matter possess different optical properties that can be accounted for, at least partially, in Monte Carlo simulations of light propagation [148, 150]. Nevertheless, the semi-infinite model has been demonstrated to provide a sufficient approximation of relative changes in cerebral blood flow (see Section 5.1).

#### *6.4.2.5 Summary/Conclusions- Hypercapnia*

We have quantified mean increases in cerebral blood flow and blood oxygenation during hypercapnia in infants with CHD, and we report significant correlations between measures of cerebral blood flow by DCS and cerebral oxygenation by DOS. Although $CO_2$ reactivity has been shown to correlate with adverse outcomes, our results suggest that $CO_2$ reactivity does not predict the presence of hypoxic-ischemic injury, albeit in a limited sample size. Given the current distribution of our data, we require approximately 17 additional patients with injury to determine a statistically significant difference between cerebrovascular reactivity in injured versus non-injured patients with 90% power. Thus, patient recruitment is ongoing. Nevertheless, these results do confirm that diffuse optical spectroscopy and diffuse correlation spectroscopy can provide valuable and individualized cerebral hemodynamic information in critically ill infants with CHD.

### 6.4.3 Sodium Bicarbonate

#### *6.4.3.1 Motivation - Sodium Bicarbonate*

Metabolic acidemia arises when the low systemic oxygen supply causes the brain to employ non-oxidative, anaerobic metabolic pathways, leading to the production of lactic acid. Severe acidemia (called acidosis) can cause increased pulmonary vascular resistance, decreased contractility of the heart muscle, and is associated with increased mortality [206, 207]. Sodium bicarbonate ($NaHCO_3$) is one of the most commonly used medications to treat metabolic acidemia in intensive care units that care for adults, children, and newborns alike. It treats metabolic acidemia by neutralizing excess acid in the blood and restoring normal tissue pH. Sodium bicarbonate reacts with the acid to yield water and carbon dioxide ($CO_2$):

$$\mathrm{H}^+ + HCO_3{}^- \leftrightarrow H_2CO_3 \leftrightarrow H_2O + CO_2. \qquad [79]$$

Sodium bicarbonate has been reported to increase systemic blood pressures as well as the arterial partial pressure of $CO_2$ (in ventilated infants) [208]. However, little is known about the effects of sodium bicarbonate on cerebral hemodynamics, and the efficacy of the treatment is widely debated [209, 210]. The few publications studying cerebral blood flow after administration of sodium bicarbonate report conflicting results [207, 208, 211-214]; Lou et al observed substantial *decreases* in cerebral blood flow measured by the $^{133}$Xe clearance technique five minutes after sodium bicarbonate administration in newborn infants with respiratory distress; Fanconi et al [208] observed significant increases in cerebral blood flow, inferred from increases in aortic flow velocity, due to sodium bicarbonate in newborn infants; and Young et al observed no change in

cerebral blood flow (measured with radioactive tracers) 30 minutes after drug administration in neonatal dogs. These apparent disparities are potentially due to the wide variety of patients studied as well as the time frame after drug administration that the effects were assessed.

Thus, the investigation described in this section aims to quantify the immediate cerebral hemodynamic effects due to rapid administration of sodium bicarbonate; the clinical study uses data collected on a subset of the pre-operative CHD patients discussed in Section 6.3. We hypothesize that sodium bicarbonate bolus will result in a rapid increase in brain $CO_2$, and thus it should have physiological effects that are similar to sudden hypercapnia, i.e., increasing cerebral blood flow and oxygenation.

#### *6.4.3.2 Data Analysis - Sodium Bicarbonate*

All data included in this analysis was acquired in the pre-operative period either prior to or immediately after the hypercapnia intervention performed in the MRI scanner (see Section 6.2.3). As seen in Figure 47, arterial blood gases taken prior to and immediately

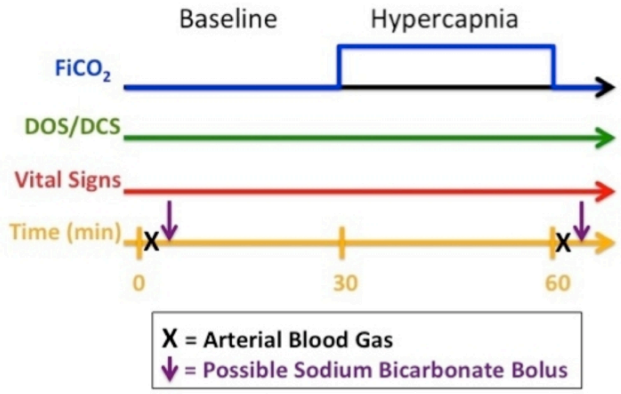


Figure 47, During the hypercapnia study protocol (see Section 6.2.3), arterial blood gases were drawn prior to and immediately after hypercapnia. A bolus of sodium bicarbonate was given to treat acidemia if indicated by the blood gas.

after the study revealed the need for sodium bicarbonate to treat acidemia. To quantify effects of sodium bicarbonate on cerebral hemodynamics, patients were monitored with DOS and DCS continuously at a rate of 0.3 Hz (see Section 6.2.3).

For DOS data analysis, we assumed the scattering coefficient does not change with the administration of sodium bicarbonate, and we further assumed that the changes in the absorption coefficient are small compared to the baseline absorption coefficient values. Thus, assuming these assumptions are valid, the modified Beer-Lambert (MBL) law can be employed for our analysis (see Section 2.1.5), i.e.

$$\log\left(\frac{I(t,\lambda)}{I_0(\lambda)}\right) = \Delta\mu_a(t,\lambda)L_{eff}(\lambda). \quad [80]$$

Here $I(t,\lambda)$ is the DC intensity of light at wavelength $\lambda$ and time $t$, $I_0(\lambda)$ is the mean DC intensity at wavelength $\lambda$ during the 2 minutes prior to sodium bicarbonate, and $\Delta\mu_a(t,\lambda)$ is the change in absorption coefficient at wavelength $\lambda$ and time $t$. To determine $L_{eff}(\lambda)$, baseline optical absorption and scattering properties were quantified in a subset of N=10 patients (see Sections 6.2.1 and 6.2.3). If absolute optical properties were not measured, a then mean $L_{eff}(\lambda)$ (calculated from the subset of CHD patients with absolute measures) was employed in our analysis.

For DCS data analysis, the correlation diffusion equation was solved analytically, for a sample geometry that was assumed homogeneous and semi-infinite. We used the semi-infinite solution (see Section 3.1) to fit our data for the tissue blood flow index (BFI). In the subset of patients for whom baseline $\mu_a$ and $\mu_s'$ were measured (see Section 6.2), these optical parameters (including the changes in $\mu_a$ computed with the MBL law) were input into the DCS fits. In those patients for whom baseline $\mu_a$ and $\mu_s'$ were not

measured, a mean baseline value from the measured subset of patients was employed along with the changes in $\mu_a$ computed with the MBL law, were input into the DCS fits

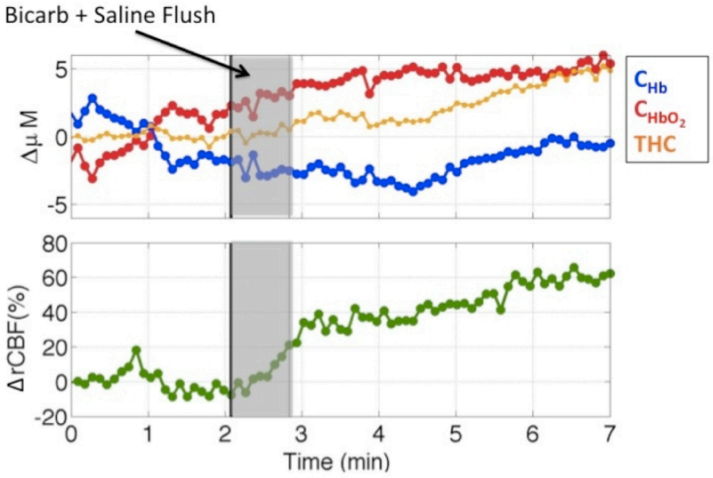


Figure 48, For quantification of the effects of rapid administration of a bolus of sodium bicarbonate, each hemodynamic parameter was averaged for 2 minutes before and two minutes after administration. Net changes were quantified either as a difference or ratio of pre- to post-sodium bicarbonate values.

(see Table 14).

Sample optical data is shown in Figure 48. For analysis, each parameter was averaged during a two-minute window prior to and immediately following sodium bicarbonate administration. A two-minute period was chosen because the effects of sodium bicarbonate are immediately evident, and because all patients had sufficient data within this window. Changes in each parameter were quantified using the following formulas:

$$\Delta Hb \equiv \langle C_{Bb} \rangle_{Post} - \langle C_{Hb} \rangle_{Pre},$$

$$\Delta HbO_2 \equiv \langle C_{BbO_2} \rangle_{Post} - \langle C_{HbO_2} \rangle_{Pre},$$

$$\Delta THC \equiv \langle THC \rangle_{Post} - \langle THC \rangle_{Pre},$$

$$\Delta rCBF \equiv (\langle BFI \rangle_{Post} / \langle BFI \rangle_{Pre} - 1) \times 100\%. \quad [81]$$

A Wilcoxon signed rank test was used to test if the median of each variable's distribution was significantly different from zero ($p<0.05$) [137].

#### *6.4.3.3 Results- Sodium Bicarbonate*

As noted previously, 28 neonates were monitored pre-operatively during the hypercapnia intervention performed in the MRI scanner. Of these 28 infants, 11 patients received sodium bicarbonate in the form of a rapid bolus administration followed by a flush of saline in an attempt to treat acidemia indicated by low arterial base excess

| Variable | Median (IQR) |
|---|---|
| Sex (M/F) | 8/3 |
| Cardiac Diagnosis (TGA/HLHS) | 2/9 |
| Gestation Age (weeks) | 38.8 (1.3) |
| Day of Life (days) | 3 (2) |
| Birth Weight (kg) | 3.15 (0.69) |
| Head Circumference (cm) | 33.7 (1.2) |
| Dosage $NaHCO_3$ (mEq/mg) | 1.12 (1.05) |

Table 16, Patient characteristics as well as dose of sodium bicarbonate (in milliequivalent per kilogram).

| **Variable** | **Median (IQR)** |
|---|---|
| pH | 7.3 (0.15) |
| $pCO_2$ (mmHg) | 43.5 (32.3) |
| $pO_2$ (mmHg) | 61 (10.3) |
| Bicarbonate ($HCO_3^-$) | 22 (4.5) |
| Base Excess (BE) | -4 (3.2) |

Table 17, Median (IQR) measures from arterial blood gas sample taken before administration of sodium bicarbonate (N=12 events).

(population median of -4, see Table 17). Twelve sodium bicarbonate events were captured, as one patient received sodium bicarbonate before and after the hypercapnia intervention. Demographics of the patients receiving sodium bicarbonate, along with median (IQR) dosage of sodium bicarbonate are summarized in Table 16. The majority of the patients were males with hypoplastic left heart syndrome. Patients received a median dose of sodium bicarbonate of 1.1 mEq/kg (ranging from 0.8 to 2.7 mEq/kg). Additionally, the results of arterial blood gases obtained prior to administration of sodium bicarbonate are summarized in Table 17.

As seen in Figure 49 and summarized in Table 18, sodium bicarbonate had little population-averaged effect on $\Delta C_{HbO_2}$, $\Delta C_{Hb}$, or $\Delta THC$. Changes in these parameters did not reach statistical significance. On the other hand, $\Delta rCBF$ increased significantly with sodium bicarbonate and weak correlation (R = 0.54, p = 0.11) was observed between changes in cerebral blood flow and sodium bicarbonate administered dosage (Figure

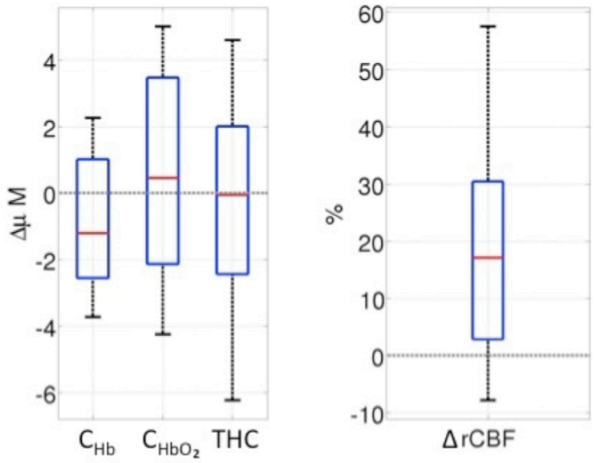


Figure 49, Boxplot summarizing the changes in deoxy-, oxy-, and total hemoglobin concentrations (left) and cerebral blood flow (right) due to sodium bicarbonate administration. Cerebral blood flow increased significantly.

50)[7]. Additionally, the correlation observed between changes in oxy-hemoglobin concentration and the dose of sodium bicarbonate was also significant (R = 0.80, p = 0.02). Correlations between dosage and $\Delta C_{Hb}$ and $\Delta THC$ did not attain statistical significance (p > 0.2).

| Variable | Median (IQR) | p-value |
|---|---|---|
| $\Delta rCBF$ (%) | 17.1 (24.6) | 0.009 |
| $\Delta C_{Hb}$(μM) | -1.2 (3.2) | 0.28 |
| $\Delta C_{HbO_2}$(μM) | 0.5 (4.9) | 0.63 |
| $\Delta THC$(μM) | -0.1 (4.1) | 0.70 |

Table 18, Median and interquartile range changes in the measured hemodynamic parameters. p-values were computed using a Wilcoxon signed rank test.

#### *6.4.3.4 Discussion- Sodium Bicarbonate*

In mechanically ventilated infants with congenital heart defects, sodium bicarbonate caused significant changes in cerebral blood flow immediately (within 2 minutes) following administration as measured by diffuse correlation spectroscopy. No significant changes in oxy- or deoxy-hemoglobin concentrations were observed in the patient population as a whole, although several individual patients did respond to sodium bicarbonate with either an increase or decrease in oxy-hemoglobin concentrations. The observed increase in cerebral blood flow may be due to $CO_2$, produced as a byproduct of sodium bicarbonate's reaction with lactic acid. As mentioned in Section 6.4.2, $CO_2$ is a potent vasodilator whose presence leads to the increases in cerebral blood flow. Interestingly, we did not observe a significant increase in total hemoglobin concentration over the entire population, an expected response to cerebrovascular vasodilation.

[7] The large error bars observed on some of the data points in this figure are due to the averaging window for analysis. When patients exhibit a substantial CBF response to sodium bicarbonate, the window encases the rise in CBF, thus leading to a large variation in the mean over the window.

Potentially we did not monitor long enough to see these expected increases.

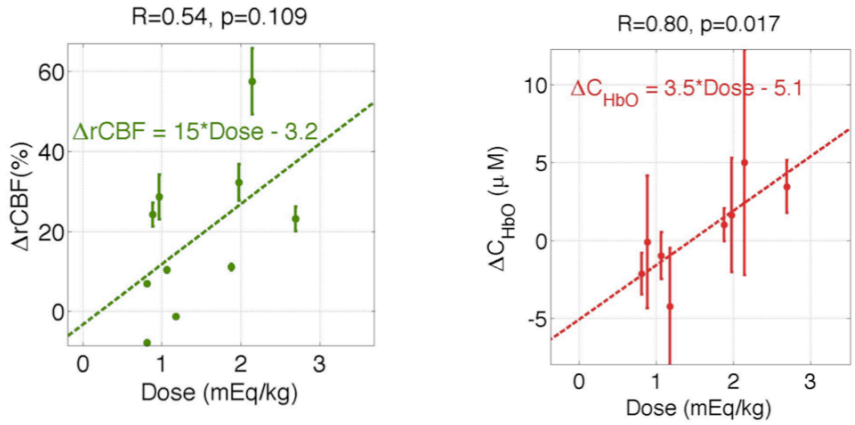


Figure 50, Relationship between the change in (Left) cerebral blood flow and (Right) oxy-hemoglobin concentration and the dose of sodium bicarbonate given.

Very little work has been published in human neonates on the effects of sodium bicarbonate to treat metabolic acidosis. Our results agree fairly well with a few reports of the cerebral hemodynamic effects of sodium bicarbonate used to correct metabolic acidosis. Van Alfen et al [207] employed NIRS and transcranial Doppler ultrasound (TCD) to study 15 preterm infants with metabolic acidosis treated with rapid administration of sodium bicarbonate. As was the case with our results, at five minutes post-sodium bicarbonate they did not observe changes in total hemoglobin concentration (they report cerebral blood volume), and, in contrast to our finding of a significant change in cerebral blood flow, they did not observe a significant change in cerebral blood flow velocity in the internal carotid artery. This discrepancy may be due to the fact that they were looking at macrovascular changes in flow velocity in a feeder artery, while DCS measures microvascular flow in cortical tissue. Alternatively, the discrepancy may arise from the fact that 9/15 of their population were not mechanically ventilated, allowing for respiratory compensation to exhale the extra $CO_2$ produced by sodium bicarbonate.

Lou et al [213] used the $^{133}Xe$ clearance technique to measure changes in cerebral blood flow five minutes after sodium bicarbonate injection in seven asphyxiated neonates with respiratory distress. They found profound *decreases* in cerebral blood flow in these infants, contrary to our findings. It is not clear why these results are contradictory; however, a possible explanation could be the difference in patient population. The neonates in their cohort were asphyxiated, while the patients in our population were not. Potentially, their brain injury was severe enough to deplete the cerebrovascular reserve, thus with the administration of sodium bicarbonate, vascular resistance is decreased in other tissues but constant in the brain, causing cerebral blood flow to decrease.

Faconi et al [208] monitored cardiac output and aortic blood flow velocity 1 and 5 minutes after a slow (~30 minutes) sodium bicarbonate infusion in 16 neonates who were paralyzed and mechanically ventilated. Although they did not measure cerebral blood flow directly, they did observe significant increases in cardiac output and aortic velocities at both 1 and 5 minutes, suggesting increases in cerebral blood flow (consistent with our findings). The researchers postulated that these aortic flow increases may be due to increases in the ability of the heart muscle to contract and decreases in the arterial tension against which the left ventricle must contract.

#### *6.4.3.5 Conclusions- Sodium Bicarbonate*

Sodium bicarbonate is one of the most commonly used medications in intensive care units that care for adults, children, and newborns alike. Infants with congenital heart defects often receive boluses of sodium bicarbonate in the pre-operative period to correct metabolic acidosis. We monitored cerebral blood flow and oxygenation changes

immediately after sodium bicarbonate administration. Cerebral blood flow was observed to increase significantly with sodium bicarbonate. These changes in cerebral blood flow were correlated (albeit somewhat weakly) with the given dose of sodium bicarbonate. On average oxy-hemoglobin concentration did not change with sodium bicarbonate administration, however changes in oxy-hemoglobin concentration were significantly correlated with dose.

Future work will benefit from extended monitoring to determine the potential transience of the cerebral blood flow response. We are in the process of recruiting more patients with the goal of increasing the statistical power of our analysis and extending monitoring time. Understanding the changes in cerebral hemodynamics that occur as a consequence of rapid infusions of sodium bicarbonate may have a significant impact in the treatment of metabolic acidemia in patients with CHD, as well as potentially in premature infants whose cerebrovascular bed is immature and poorly tolerates rapid fluctuations in CBF.

### 6.4.4 Blood transfusions

#### *6.4.4.1 Motivation- Blood Transfusions*

Critically-ill neonates often receive blood transfusions in order to maintain an adequate supply of oxygen to the tissue by increasing oxygen carrying capacity of the blood. In particular, many of the post-operative CHD patients are anemic due to hemodilution from cardiopulmonary bypass and substantial blood loss post-surgery. These patients receive transfusions in order to maintain adequate tissue oxygen supply to the tissue. Clinical indications for administering transfusion include hypotension,

tachycardia, and/or low hematocrit and hemoglobin values on arterial blood gases.

Although post-operative CHD patients frequently receive transfusions, little quantitative information is available about the cerebral effects of these transfusions. Some work has been done to monitor cerebral oxygen saturations ($ScO_2$), cerebral blood volume (CBV), and blood flow velocity in the large cerebral vessels during blood transfusions [215-222], but the majority of this work has been conducted on preterm infants, another critically ill neonatal population who frequently require transfusions. These investigations have found that tissue oxygen saturation increases due to increased oxygen carrying capacity of the blood. Additionally, these investigations have seen small but significant decreases in cerebral blood flow with transfusion, presumably due to increased arterial oxygen content and blood viscosity.

We have obtained pilot cerebral data due to transfusion using DOS/DCS in CHD patients with the ultimate goal of quantifying and better understanding the cerebral effects of blood transfusions in this particular population. Post-operatively, CHD patients with transposition of the great arteries have "healthy" circulation, since their condition is repairable. Thus, these patients are expected to respond in a similar manner to preterm infants to transfusion. However, CHD patients with hypoplastic left heart syndrome (HLHS) do not have normal circulation following palliative heart surgery. Despite this fact, we hypothesize that HLHS patients will still have a normal response to transfusion, i.e., an increase in cerebral oxygenation and decrease in cerebral blood flow will be observed in response to transfusion. The following sub-sections characterize the responses to transfusion and compare the effects between cardiac diagnoses. The reported results are the first observations about cerebral hemodynamic changes during

blood transfusions in CHD neonates.

#### *6.4.4.2 Data Analysis- Blood Transfusions*

All transfusion events included in this analysis were acquired in the post-operative period (see Section 6.2.4). Patients were monitored with DOS and DCS continuously ever 7.5 seconds, and vital signs were captured every 2 seconds. A researcher was at the bedside to mark the start and end of transfusion. Transfusions were excluded from analysis if the optical data was interrupted for probe repositioning, or if a significant physiological event (other than the transfusion itself) occurred during the transfusion, such as suctioning of the endotracheal tube, changes in ventilator settings, drug interventions causing changes in cerebral hemodynamics, etc.

For DOS data analysis, we assumed the scattering coefficient does not change with transfusion, and that the changes in the absorption coefficient are small compared to the baseline absorption coefficient values. Thus, the modified Beer-Lambert (MBL) law can be employed (see Section 2.1.5), i.e.

$$\log\left(\frac{I(t,\lambda)}{I_0(\lambda)}\right) = \Delta\mu_a(t,\lambda)L_{eff}(\lambda). \quad [82]$$

Here $I(t,\lambda)$ is the DC intensity of light at wavelength $\lambda$ and time $t$, $I_0(\lambda)$ is the mean DC intensity at wavelength $\lambda$ during the 2 minutes prior to transfusion, and $\Delta\mu_a(t,\lambda)$ is the change in absorption coefficient at wavelength $\lambda$ and time $t$ compared to at $t = 0$. To determine $L_{eff}(\lambda)$, baseline optical properties, i.e., absorption and reduced scattering coefficients, were quantified in a subset of N=10 patients (see Sections 6.2.1 and 6.2.3). If absolute optical properties were not measured, a mean $L_{eff}(\lambda)$ (calculated from the

subset of CHD patients with absolute measures) was employed.

For DCS data analysis, the correlation diffusion equation was solved analytically, assuming the sample geometry was assumed homogeneous and semi-infinite. We used the semi-infinite solution (see Section 3.1) to fit our data for a blood flow index (BFI). In the subset of patients for whom baseline $\mu_a$ and $\mu_s$' were measured (see Section 6.2), these values, along with the changes in $\mu_a$ computed with the MBL law, were input into the DCS fits. In those patients for whom baseline $\mu_a$ and $\mu_s$' were not measured, a mean value from the measured subset of patients was employed along with the changes in $\mu_a$ computed with the MBL law, were input into the DCS fits (see Table 14).

Sample optical and vital sign data obtained during transfusion is shown in Figure 51. For analysis, each parameter was averaged for a two-minute window prior to and

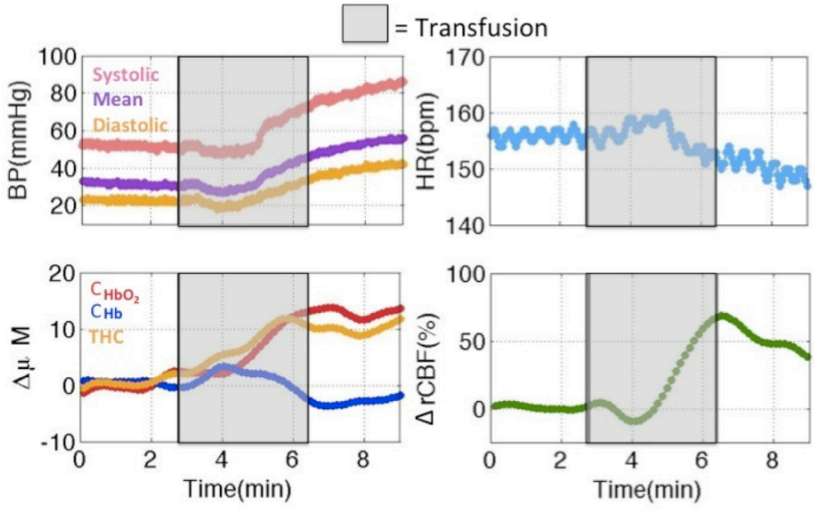


Figure 51, (Top Left) Arterial blood pressure, (Top Right) Heart rate, (Bottom Left) Changes in oxy-, deoxy-, and total hemoglobin concentrations (Bottom Right) changes in cerebral blood flow due to transfusion which is administered within the shaded region. For quantification of the effects of transfusion, each parameter was averaged for two minutes before and two minutes after administration. Net changes were quantified either as a difference or ratio of pre- to post-transfusion values.

immediately following transfusion. A two-minute period was chosen because all patients studied had sufficient data within this window. Changes in each parameter were quantified using the following formulas:

$$\Delta Hb \equiv \langle C_{Bb} \rangle_{Post} - \langle C_{Hb} \rangle_{Pre},$$

$$\Delta HbO_2 \equiv \langle C_{BbO_2} \rangle_{Post} - \langle C_{HbO_2} \rangle_{Pre},$$

$$\Delta THC \equiv \langle THC \rangle_{Post} - \langle THC \rangle_{Pre},$$

$$\Delta rCBF \equiv (\langle BFI \rangle_{Post} / \langle BFI \rangle_{Pre} - 1) \times 100\%. \quad [83]$$

For the purpose of this analysis, we considered each transfusion event to be an independent observation. A Wilcoxon signed rank test was used to test if the median of each variable's distribution was significantly different from zero ($p<0.05$) [137]. To test for association between the volume of blood given and the response of hemodynamic variables, a simple linear regression model was employed.

#### *6.4.4.3 Results- Blood Transfusions*

We have captured a total of 16 post-operative blood transfusions of varying duration and amount from 7 out of the 28 CHD patients we measured. Table 19 lists the patient characteristics of those who received transfusions. The median (interquartile range) duration of transfusion was 24.1 (34.5) minutes and median amount of transfusion was 25.3 (10.7) mL. Median (IQR) baseline hematocrit was 36 (3) % and baseline hemoglobin was 12.5 (2.38) g/dL, as determined by pre-transfusion arterial blood gas samples.

| | Median (IQR) |
|---|---|
| Diagnosis (HLHS/TGA) | N = 5/2 |
| Sex (Male/Female) | N = 4/3 |
| Gestation Age (weeks) | 38.9 (1.0) |
| Day of Life (days) | 3 (1.5) |
| Birth Weight (kg) | 3.15 (0.52) |
| Head Circumference (cm) | 33.4 (1.2) |

Table 19, Patient characteristics, reported as median and interquartile range (IQR), of those who received blood transfusions post-operatively.

As summarized in Table 21, transfusions induced significant increases (p=0.007) in mean arterial pressure. Figure 52 depicts a histogram of cerebral hemodynamic responses to transfusion. In this figure, a vertical dotted line indicates no change in the given parameter due to transfusion. Total hemoglobin concentration increased significantly with a median (interquartile range) increase of 9.5 (10.9) $\mu$M after transfusion (p=0.005). Oxy-hemoglobin concentration also increased with transfusion by 6.7 (9.9) $\mu$M (p=0.064). Transfusions had mixed effects on $rCBF$, leading to a non-significant (p = 0.21) population averaged change in CBF of 4.5 (24.5)%. Deoxy-hemoglobin concentration demonstrated a mild increase with transfusion that did not

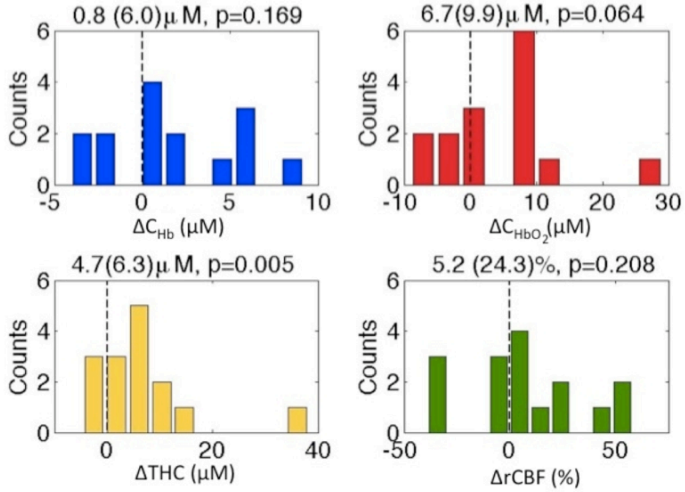


Figure 52, Distribution of changes in hemodynamic parameters caused to transfusion. Median (interquartile range) reported in the title of each subplot. The dotted vertical line indicates no change due to transfusion.

reach statistical significance (p > 0.17). Changes in all of these parameters did not significantly correlate (p > 0.1) with the amount of volume given (Table 20).

The cerebral hemodynamic effects of blood transfusions were then grouped by the cardiac diagnosis of the patient. As seen in Figure 53, Patients with TGA (N=5) showed a greater increase in $\Delta HbO_2$ after transfusion compared to those with a palliative repair of their CHD (HLHS, N=10). A similar trend was observed with changes in total hemoglobin concentration (p=0.075). No differences between the two groups were seen with either deoxy-hemoglobin concentration changes or relative changes in cerebral blood flow.

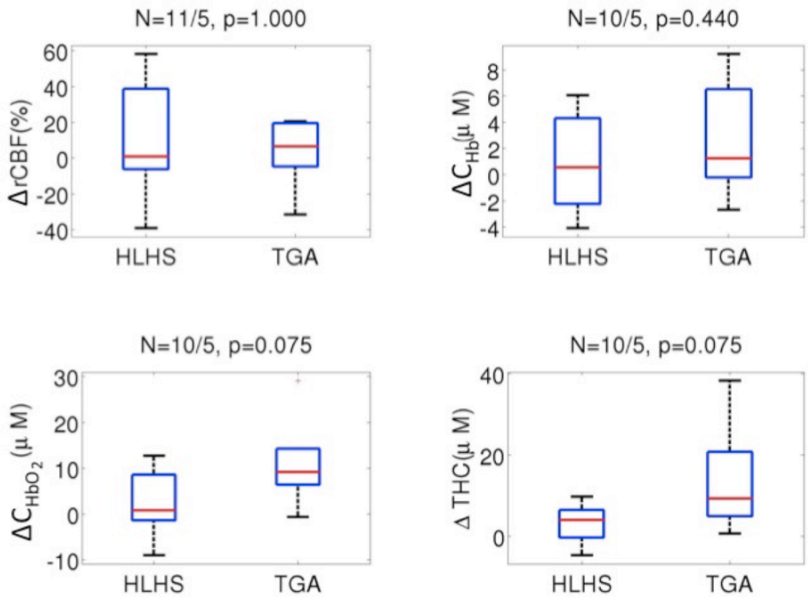


Figure 53, Differences between cardiac diagnosis in hemodynamic response to blood transfusion. From top left to bottom right: relative change in cerebral blood flow, change in deoxy-hemoglobin concentration, change in oxy-hemoglobin concentration, and change in total hemoglobin concentration. The title of each subplot indicates the number of events in each group and the p-value indicating differences between the medians of each group.

| | R (p-value) |
|---|---|
| $\Delta rCBF$ (%) | -0.39 (0.14) |
| $\Delta C_{Hb}$(μM) | 0.18 (0.52) |
| $\Delta C_{HbO_2}$(μM) | 0.16 (0.56) |
| $\Delta THC$(μM) | 0.22 (0.44) |

Table 20, Pearson's linear correlation coefficient (R) and corresponding p-value for the relationship between cerebral hemodynamic changes and the transfusion volume (cc/kg). Significant relations ($p < 0.05$) between changes in these parameters and transfusion amount were not observed.

| Variable | Median (IQR) | p-value |
|---|---|---|
| $\boldsymbol{\Delta rCBF}$ (%) | 5.2 (24.3) | 0.21 |
| $\boldsymbol{\Delta C_{Hb}}$(μM) | 0.8 (6.0) | 0.17 |
| $\boldsymbol{\Delta C_{HbO_2}}$(μM) | 6.7 (9.9) | 0.064 |
| $\boldsymbol{\Delta HR}$(bpm) | 1.5 (10.3) | 0.41 |
| $\boldsymbol{\Delta SpO_2}$(%) | -0.5 (2.8) | 0.88 |
| $\boldsymbol{\Delta MAP}$(mmHg) | 4.0 (5.4) | 0.007 |

Table 21, Median and interquartile range changes in the measured hemodynamic and vital sign parameters. p-values were computed using a Wilcoxon signed rank test.

#### *6.4.4.4 Discussion - Blood Transfusions*

These results demonstrate that blood transfusions in post-operative CHD patients aimed at improving the oxygen carrying capacity of the blood cause a wide-variety of hemodynamic responses. We observed significant population averaged increases in mean arterial pressure and total hemoglobin concentration. Oxy-hemoglobin concentrations also increased on average following transfusion, similar to observations by [215, 217, 218, 220] in preterm infants. Deoxy-hemoglobin concentration showed no significant population averaged changes.

On average, no alterations in cerebral blood flow were observed, however it should be noted that cerebral blood flow for some individual patients changed quite

dramatically with transfusion. In 3 patients, for example, CBF increased more than 50%, and in 3 other patients CBF decreased more than 30%. These results differ slightly from previously published work done on preterm infants using transcranial Doppler ultrasound in the pericallosal [217] and internal carotid [220] arteries. These groups found small but significant decreases in cerebral blood flow velocity (CBFV) in these large vessels following transfusion, potentially indicating a decrease in cerebral blood flow on the microvascular level as well. Additionally, it is believed that hematocrit and cerebral blood flow are anti-correlated [222]. Thus, our cerebral blood flow results are puzzling. Our CBF results may be explained by the fact that we are considering the two-minute window immediately following transfusion and not capturing the longer-term effects on CBF.

From this preliminary analysis, we did not find any predictive population-averaged variables of the cerebral hemodynamic changes to transfusion. Thus, in order for a clinician to determine the success or failure of a blood transfusion to improve oxygen content and delivery of blood in an individual patient, individualized bedside DOS and DCS monitoring is needed.

When grouped according to either palliative or corrective CHDs (HLHS or TGA, respectively), patients with “normal” circulation (TGA’s) showed a greater response in oxy-hemoglobin concentration to transfusion. Our work may lead to changes in clinical transfusion protocols for HLHS patients. If transfusions do not improve cerebral oxygenation, other preferred interventions exist, such as saline boluses or albumin infusions that would also have the desired effect of increasing blood pressure, but would not impose transfusion-related complications.

The main caveat of interpreting these results is that we did not explore the long-term (hours to days after transfusion) cerebral hemodynamic effects of transfusion. Our averaging window was chosen in order to avoid confounding factors that often occurred after transfusion, such as ventilator changes, medication delivery, or optical probe adjustments, that would affect the optical signal and/or brain dynamics. However, we do believe that our results, obtained immediately after transfusion, may still be indicative of long-term effects of transfusion, as other groups have observed oxygen saturations immediately after transfusion to be reflective of saturations 12 hours after transfusion [215].

*Optical data assumptions*

Due to limitations in the head size of the neonates we studied, we were restricted to a single source-detector separation for DOS measurements. Thus, the modified Beer-Lambert law was used to quantify changes in the absorption coefficient and thus changes in oxy- and deoxy-hemoglobin. However, many assumptions are required to employ the modified Beer-Lambert Law. In particular, it is assumed that $\Delta\mu_a$ is small relative to its baseline value, and we assume that $\mu_s'$ remains constant. These assumptions may not be valid in the present study since it is unknown whether the scattering properties of the tissue will change significantly with the presence of additional red blood cells. However, preliminary data obtained in our laboratory on piglets during transfusion (results not shown) indicate that the reduced scattering coefficient does indeed remain unchanged after transfusion. Additionally, depending on the patient, the absorption coefficient can change substantially (greater than 50%) with transfusion. Thus, future work would benefit greatly from the use of multiple source detector DOS

amplitude and phase measurements used to continuously quantify $\mu_a$ and $\mu_s'$.

To fit the DCS data for a blood flow index, we assumed initial values for the absorption and reduced scattering coefficients ($\mu_a$ and $\mu_s'$). Because we are only interested in relative changes in the BFI, our choice of initial $\mu_a$ and $\mu_s'$ has little to no effect on the resulting value of rCBF. However, changes from these initial values of $\mu_a$ and $\mu_s'$ that occur during the duration of the study may influence the magnitude of rCBF. Thus, we incorporated changes in $\mu_a$ obtained with DOS into our fitting procedure for BFI. However, as mentioned in the previous paragraph, our DOS analysis assumed that the scattering coefficient remained constant during the duration of the study. If this assumption is false, a 10% increase in the scattering coefficient could alter the magnitude of rCBF by approximately 20%. Again, future work would benefit from continuously quantifying $\mu_a$ and $\mu_s'$.

#### *6.4.4.5 Conclusions-Blood Transfusions*

These results are the first to investigate blood transfusions in CHD patients. We have observed significant increases in total hemoglobin concentrations with transfusions, with varying effects on cerebral blood flow in this population. Patient recruitment is ongoing in an attempt to recruit at least five more patients with each CHD diagnosis in order to achieve the desired statistical significance ($p < 0.05$, 90% power) for our population averaged response to blood transfusion.

We are currently investigating a neonatal piglet model of transfusion in order to have normative data to compare our CHD population results. Additionally, these animal studies will be used to further validate the optical techniques employed herein using both multi-separation diffusion theory and radiolabeled microspheres (to validate DOS and DCS, respectively). Once a

“normal” response to transfusion is established, albeit in a neonatal animal model, and the optical techniques have been well validated as reliable during transfusion, this data will be well received in the clinical community.

# 7 Conclusions/Future

Over the past few decades, significant advances have been made in improving the survival of premature neonates and neonates with congenital heart defects. With these advances in medical and surgical therapy, clinicians are now focusing their attention on reducing the morbidity associated with routine neonatal care. A major area of focus has been the greater understanding of the factors that contribute to impaired neurological development. Increasing our understanding of regulation of cerebral blood flow and the perturbations that occur during injury will allow us to further investigate the factors that contribute to central nervous system injury. These critically ill neonates would benefit greatly from continuous bedside monitoring of cerebral hemodynamics to identify, treat, and/or potentially prevent detrimental cerebral events such as hypoxic ischemia, hemorrhage, stroke, etc.

I believe that diffuse optical techniques (namely DOS and DCS) are well suited for this unique population. At a given source-detector separation, NIR light penetrates deeper into the neonatal cortex compared with adult cortex because of the decreased thickness of the neonatal skull. Therefore, neonates are ideal candidates for DOS/DCS monitoring. Conversely, DOS/DCS are particularly attractive tools for monitoring cerebral physiology in neonates because of their high temporal resolution, bedside capabilities, minimal deposition of energy, and its non-invasiveness. Additionally, DOS/DCS can easily be integrated with other monitoring techniques, such as MRI, transcranial Doppler ultrasound, electroencephalography, or positron emission tomography. Unlike some of these other modalities, namely MRI and positron emission tomography, DOS and DCS measurements are easily performed without the use of general anesthesia.

This dissertation focused on clinical data obtained with DOS and DCS in these neonates. As DCS is a relatively new technique, I demonstrate successful validation of both absolute DCS measures of blood flow index as well as relative changes in the blood flow index as a measure of cerebral blood flow in children. This validation is vital for further acceptance and integration of the technique into the clinical arena.

The last chapter (Chapter 6) highlights the translation of the DOS/DCS techniques to the intensive care unit for bedside monitoring. I focus on a collection of data obtained from infants with congenital heart defects. I demonstrate a progression of tissue oxygen saturation and cerebral blood volume (represented by total hemoglobin concentration) in the 12-hour period following cardiac surgery. Preliminary data suggests that prolonged periods of low tissue oxygen saturation may be indicative of brain injury. Additionally, chapter 6 quantifies the cerebral effects of various interventions, namely hypercapnia, blood transfusion, and sodium bicarbonate infusion. Patient recruitment for these studies is ongoing in order to increase our numbers and improve our statistics. We hope to get at least 20 more patients.

Our laboratory's collaborations with researchers at CHOP have grown by leaps and bounds in the four years that I have been working over there. In this past year alone our optics team has been approached to facilitate understanding of cerebral hemodynamics during anesthesia induction/maintenance, extracorporeal membrane oxygenation (ECMO, which is essentially a bedside cardiopulmonary bypass machine), pulmonary hypertension treatment, and blood transfusions in preterm infants.

In the near future, I envision DOS/DCS as a tool used primarily to study small subsets of pediatric patients to discover population-averaged patterns of cerebral

hemodynamic changes occurring with various clinical interventions, as well to gain insight into the predictors and risk factors for brain injury. However, due to the low cost and high information content of combining DOS and DCS, these techniques may become standard bedside care in many pediatric populations within the next 20 years. I quote this fairly long time frame because I believe there is still a substantial amount of work to be done for the techniques to gain widespread acceptance. The first major hurdle will be to establish a "user-friendly" interface for a hybrid DOS/DCS device that provides reliable real time data. The next hurdle will be to develop a way to obtain DCS signals through hair so that measurements can be made over regions other than the frontal cortex. Finally, we must fully understand the origin of the DCS signal in order to assess absolute cerebral blood flow (as opposed to just relative changes) and to isolate the contribution of the CBF signal that arises from the brain itself from that which arises from extracerebral layers.

The future looks bright for DOS and DCS monitoring in neonates. Unlike adult patients, much is still completely unknown about cerebral hemodynamics, brain injury, and subsequent neurodevelopment of infants. These optical techniques will help shed light on these unknowns, and may be the ideal cerebral monitor that is needed for these infants due to its non-invasive nature. Yet there is a mountain of development, education, exploration, and integration to be done, and this dissertation is just part of the beginning.

# 8 Bibliography


1. Martin, J.A., B.E. Hamilton, P.D. Sutton, S.J. Ventura, F. Menacker, S. Kirmeyer, and M.L. Munson, *Births: Final Data for 2005*, 2007, National Center for Health Statistics.

2. du Plessis, A.J. and J.J. Volpe, *Perinatal brain injury in the preterm and term newborn.* Current Opinion in Neurology, 2002. **15**: p. 151-7.

3. Perlman, J.M., *White matter injury in the preterm infant: an important determination of abnormal neurodevelopment outcome.* Early Hum Dev, 1998. **53**: p. 99-120.

4. Back, S.A., B.H. Han, N.L. Luo, C.A. Chricton, S. Xanthoudakis, J. Tam, K.L. Arvin, and D.M. Holtzman, *Selective Vulnerability of Late Oligodendrocyte Progenitors to Hypoxia-Ischemia.* J. Neurosci., 2002. **22**(2): p. 455-463.

5. Greisen, G., *Brain Monitoring in the Neonate-the Rationale.* Clinics in Perinatology, 2006. **33**(3).

6. *Improved National Prevalence Estimates for 18 Selected Major Birth Defects --- United States, 1999--2001*, in *Morbidity and Mortality Weekly Report*2005, Center for Disease Control. p. 1301-1305.

7. Bellinger, D.C., D. Wypij, A.J. duPlessis, L.A. Rappaport, R.A. Jonas, G. Wernovsky, and J.W. Newburger, *Neurodevelopmental status at eight years in children with dextro-transposition of the great arteries: The Boston Circulatory Arrest Trial.* Journal of Thoracic and Cardiovascular Surgery, 2003. **126**(5): p. 1385-1396.

8. Mahle, W.T., R.R. Clancy, E.M. Moss, M. Gerdes, D.R. Jobes, and G. Wernovsky, *Neurodevelopmental Outcome and Lifestyle Assessment in School-Aged and Adolescent Children With Hypoplastic Left Heart Syndrome.* Pediatrics, 2000. **105**(5): p. p1082 -

1089.

9. Majnemer, A., C. Limperopoulos, M. Shevell, B. Rosenblatt, C. Rohlicek, and C. Tchervenkov, *Long-term neuromotor outcome at school entry of infants with congenital heart defects requiring open-heart surgery.* Journal of Pediatrics, 2006. **148**(1): p. 72-77.

10. Wernovsky, G., A.J. Shillingford, and J.W. Gaynor, *Central nervous system outcomes in children with complex congenital heart disease.* Current Opinion in Cardiology, 2005. **20**(2): p. 94-99.

11. Wintermark, M., M. Sesay, E. Barbier, K. Borbely, W.P. Dillon, J.D. Eastwood, T.C. Glenn, C.B. Grandin, S. Pedraza, J.F. Soustiel, T. Nariai, G. Zaharchuk, J.M. Caille, V. Dousset, and H. Yonas, *Comparative overview of brain perfusion imaging techniques.* Stroke, 2005. **36**(9): p. E83-E99.

12. Huppi, P.S., S. Warfield, R. Kikinis, P.D. Barnes, G.P. Zientara, F.A. Jolesz, M.K. Tsuji, and J.J. Volpe, *Quantitative magnetic resonance imaging of brain development in premature and mature newborns.* Annals of Neurology, 1998. **43**(2): p. 224-235.

13. Kazemi, K., H.A. Moghaddam, R. Grebe, C. Gondry-Jouet, and F. Wallois, *A neonatal atlas template for spatial normalization of whole-brain magnetic resonance images of newborns: Preliminary results.* Neuroimage, 2007. **37**(2): p. 463-473.

14. Shi, F., Y. Fan, S.Y. Tang, J.H. Gilmore, W.L. Lin, and D.G. Shen, *Neonatal brain image segmentation in longitudinal MRI studies.* Neuroimage, 2010. **49**(1): p. 391-400.

15. Inder, T.E. and P.S. Huppi, *In vivo studies of brain development by magnetic resonance techniques.* Mental Retardation & Developmental Disabilities Research Reviews, 2000. **6**(1): p. 59-67.

16. Neil, J., J. Miller, P. Mukherjee, and P.S. Huppi, *Diffusion tensor imaging of normal and injured developing human brain - a technical review.* NMR in Biomedicine, 2002. **15**(7-8): p. 543-552.

17. Inder, T.E., P.S. Huppi, S. Warfield, R. Kikinis, G.P. Zientara, P.D. Barnes, F. Jolesz, and J.J. Volpe, *Periventricular white matter injury in the premature infant is followed by reduced cerebral cortical gray matter volume at term.* Annals of Neurology, 1999. **46**(5): p. 755-760.

18. Cha, S., *Dynamic Susceptibility-Weighted Contrast-Enhanced Perfusion MR Imaging in Pediatric Patients.* Neuroimaging Clinics of North America, 2006. **16**(1): p. 137-147.

19. Zierler, K.L., *Theoretical basis of indicator-dilution methods for measuring flow and volume.* Circulation Research, 1962. **10**(3): p. 393-&.

20. Goff, D.A., E.M. Buckley, T. Durduran, J. Wang, and D.J. Licht, *Noninvasive cerebral perfusion imaging in high-risk neonates.* Semin Perinatol, 2010. **34**(1): p. 46-56.

21. Wang, J. and D.J. Licht, *Pediatric perfusion MR imaging using arterial spin labeling.* Neuroimaging Clinics of North America, 2006. **16**(1): p. 149-+.

22. Wang, J.J., D.J. Licht, G.H. Jahng, C.S. Liu, J.T. Rubin, J. Haselgrove, R.A. Zimmerman, and J.A. Detre, *Pediatric perfusion imaging using pulsed arterial spin labeling.* Journal of Magnetic Resonance Imaging, 2003. **18**(4): p. 404-413.

23. Wang, J.J., D.J. Licht, D.W. Silvestre, and J.A. Detre, *Why perfusion in neonates with congenital heart defects is negative - Technical issues related to pulsed arterial spin labeling.* Magnetic Resonance Imaging, 2006. **24**(3): p. 249-254.

24. Greeley, W.J., R.M. Ungerleider, F.H. Kern, F.G. Brusino, L.R. Smith, and J.G. Reves,

*Effects of cardiopulmonary bypass on cerebral blood-flow in neonates, infants, and children.* Circulation, 1989. **80**(3): p. 209-215.

25. Greisen, G. and O. Pryds, *Low CBF, discontinuous EEG activity, and periventricular brain injury in ill, preterm neonates.* Brain & Development, 1989. **11**(3): p. 164-168.

26. Licht, D.J., J. Wang, D.W. Silvestre, S.C. Nicolson, L.M. Montenegro, G. Wernovsky, S. Tabbutt, S.M. Durning, D.M. Shera, J.W. Gaynor, T.L. Spray, R.R. Clancy, R.A. Zimmerman, and J.A. Detre, *Preoperative cerebral blood flow is diminished in neonates with severe congenital heart defects.* Journal of Thoracic and Cardiovascular Surgery, 2004. **128**(6): p. 841 - 849.

27. Miranda, M.J., K. Olofsson, and K. Sidaros, *Noninvasive measurements of regional cerebral perfusion in preterm and term neonates by magnetic resonance arterial spin labeling.* Pediatric Research, 2006. **60**(3): p. 359-363.

28. Biagi, L., A. Abbruzzese, M.C. Bianchi, D.C. Alsop, A. Del Guerra, and M. Tosetti, *Age dependence of cerebral perfusion assessed by magnetic resonance continuous arterial spin labeling.* Journal of Magnetic Resonance Imaging, 2007. **25**(4): p. 696-702.

29. Pollock, J.M., C.T. Whitlow, A.R. Deibler, H. Tan, J.H. Burdette, R.A. Kraft, and J.A. Maldjian, *Anoxic injury-associated cerebral hyperperfusion identified with arterial spin-labeled MR imaging.* American Journal of Neuroradiology, 2008. **29**(7): p. 1302-1307.

30. Chen, J., D.J. Licht, S.E. Smith, S.C. Agner, S. Mason, S.M. Wang, D.W. Silvestre, J.A. Detre, R.A. Zimmerman, R.N. Ichord, and J.J. Wang, *Arterial Spin Labeling Perfusion MRI in Pediatric Arterial Ischemic Stroke: Initial Experiences.* Journal of Magnetic Resonance Imaging, 2009. **29**(2): p. 282-290.

31. Evans, D.H. and W.N. McDicken, *Doppler Ultrasound: Physics, Instrumentation, and*

*Signal Processing*2000, New York, NY: John Wiley and Sons, Ltd.

32. Volpe, J.J., *Neurology of the Newborn*. 5th ed2008, Philadelphia: Elsevier.

33. Fenton, A.C., D.B. Shortland, E. Papathoma, D.H. Evans, and M.I. Levene, *Normal range for blood flow velocity in cerebral arteries of newly born term infants.* Early Human Development, 1990. **22**(2): p. 73-79.

34. Mires, G.J., N.B. Patel, J.S. Forsyth, and P.W. Howie, *Neonatal cerebral doppler flow velocity waveforms in the uncomplicated pre-term infant: reference values.* Early Human Development, 1994. **36**(3): p. 205-212.

35. Sonesson, S., P. Winberg, and B.P.W. Lundell, *Early Postnatal Changes in Intracranial Arterial Blood Flow Velocities in Term Infants.* Pediatric Research, 1987. **22**(4): p. 461-464.

36. Evans, N., M. Kluckow, M. Simmons, and D. Osborn, *Which to measure, systemic or organ blood flow? Middle cerebral artery and superior vena cava flow in very preterm infants.* Arch. Dis. Child. Fetal Neonatal Ed., 2002. **87**(3): p. F181-184.

37. Anthony, M.Y., D.H. Evans, and M.I. Levene, *Neonatal cerebral blood flow velocity responses to changes in posture.* Arch Dis Child, 1993. **69**(3 Spec No): p. 304-308.

38. Drayton, M.R. and R. Skidmore, *Vasoactivity of the major intracranial arteries in newborn infants.* Archives of Disease in Childhood, 1987. **62**(3): p. 236-240.

39. Kontos, H.A., *Validity of cerebral arterial blood flow calculations from velocity measurements.* Stroke, 1989. **20**(1): p. 1-3.

40. McBride, M.C., N. Laroia, and R. Guillet, *Electrographic seizures in neonates correlate with poor neurodevelopmental outcome.* Neurology, 2000. **55**(4): p. 506-513.

41. *Current Practice of Clinical Electroencephalography*. 3rd ed, ed. J.S. Ebersole and T.A. Pedley2002, Philadelphia: Lippincott Williams & Wilkins.

42. Watanabe, K., F. Hayakawa, and A. Okumura, *Neonatal EEG: a powerful tool in the assessment of brain damage in preterm infants.* Brain & Development, 1999. **21**(6): p. 361-372.

43. Frackowiak, R.S.J., G.-L. Lenzi, T. Jones, and J.D. Heather, *Quantitative Measurement of Regional Cerebral Blood Flow and Oxygen Metabolism in Man Using 15O and Positron Emission Tomography: Theory, Procedure, and Normal Values.* Journal of Computer Assisted Tomography, 1980. **4**(6): p. 727-736.

44. Raichle, M.E., W.R.W. Martin, P. Herscovitch, M.A. Mintun, and J. Markham, *Brain blood-flow measured with intravenous H2O-O15, II. Implementation and Validation.* Journal of Nuclear Medicine, 1983. **24**(9): p. 790-798.

45. Altman, D.I., J.M. Perlman, J.J. Volpe, and W.J. Powers, *Cerebral oxygen-metabolism in newborns.* Pediatrics, 1993. **92**(1): p. 99-104.

46. Altman, D.I. and J.J. Volpe, *Positron emission tomography in newborn-infants.* Clinics in Perinatology, 1991. **18**(3): p. 549-562.

47. Kusaka, T., S. Ijichi, Y. Yamamoto, and Y. Nishiyama, *Changes in cerebral glucose metabolism in newborn infants with cerebral infarction.* Pediatric Neurology, 2005. **32**(1): p. 46-49.

48. Shi, Y., R.B. Jin, J.N. Zhao, S.F. Tang, H.Q. Li, and T.Y. Li, *Brain positron emission tomography in preterm and term newborn infants.* Early Human Development, 2009. **85**(7): p. 429-432.

49. Obrist, W.D., H.K. Thompson, H.S. Wang, and W.E. Wilkinson, *Regional cerebral blood flow estimated by Xenon-133 inhalation.* Stroke, 1975. **6**(3): p. 245-256.

50. Hanson, M.A., J.A. Spencer, and C.H. Rodeck, eds. *Fetus and neonate: physiology and clinical applications. v.1 Circulation*. Vol. 1. 1993, Cambridge University Press: New York. 338-345.

51. Olesen, J., O.B. Paulson, and N.A. Lassen, *Regional Cerebral Blood Flow in Man Determined by the Initial Slope of the Clearance of Intra-arterially Injected l33Xe: Theory of the method, normal values, error of measurement, correction for remaining radioactivity, relation to other flow parameters, and response to PaCO2 changes.* Stroke, 1971. **2**(6): p. 519-540.

52. Younkin, D.P., M. Reivich, J. Jaggi, W. Obrist, and M. Delivoriapapadopoulos, *Noninvasive method of estimating human newborn regional cerebral blood flow.* Journal of Cerebral Blood Flow and Metabolism, 1982. **2**(4): p. 415-420.

53. Wolf, M., M. Ferrari, and V. Quaresima, *Progress of near-infrared spectroscopy and topography for brain and muscle clinical applications.* Journal of Biomedical Optics, 2007. **12**(6).

54. Brown, D., P. Picot, J. Naeini, R. Springett, D. Delpy, and T. Lee, *Quantitative near infrared spectroscopy measurement of cerebral hemodynamics in newborn piglets.* Pediatric Research, 2002. **51**(5): p. 564-570.

55. Schytz, H.W., T. Wienecke, L.T. Jensen, J. Selb, D.A. Boas, and M. Ashina, *Cerebral blood flow assessment with indocyanine green bolus transit detection by near-infrared spectroscopy before and after acetazolamide provocation in humans.* European Journal of Neurology, 2009. **16**(4): p. 461-467.

56. Arridge, S.R. and M. Schweiger, *A gradient-based optimisation scheme for optical tomography.* Opt. Express, 1998. **2**: p. 213.

57. Corlu, A., R. Choe, T. Durduran, K. Lee, M. Schweiger, E.M.C. Hillman, S.R. Arridge, and A.G. Yodh, *Diffuse optical tomography with spectral constraints and wavelength optimization.* Applied Optics, 2005. **44**: p. 2082-2093.

58. Buckley, E.M., N.M. Cook, T. Durduran, M.N. Kim, C. Zhou, R. Choe, G. Yu, S. Schultz, C.M. Sehgal, D.J. Licht, P.H. Arger, M.E. Putt, H.H. Hurt, and A.G. Yodh, *Cerebral hemodynamics in preterm infants during positional intervention measured with diffuse correlation spectroscopy and transcranial Doppler ultrasound.* Optics Express, 2009. **17**(15): p. 12571-81.

59. Durduran, T., C.A. Zhou, E.M. Buckley, M.N. Kim, G.Q. Yu, R. Choe, J.W. Gaynor, T.L. Spray, S.M. Durning, S.E. Mason, L.M. Montenegro, S.C. Nicolson, R.A. Zimmerman, M.E. Putt, J.J. Wang, J.H. Greenberg, J.A. Detre, A.G. Yodh, and D.J. Licht, *Optical measurement of cerebral hemodynamics and oxygen metabolism in neonates with congenital heart defects.* Journal of Biomedical Optics, 2010. **15**(3): p. 10.

60. Zhou, C., S.A. Eucker, T. Durduran, G. Yu, S.H. Friess, R. Ichord, S. Margulies, and A.G. Yodh., *Diffuse optical monitoring of hemodynamics in piglet brain with head trauma injury.* Journal of Biomedical Optics, 2009. **14**(3): p. 034015.

61. Cheung, C., J.P. Culver, K. Takahashi, J.H. Greenberg, and A.G. Yodh, *In vivo cerebrovascular measurement combining diffuse near-infrared absorption and correlation spectroscopies.* Physics In Medicine And Biology, 2001. **46**: p. 2053-2065.

62. Culver, J.P., T. Durduran, T. Furuya, C. Cheung, J.H. Greenberg, and A.G. Yodh, *Diffuse optical tomography of cerebral blood flow, oxygenation, and metabolism in rat during*

*focal ischemia.* Journal Of Cerebral Blood Flow And Metabolism, 2003. **23**: p. 911-924.

63. Durduran, T., G. Yu, M.G. Burnett, J.A. Detre, J.H. Greenberg, J. Wang, C. Zhou, and A.G. Yodh, *Diffuse optical measurement of blood flow, blood oxygenation, and metabolism in a human brain during sensorimotor cortex activation.* Optics Letters, 2004. **29**: p. 1766-1768.

64. Zhou, C., G. Yu, F. Daisuke, J.H. Greenberg, A.G. Yodh, and T. Durduran, *Diffuse optical correlation tomography of cerebral blood flow during cortical spreading depression in rat brain.* Optics Express, 2006. **14**: p. 1125-1144.

65. Kim, M.N., T. Durduran, S. Frangos, B.L. Edlow, E.M. Buckley, H.E. Moss, C. Zhou, G. Yu, R. Choe, E. Maloney-Wilensky, R.L. Wolf, M.S. Grady, J.H. Greenberg, J.M. Levine, A.G. Yodh, J.A. Detre, and W.A. Kofke, *Noninvasive measurement of cerebral blood blow and blood oxygenation using near-infrared and diffuse correlation spectroscopies in critically brain-injured adults.* Neurocritical Care, 2009.

66. Van Albada, M.P. and A. Lagendijk, *Observation of weak localization of light in a random medium.* Physical Review Letters, 1985. **55**(24): p. 2692-2695.

67. Haskell, R.C., L.O. Svaasand, T.-T. Tsay, T.-C. Feng, M.S. McAdams, and B.J. Tromberg, *Boundary conditions for the diffusion equation in radiative transfer.* JOSA-A, 1994. **11**(10): p. 2727-2741.

68. Durduran, T., R. Choe, W.B. Baker, and A.G. Yodh, *Diffuse optics for tissue monitoring and tomography.* Reports on Progress in Physics, 2010. **73**(7): p. 43.

69. Boas, D.A., *Diffuse Photon Probes of Structural and Dynamical Properties of Turbid Media: Theory and Biomedical Applications*, 1996, University of Pennsylvania.

70. Furutsu, K. and Y. Yamada, *Diffusion approximation for a dissipative random medium and the applications.* Phys. Rev. E, 1994. **50**(5): p. 3634-3640.

71. Ishimaru, A., *Wave Propagation and Scattering in Random Media*1978, New York: Wiley-IEEE Press.

72. Fishkin, J.B. and E. Gratton, *Propagation of photon-density waves in strongly scattering media containing an absorbing semi-infinite plane bounded by a straight edge.* J. Opt. Soc. Am. A, 1993. **10**(1): p. 127+.

73. Durduran, T., A.G. Yodh, B. Chance, and D.A. Boas, *Does the photon-diffusion coefficient depend on absorption?* Journal Of The Optical Society Of America A-Optics Image Science And Vision, 1997. **14**: p. 3358-3365.

74. Durian, D.J., *The diffusion coefficient depends on absorption.* Opt Lett, 1998. **23**(19): p. 1502-1504.

75. Duncan, A., J.H. Meek, M. Clemence, C.E. Elwell, L. Tyszczuk, M. Cope, and D. Delpy, *Optical pathlength measurements on adult head, calf and forearm and the head of the newborn infant using phase resolved optical spectroscopy.* Physics in Medicine and Biology, 1995. **40**(2): p. 295-304.

76. Patterson, M.S., B. Chance, and B.C. Wilson, *Time resolved reflectance and transmittance for the noninvasive measurement of tissue optical properties.* Applied Optics, 1989. **28**: p. 2331-2336.

77. Chance, B., M. Cope, E. Gratton, N. Ramanujam, and B. Tromberg, *Phase measurement of light absorption and scatter in human tissue.* Review of Scientific Instruments, 1998. **69**: p. 3457-3481.

78. Pham, T.H., O. Coquoz, J.B. Fishkin, E. Anderson, and B.J. Tromberg, *Broad bandwidth frequency domain instrument for quantitative tissue optical spectroscopy.* Review of Scientific Instruments, 2000. **71**(6): p. 2500-2513.

79. Fantini, S., M.A. Franceschini, J.S. Maier, S.A. Walker, B. Barbieri, and E. Gratton, *Frequency-domain multichannel optical-detector for noninvasive tissue spectroscopy and oximetry.* Optical Engineering, 1995. **34**(1): p. 32-42.

80. Gibson, A., J. Hebden, and S. Arridge, *Recent advances in diffuse optical imaging.* Physics in Medicine and Biology, 2005. **50**(4): p. R1-R43.

81. Boas, D.A., M.A. Oleary, B. Chance, and A.G. Yodh, *Scattering and Wavelength Transduction of Diffuse Photon Density Waves.* Phys. Rev. E, 1993. **47**(5): p. R2999-R3002.

82. O'Leary, M.A., *Imaging with Diffuse Photon Density Waves*, 1996, University of Pennsylvania.

83. Tromberg, B.J., L.O. Svaasand, T.-T. Tsay, and R.C. Haskell, *Properties of photon density waves in multiple-scattering media.* Appl. Opt., 1993. **32**(4): p. 607.

84. Walker, S.A., D.A. Boas, and E. Gratton, *Photon density waves scattered from cylindrical inhomogeneities: theory and experiments.* Applied Optics, 1998. **37**(10): p. 1935-1944.

85. Ripoll, J., V. Ntziachristos, R. Carminati, and M. Nieto-Vesperinas, *Kirchhoff approximation for diffusive waves.* Physical Review E, 2001. **64**(5).

86. Farrell, T.J., M.S. Patterson, and B. Wilson, *A diffusion theory model of spatially resolved, steady-state diffuse reflectance for the noninvasive determination of tissue optical properties in vivo.* Medical Physics, 1992. **19**(4): p. 879-888.

87. Schweiger, M., S.R. Arridge, M. Hiraoka, and D.T. Delpy, *The finite-element method for propagation of light in scattering media- Boundary and source conditions.* Medical Physics, 1995. **22**(11): p. 1779-1792.

88. Fantini, S., D. Hueber, M.A. Franceschini, E. Gratton, W. Rosenfeld, P.G. Stubblefield, D. Maulik, and M.R. Stankovic, *Non-invasive optical monitoring of the newborn piglet brain using continuous-wave and frequency-domain spectroscopy.* Physics in Medicine and Biology, 1999. **44**(6): p. 1543-1563.

89. Fantini, S., M.A. Franceschini, J.B. Fishkin, B. Barbieri, and E. Gratton, *Quantitative determination of the absorption spectra of chromophores in strongly scattering media- A light-emitting diode based technique.* Applied Optics, 1994. **33**(22): p. 5204-5213.

90. Arridge, S.R., M. Cope, and D.T. Delpy, *The theoretical basis for the determination of optical pathlengths in tissue: temporal and frequency analysis.* Physics in Medicine and Biology, 1992. **37**(7): p. 1531-1560.

91. Delpy, D.T., M. Cope, P. van der Zee, S. Arridge, S. Wray, and J. Wyatt, *Estimation of optical pathlength through tissue from direct time of flight measurement.* Physics in Medicine and Biology, 1988. **33**(12): p. 1433-1442.

92. Duncan, A., J.H. Meek, M. Clemence, C.E. Elwell, P. Fallon, L. Tyszczuk, M. Cope, and D.T. Delpy, *Measurement of Cranial Optical Path Length as a Function of Age Using Phase Resolved Near Infrared Spectroscopy.* Pediatric Research, 1996. **39**(5): p. 889-894.

93. van der Zee, P., M. Cope, S.R. Arridge, M. Essenpreis, L.A. Potter, A.D. Edwards, J.S. Wyatt, D.C. McCormick, S.C. Roth, and E.O. Reynolds, *Experimentally measured optical pathlengths for the adult head, calf and forearm and the head of the newborn infant as a*

*function of inter optode spacing.* Adv Exp Med Biol, 1992. **316**: p. 143-53.

94. Wyatt, J.S., M. Cope, D.T. Delpy, P. Vanderzee, S. Arridge, A.D. Edwards, and E.O.R. Reynolds, *Measurement of optical pathlength for cerebral near-infrared spectroscopy in newborn infants.* Developmental Neuroscience, 1990. **12**(2): p. 140-144.

95. Wyatt, J.S., M. Cope, D.T. Delpy, S. Wray, and E.O. Reynolds, *Quantification of cerebral oxygenation and haemodynamics in sick newborn infants by near infrared spectrophotometry.* Lancet, 1986. **2**(8515): p. 1063-1066.

96. Mourant, J.R., J.P. Freyer, A.H. Hielscher, A.A. Eick, D. Shen, and T.M. Johnson, *Mechanisms of light scattering from biological cells relevant to noninvasive optical-tissue diagnostics.* Applied Optics, 1998. **37**(16): p. 3586-3593.

97. Mourant, J.R., T. Fuselier, J. Boyer, T.M. Johnson, and I.J. Bigio, *Predictions and measurements of scattering and absorption over broad wavelength ranges in tissue phantoms.* Applied Optics, 1997. **36**(4): p. 949-957.

98. Nilsson, A.M.K., C. Sturesson, D.L. Liu, and S. Andersson-Engels, *Changes in spectral shape of tissue optical properties in conjunction with laser-induced thermotherapy.* Applied Optics, 1998. **37**(7): p. 1256-1267.

99. Franceschini, M.A., S. Thaker, G. Themelis, K.K. Krishnamoorthy, H. Bortfeld, S.G. Diamond, D.A. Boas, K. Arvin, and P.E. Grant, *Assessment of Infant Brain Development with Frequency-Domain Near-Infrared Spectroscopy.* Pediatric Research, 2007. **61**(5 Part 1): p. 546-551.

100. Zhao, J., H.S. Ding, X.L. Hou, C.L. Zhou, and B. Chance, *In vivo determination of the optical properties of infant brain using frequency-domain near-infrared spectroscopy.* Journal of Biomedical Optics, 2005. **10**(2): p. 024028.

101. Kohl, M., U. Lindauer, G. Royl, M. Kuhl, L. Gold, A. Villringer, and U. Dirnagl, *Physical model for the spectroscopic analysis of cortical intrinsic optical signals.* Physics in Medicine and Biology, 2000. **45**(12): p. 3749-3764.

102. Boas, D.A., L.E. Campbell, and A.G. Yodh, *Scattering and Imaging with Diffusing Temporal Field Correlations.* Physical Review Letters, 1995. **75**(9): p. 1855-1858.

103. Boas, D.A. and A.G. Yodh, *Spatially varying dynamical properties of turbid media probed with diffusing temporal light correlation.* Journal of the Optical Society America A, 1997. **14**(1): p. 192-215.

104. Maret, G. and P. Wolf, *Multiple light scattering from disordered media. The effect of brownian motion of scatterers.* Zeitschrift für Physik B Condensed Matter, 1987. **65**(4): p. 409-413.

105. Pine, D.J., D.A. Weitz, P.M. Chaikin, and E. Herbolzheimer, *Diffusing wave spectroscopy.* Physical Review Letters, 1988. **60**(12): p. 1134-1137.

106. Bonner, R. and R. Nossal, *Model for laser doppler measurements of blood flow in tissue.* Applied Optics, 1981. **20**(12): p. 2097-2107.

107. Ackerson, B.J., R.L. Dougherty, N.M. Reguigui, and U. Nobbman, *Correlation transfer - Application of radiative transfer solution methods to photon correlation problems.* Journal of Thermophysics and Heat Transfer, 1992. **6**(4): p. 577-588.

108. Sunar, U., H. Quon, T. Durduran, J. Zhang, J. Du, C. Zhou, G. Yu, R. Choe, A. Kilger, R. Lustig, L. Loevner, S. Nioka, B. Chance, and A.G. Yodh, *Noninvasive diffuse optical measurement of blood flow and blood oxygenation for monitoring radiation therapy in patients with head and neck tumors: a pilot study.* J Biomed Opt, 2006. **11**(6): p. 064021-064021.

109. McMahon, K.A., S.Y. Hiew, S. Hadjur, H. Veiga-Fernandes, U. Menzel, A.J. Price, D. Kioussis, O. Williams, and H.J. Brady, *Mll has a critical role in fetal and adult hematopoietic stem cell self-renewal.* Cell Stem Cell, 2007. **1**(3): p. 338-45.

110. Lemieux, P.A. and D.J. Durian, *Investigating non-Gaussian scattering processes by using nth-order intensity correlation functions.* J. Opt. Soc. Am. A, 1999. **16**(7): p. 1651-1664.

111. Zhou, C., *In-Vivo Optical Imaging and Spectroscopy of Cerebral Hemodynamics*, 2007, University of Pennsylvania.

112. Bandyopadhyay, R., A.S. Gittings, S.S. Suh, P.K. Dixon, and D.J. Durian, *Speckle-visibility spectroscopy: A tool to study time-varying dynamics.* Review of Scientific Instruments, 2005. **76**(9).

113. Einstein, A., *On the motion of small particles suspended in liquid at rest required by the molecular-kinetic theory of heat.* Annalen Der Physik, 1905. **17**: p. 549-560.

114. Zhou, C., R. Choe, N. Shah, T. Durduran, G. Yu, A. Durkin, D. Hsiang, R. Mehta, J. Butler, A. Cerussi, B.J. Tromberg, and A.G. Yodh, *Diffuse optical monitoring of blood flow and oxygenation in human breast cancer during early stages of neoadjuvant chemotherapy.* J Biomed Opt, 2007. **12**(5): p. 051903.

115. Durduran, T., *Non-Invasive Measurements of Tissue Hemodynamics with Hybrid Diffuse Optical Methods*, in *Physics and Astronomy*2004, University of Pennsylvania: Philadelphia.

116. Choe, R., *Diffuse Optical Tomography and Spectroscopy of Breast Cancer and Fetal Brain*, in *Physics and Astronomy*2005, University of Pennsylvania: Philadelphia.

117. Ramanujam, N., C. Du, H.Y. Ma, and B. Chance, *Sources of phase noise in homodyne*

*and heterodyne phase modulation devices used for tissue oximetry studies.* Review of Scientific Instruments, 1998. **69**(8): p. 3042-3054.

118. Benaron, D.A., C.D. Kurth, J.M. Steven, M. Delivoriapapadopoulos, and B. Chance, *Transcranial optical pathlength in infants by near-infrared phase shift spectroscopy*\. Journal of Clinical Monitoring, 1995. **11**(2): p. 109-117.

119. Bruce J. Berne, R.P., *Dynamic Light Scattering: With Applications to Chemistry, Biology, and Physics*2000: Courier Dover Publications.

120. Franceschini, M.-A., D.J. Wallace, B.B. Barbieri, S. Fantini, W.W. Mantulin, S. Pratesi, G.P. Donzelli, and E. Gratton. *Optical study of the skeletal muscle during exercise with a second-generation frequency-domain tissue oximeter*. 1997. SPIE.

121. Wallace, D.J., B. Michener, D. Choudhury, M. Levi, P. Fennelly, D.M. Hueber, and B.B. Barbieri. *Results of a 95-subject human clinical trial for the diagnosis of peripheral vascular disease using a near-infrared frequency domain hemoglobin spectrometer*. 1999. SPIE.

122. Yu, G.Q., T. Durduran, G. Lech, C. Zhou, B. Chance, R.E. Mohler, and A.G. Yodh, *Time-dependent blood flow and oxygenation in human skeletal muscles measured with noninvasive near-infrared diffuse optical spectroscopies.* Journal of Biomedical Optics, 2005. **10**: p. 024027-1-12.

123. Franceschini, M.-A., E. Gratton, D.M. Hueber, and S. Fantini. *Near-infrared absorption and scattering spectra of tissues in vivo*. 1999. SPIE.

124. Liem, K.D. and G. Greisen, *Monitoring of cerebral haemodynamics in newborn infants.* Early Human Development, 2010. **86**(3): p. 155-158.

125. Galli, K.K., R.A. Zimmerman, G.P. Jarvik, G. Wernovsky, M.K. Kuypers, R.R. Clancy, L.M. Montenegro, W.T. Mahle, M.F. Newman, A.M. Saunders, S.C. Nicolson, T.L. Spray, and J.W. Gaynor, *Periventricular leukomalacia is common after neonatal cardiac surgery.* Journal of Thoracic and Cardiovascular Surgery, 2004. **127**(3): p. 692 - 704.

126. Licht, D.J., D.M. Shera, R.R. Clancy, G. Wernovsky, L.M. Montenegro, S.C. Nicolson, R.A. Zimmerman, T.L. Spray, J.W. Gaynor, and A. Vossough, *Brain maturation is delayed in infants with complex congenital heart defects.* J Thorac Cardiovasc Surg, 2009. **137**(3): p. 529-537.

127. Andropoulos, D.B., J.V. Hunter, D.P. Nelson, S.A. Stayer, A.R. Stark, E.D. McKenzie, J.S. Heinle, D.E. Graves, and C.D. Fraser, *Brain immaturity is associated with brain injury before and after neonatal cardiac surgery with high-flow bypass and cerebral oxygenation monitoring.* Journal of Thoracic and Cardiovascular Surgery, 2010. **139**(3): p. 543-556.

128. Wilson, E.M., J.H. Halsey, JR., and J.J. Vitek, *Validation of Jugular Venous Flow as an Index of Total Cerebral Blood Flow.* Stroke, 1972. **3**(3): p. 300-321.

129. Meyer, J.S., S. Ishikawa, T.K. Lee, and A. Thal, *Quantitative measurement of cerebral blood flow with electromagnetic flowmeters: Recording internal jugular venous flow of monkey and man.* Trans Am Neurol Assoc, 1963. **88**: p. 78-83.

130. Bryant, D.J., J.A. Payne, D.N. Firmin, and D.B. Longmore, *Measurement of Flow with NMR Imaging Using a Gradient Pulse and Phase Difference Technique.* Journal of Computer Assisted Tomography, 1984. **8**(4): p. 588-593.

131. Dumoulin, C.L. and H.R. Hart, *Magnetic resonance angiography.* Radiology, 1986. **161**(3): p. 717-720.

132. Pelc, N.J., F.G. Sommer, K.C.P. Li, T.J. Brosnan, R.J. Herfkens, and D.R. Enzmann,

*Quantitative magnetic-resonance flow imaging.* Magnetic Resonance Quarterly, 1994. **10**(3): p. 125-147.

133. Fantini, S. and et al., *Non-invasive optical monitoring of the newborn piglet brain using continuous-wave and frequency-domain spectroscopy.* Physics in Medicine and Biology, 1999. **44**(6): p. 1543.

134. Zhao, J., H.S. Ding, X.L. Hou, C. Le Zhou, and B. Chance, *In vivo determination of the optical properties of infant brain using frequency-domain near-infrared spectroscopy.* Journal of Biomedical Optics, 2005. **10**(2): p. 7.

135. Boas, D.A., M.A. OLeary, B. Chance, and A.G. Yodh, *Detection and characterization of optical inhomogeneities with diffuse photon density waves: A signal-to-noise analysis.* Applied Optics, 1997. **36**(1): p. 75-92.

136. Dietsche, G., M. Ninck, C. Ortolf, J. Li, F. Jaillon, and T. Gisler, *Fiber-based multispeckle detection for time-resolved diffusing-wave spectroscopy: characterization and application to blood flow detection in deep tissue.* Appl. Opt., 2007. **46**(35): p. 8506-8514.

137. Wilcoxon, F., *Individual Comparisons by Ranking Methods.* Biometrics Bulletin, 1945. **1**(6): p. 80-83.

138. R Development Core Team, *R: A Language and Environment for Statistical Computing*, 2011, R Foundation for Statistical Computing.

139. Lin, L.I., *A Concordance Correlation-Coefficient to Evaluate Reproducibility.* Biometrics, 1989. **45**(1): p. 255-268.

140. Ito, H., I. Kanno, M. Ibaraki, J. Hatazawa, and S. Miura, *Changes in human cerebral blood flow and cerebral blood volume during hypercapnia and hypocapnia measured by*

*positron emission tomography.* Journal of Cerebral Blood Flow and Metabolism, 2003. **23**(6): p. 665-670.

141. Rostrup, E., I. Law, M. Blinkenberg, H.B.W. Larsson, A.P. Born, S. Holm, and O.B. Paulson, *Regional differences in the CBF and BOLD responses to hypercapnia: A combined PET and fMRI study.* Neuroimage, 2000. **11**(2): p. 87-97.

142. Tabbutt, S., C. Ramamoorthy, L.M. Montenegro, S.M. Durning, C.D. Kurth, J.M. Steven, R.I. Godinez, T.L. Spray, G. Wernovsky, and S.C. Nicolson, *Impact of inspired gas mixtures on preoperative infants with hypoplastic left heart syndrome during controlled ventilation.* Circulation, 2001. **104**(12): p. I159-I164.

143. Ramamoorthy, C., S. Tabbutt, C.D. Kurth, J.M. Steven, L.M. Montenegro, S. Durning, G. Wernovsky, J.W. Gaynor, T.L. Spray, and S.C. Nicolson, *Effects of inspired hypoxic and hypercapnic gas mixtures on cerebral oxygen saturation in neonates with univentricular heart defects.* Anesthesiology, 2002. **96**(2): p. 283-288.

144. Toiyama, K., K. Hamaoka, T. Oka, N. Kobayashi, K. Noritake, R. Kato, Y. Kawai, S. Ozawa, M. Nishida, and T. Itoi, *Changes in Cerebral Oxygen Saturation and Blood Flow During Hypoxic Gas Ventilation Therapy in HLHS and CoA/IAA Complex With Markedly Increased Pulmonary Blood Flow.* Circulation Journal, 2010. **74**(10): p. 2125-2131.

145. Fogel, M.A., S. Durning, G. Wernovsky, A.N. Pollock, J.W. Gaynor, and S. Nicolson, *Brain versus lung: Hierarchy of feedback loops in single-ventricle patients with superior cavopulmonary connection.* Circulation, 2004. **110**(11): p. II147-II152.

146. Mesquita, R.C., N. Skuli, M.N. Kim, J. Liang, S. Schenkel, A.J. Majmundar, M.C. Simon, and A.G. Yodh, *Hemodynamic and metabolic diffuse optical monitoring in a mouse model of hindlimb ischemia.* Biomed. Opt. Express, 2010. **1**(4): p. 1173-1187.

147. Diop, M., *Email Correspondence*, E. Buckley, Editor 2011.

148. Wang, L.H., S.L. Jacques, and L.Q. Zheng, *MCML - Monte Carlo modeling of light transport in multilayered tissues.* Computer Methods and Programs in Biomedicine, 1995. **47**(2): p. 131-146.

149. Gagnon, L., M.e. Desjardins, J. Jehanne-Lacasse, L. Bherer, and F.e.e. Lesage, *Investigation of diffuse correlation spectroscopy in multi-layered media including the human head.* Opt. Express, 2008. **16**(20): p. 15514-15530.

150. Boas, D., J. Culver, J. Stott, and A. Dunn, *Three dimensional Monte Carlo code for photon migration through complex heterogeneous media including the adult human head.* Opt. Express, 2002. **10**(3): p. 159-170.

151. Allen, M.C., *Neurodevelopmental outcomes of preterm infants.* Curr Opin Neurol, 2008. **21**(2): p. 123-128.

152. Romagnoli, C., C. Giannantonio, M. De Carolis, F. Gallini, E. Zecca, and P. Papacci, *Neonatal color Doppler US study: Normal values of cerebral blood flow velocities in preterm infants in the first month of life.* Ultrasound in Medicine and Biology, 2006. **32**: p. 321-331.

153. Yodh, A.G. and B. Chance, *Spectroscopy and Imaging with Diffusing Light.* Physics Today, 1995: p. 34-40.

154. Wolfberg, A.J. and A.J. du Plessis, *Near-infrared spectroscopy in the fetus and neonate.* Clin Perinatol, 2006. **33**(3): p. 707-728.

155. Edwards, A.D., C. Richardson, M. Cope, J.S. Wyatt, D.T. Delpy, and E.O.R. Reynolds, *Cotside measurement of cerebral bood flow in ill newborn infants by near-infrared*

*spectroscopy.* The Lancet, 1988. **2**(8614): p. 770-771.

156. Finley, J.P., R. Hamilton, and M.G. MacKenzie, *Heart rate response to tilting in newborns in quiet and active sleep.* Biol Neonate, 1984. **45**(1): p. 1-10.

157. Lagercrantz, H., D. Edwards, D. Hendersonsmart, T. Hertzberg, and H. Jeffery, *Autonomic Reflexes in Preterm Infants.* Acta Paediatrica Scandinavica, 1990. **79**: p. 721-728.

158. Dellagrammaticas, H.D., J. Kapetanakis, M. Papadimitriou, and G. Kourakis, *Effect of body tilting on physiological functions in stable very low birthweight neonates.* Arch Dis Child, 1991. **66**(4 Spec No): p. 429-432.

159. Gronlund, J., J. Jalonen, and I. Valimaki, *Transcephalic electrical impedance provides a means for quantifying pulsatile cerebral blood volume changes following head-up tilt.* Early Hum Dev, 1997. **47**: p. 11-18.

160. Panerai, R.B., A. Wilfred, R. Kelsall, J. Rennie, and D. Evans, *Cerebral Autoregulation Dynamics in Premature Newborns.* Stroke, 1995. **26**: p. 74-80.

161. Pichler, G., B. Urlesberger, G. Schmölzer, and W. Müller, *Effect of tilting on cerebral haemodynamics in preterm infants with periventricular leucencephalomalacia.* Acta Paediatr, 2004. **93**(1): p. 70-75.

162. Pichler, G., M.C. van Boetzelar, W. Müller, and B. Urlesberger, *Effect of tilting on cerebral hemodynamics in preterm and term infants.* Biol Neonate, 2001. **80**(3): p. 179-185.

163. Schrod, L. and J. Walter, *Effect of head-up body tilt position on autonomic function and cerebral oxygenation in preterm infants.* Biol Neonate, 2002. **81**(4): p. 255-259.

164. Urlesberger, B., W. Muller, E. Ritschl, and F. Reiterer, *The influence of head position on*

*the intracranial pressure in preterm infants with posthemorrhagic hydrocephalus.* Childs Nervous System, 1991. **7**(2): p. 85-87.

165. Brown, W., *Dynamic Light Scattering: The Method and Some Applications*1993: Oxford University Press.

166. Hebden, J. and T. Austin, *Optical tomography of the neonatal brain.* European Radiology, 2007. **17**(11): p. 2926-2933.

167. Hebden, J.C., A. Gibson, R.M. Yusof, N. Everdell, E.M.C. Hillman, D.T. Delpy, S.R. Arridge, T. Austin, J.H. Meek, and J.S. Wyatt, *Three-dimensional optical tomography of the premature infant brain.* Physics in Medicine and Biology, 2002. **47**(23): p. 4155-4166.

168. Spearman, C., *The proof and measurement of association between two things. By C. Spearman, 1904.* The American journal of psychology, 1987. **100**(3-4): p. 441-471.

169. Hochberg, Y., *A sharper Bonferroni procedure for multiple tests of significance.* Biometrika, 1988. **75**(4): p. 800-802.

170. Li, J., G. Dietsche, D. Iftime, S.E. Skipetrov, G. Maret, T. Elbert, B. Rockstroh, and T. Gisler, *Noninvasive detection of functional brain activity with near-infrared diffusing-wave spectroscopy.* Journal of Biomedical Optics, 2005. **10**(4).

171. Ijichi, S., T. Kusaka, K. Isobe, K. Okubo, K. Kawada, M. Namba, H. Okada, T. Nishida, T. Imai, and S. Itoh, *Developmental Changes of Optical Properties in Neonates Determined by Near-Infrared Time-Resolved Spectroscopy.* Pediatric Research, 2005. **58**(3): p. 568-573.

172. Cheung, R., M. Solonenko, T.M. Busch, F. Del Piero, M.E. Putt, S.M. Hahn, and A.G. Yodh, *Correlation of in vivo photosensitizer fluorescence and photodynamic-therapy-*

*induced depth of necrosis in a murine tumor model.* Journal Of Biomedical Optics, 2003. **8**: p. 248-252.

173. Miller, S.P. and P.S. McQuillen, *Neurology of congenital heart disease: insight from brain imaging.* Arch. Dis. Child. Fetal Neonatal Ed., 2007. **92**(6): p. F435-437.

174. Dent, C.L., J.P. Spaeth, B.V. Jones, S.M. Schwartz, T.A. Glauser, B. Hallinan, J.M. Pearl, P.R. Khoury, and C.D. Kurth, *Brain magnetic resonance imaging abnormalities after the Norwood procedure using regional cerebral perfusion.* Journal of Thoracic and Cardiovascular Surgery, 2006. **131**(1): p. 190-197.

175. Ichord, R., R.R. Clancy, G.P. Jarvik, T.L. Spray, S. Nicolson, S. Tabbutt, G. Wernovsky, R. Zimmerman, and J.W. Gaynor, *Perioperative stroke is clinically silent in infants undergoing open heart surgery for complex congenital heart disease.* Stroke, 2004. **35**(1): p. 264-264.

176. Rappaport, L.A., D. Wypij, D.C. Bellinger, S.L. Helmers, G.L. Holmes, P.D. Barnes, G. Wernovsky, K.C.K. Kuban, R.A. Jonas, J.W. Newburger, and G. Boston Circulatory Arrest Study, *Relation of seizures after cardiac surgery in early infancy to neurodevelopmental outcome.* Circulation, 1998. **97**(8): p. 773-779.

177. Volpe, J.J., *Neurobiology of periventricular leukomalacia in the premature infant.* Pediatr Res, 2001. **50**(5): p. 553-562.

178. Volpe, J.J., *Cerebral White Matter Injury of the Premature Infant--More Common Than You Think.* Pediatrics, 2003. **112**(1): p. 176.

179. Mahle, W.T., F. Tavani, R.A. Zimmerman, S.C. Nicolson, K.K. Galli, J.W. Gaynor, R.R. Clancy, L.M. Montenegro, T.L. Spray, R.M. Chiavacci, G. Wernovsky, and C.D. Kurth, *An MRI study of neurological injury before and after congenital heart surgery.* Circulation,

2002. **106**(90121): p. I-109-114.

180. McQuillen, P.S., A.J. Barkovich, S.E.G. Hamrick, M. Perez, P. Ward, D.V. Glidden, A. Azakie, T. Karl, and S.P. Miller, *Temporal and anatomic risk profile of brain injury with neonatal repair of congenital heart defects.* Stroke, 2007. **38**(2): p. 736-741.

181. McQuillen, P.S., S.E.G. Hamrick, M.J. Perez, A.J. Barkovich, D.V. Glidden, T.R. Karl, D. Teitel, and S.P. Miller, *Balloon atrial septostomy is associated with preoperative stroke in neonates with transposition of the great arteries.* Circulation, 2006. **113**(2): p. 280-285.

182. Petit, C.J., J.J. Rome, G. Wernovsky, S.E. Mason, D.M. Shera, S.C. Nicolson, L.M. Montenegro, S. Tabbutt, R.A. Zimmerman, and D.J. Licht, *Preoperative Brain Injury in Transposition of the Great Arteries Is Associated With Oxygenation and Time to Surgery, Not Balloon Atrial Septostomy.* Circulation, 2009. **119**(5): p. 709-716.

183. Marelli, A.J., A.S. Mackie, R. Ionescu-Ittu, E. Rahme, and L. Pilote, *Congenital Heart Disease in the General Population: Changing Prevalence and Age Distribution.* Circulation, 2007. **115**(2): p. 163-172.

184. Schlant, R.C. and R.W. Alexander, eds. *Hurst's the Heart: Arteries and Veins*. 8th ed. 1995, McGraw-Hill: New York. 538.

185. Anderson, R.H.B., Edward J; Penny, Daniel J; Redington, Andrew N; Rigby, Michael L; Wernovsky, Gil, ed. *Pediatric Cardiology*. 3 ed. 2010, Churchill Livingstone: Philadelphia, PA.

186. Wolthuis, R., M. van Aken, K. Fountas, J.S. Robinson, H.A. Bruining, and G.J. Puppels, *Determination of water concentration in brain tissue by Raman spectroscopy.* Analytical Chemistry, 2001. **73**(16): p. 3915-3920.

187. Fenton, K.N., K. Freeman, K. Glogowski, S. Fogg, and K.F. Duncan, *The significance of baseline cerebral oxygen saturation in children undergoing congenital heart surgery.* American Journal of Surgery, 2005. **190**(2): p. 260-263.

188. Hoffman, G.M., E.A. Stuth, R.D. Jaquiss, P.L. Vanderwal, S.R. Staudt, T.J. Troshynski, N.S. Ghanayem, and J.S. Tweddell, *Changes in cerebral and somatic oxygenation during stage 1 palliation of hypoplastic left heart syndrome using continuous regional cerebral perfusion.* Journal of Thoracic and Cardiovascular Surgery, 2004. **127**(1): p. 223-233.

189. Li, J., G.C. Zhang, B.W. McCrindle, H. Holtby, T. Humpl, S. Cai, C.A. Caldarone, A.N. Redington, and G.S. Van Arsdell, *Profiles of hemodynamics and oxygen transport derived by using continuous measured oxygen consumption after the Norwood procedure.* Journal of Thoracic and Cardiovascular Surgery, 2007. **133**(2): p. 441-U39.

190. Pesonen, E.J., K.I. Peltola, R.E. Korpela, H.I. Sairanen, M.A. Leijala, K.O. Raivio, and S.H.M. Andersson, *Delayed impairment of cerebral oxygenation after deep hypothermic circulatory arrest in children.* Annals of Thoracic Surgery, 1999. **67**(6): p. 1765-1770.

191. Phelps, H.M., W.T. Mahle, D. Kim, J.M. Simsic, P.M. Kirshbom, K.R. Kanter, K.O. Maher, and D.M. Overman, *Postoperative Cerebral Oxygenation in Hypoplastic Left Heart Syndrome After the Norwood Procedure.* Annals of Thoracic Surgery, 2009. **87**(5): p. 1490-1494.

192. Hoffman, G.M., N.S. Ghanayem, J.M. Kampine, S. Berger, K.A. Mussatto, S.B. Litwin, and J.S. Tweddell, *Venous saturation and the anaerobic threshold in neonates after the Norwood procedure for hypoplastic left heart syndrome.* Annals of Thoracic Surgery, 2000. **70**(5): p. 1515-1520.

193. Tweddell, J.S., N.S. Ghanayem, K.A. Mussatto, M.E. Mitchell, L.J. Lamers, N.L. Musa, S.

Berger, S.B. Litwin, and G.M. Hoffman, *Mixed venous oxygen saturation monitoring after stage 1 palliation for hypoplastic left heart syndrome.* Annals of Thoracic Surgery, 2007. **84**(4): p. 1301-1311.

194. Roche, N., *Email Correspondence*, E. Buckley, Editor 2011.

195. Svaasand, L.O. and R. Ellingsen, *Optical properties of human brain* Photochemistry and Photobiology, 1983. **38**(3): p. 293-299.

196. Miller, S.P., P.S. McQuillen, S. Hamrick, D. Xu, D.V. Glidden, N. Charlton, T. Karl, A. Azakie, D.M. Ferriero, A.J. Barkovich, and D.B. Vigneron, *Abnormal brain development in newborns with congenital heart disease.* New England Journal of Medicine, 2007. **357**(19): p. 1928-1938.

197. Franceschini, M.A., S. Fantini, L.A. Paunescu, J.S. Maier, and E. Gratton, *Influence of a Superficial Layer in the Quantitative Spectroscopic Study of Strongly Scattering Media.* Appl. Opt., 1998. **37**(31): p. 7447-7458.

198. Roche-Labarbe, N., S.A. Carp, A. Surova, M. Patel, D.A. Boas, R.E. Grant, and M.A. Franceschini, *Noninvasive Optical Measures of CBV, StO(2), CBF Index, and rCMRO(2) in Human Premature Neonates' Brains in the First Six Weeks of Life.* Human Brain Mapping, 2010. **31**(3): p. 341-352.

199. Lassen, N.A., *Cerebral blood flow and oxygen consumption in man.* Physiological Reviews, 1959. **39**(2): p. 183-238.

200. Lassen, N.A., *Control of cerebral circulation in health and disease.* Circulation Research, 1974. **34**(6): p. 749-760.

201. Ashwal, S., R.M. Perkin, J.R. Thompson, L.G. Tomasi, D. Vanstralen, and S. Schneider,

*CBF and CBF pCO2 reactivity in childhood strangulation.* Pediatric Neurology, 1991. **7**(5): p. 369-374.

202. Ashwal, S., W. Stringer, L. Tomasi, S. Schneider, J. Thompson, and R. Perkin, *Cerebral blood flow and carbon dioxide reactivity in children with bacterial meningitis.* Journal of Pediatrics, 1990. **117**(4): p. 523-530.

203. Pryds, O., G. Greisen, L.L. Skov, and B. Friishansen, *Carbon dioxide related changes in cerebral blood volume and cerebral blood flow in mechanically ventilated preterm neonates- Comparison of near-infrared spectrophotometry and Xe-133 clearance.* Pediatric Research, 1990. **27**(5): p. 445-449.

204. Grubb, R.L., M.E. Raichle, J.O. Eichling, and Terpogos.Mm, *Effects of changes in PaCO2 on cerebral blood volume, blood flow, and vascular mean transit time.* Stroke, 1974. **5**(5): p. 630-639.

205. Boas, D.A. and S.J. Payne, *Comment on 'Estimating a modified Grubb's exponent in healthy human brains with near infrared spectroscopy and transcranial Doppler'.* Physiological Measurement, 2009. **30**(10): p. L9-L11.

206. Forsythe, S.M. and G.A. Schmidt, *Sodium bicarbonate for the treatment of lactic acidosis.* Chest, 2000. **117**(1): p. 260-267.

207. van Alfen-van der Velden, A., J.C.W. Hopman, J. Klaessen, T. Feuth, R.C.A. Sengers, and K.D. Liem, *Effects of rapid versus slow infusion of sodium bicarbonate on cerebral hemodynamics and oxygenation in preterm infants.* Biology of the Neonate, 2006. **90**(2): p. 122-127.

208. Fanconi, S., R. Burger, D. Ghelfi, J. Uehlinger, and U. Arbenz, *Hemodynamic effects of sodium bicarbonate in critically ill neonates.* Intensive Care Medicine, 1993. **19**(2): p. 65-

69.

209. Aschner, J.L. and R.L. Poland, *Sodium bicarbonate: Basically useless therapy.* Pediatrics, 2008. **122**(4): p. 831-835.

210. Corbet, A.J., J.M. Adams, J.D. Kenny, J. Kennedy, and A.J. Rudolph, *Controlled trial of bicarbonate therapy in high-risk premature newborn infants.* Journal of Pediatrics, 1977. **91**(5): p. 771-776.

211. Huseby, J.S. and D.G. Gumprecht, *Hemodynamic effects of rapid bolus hypertonic sodium bicarbonate.* Chest, 1981. **79**(5): p. 552-554.

212. Laptook, A.R., *The effects of sodium bicarbonate on brain blood flow and O2 delivery during hypoxemia and acidemia in the piglet.* Pediatric Research, 1985. **19**(8): p. 815-819.

213. Lou, H.C., N.A. Lassen, and B. Friishansen, *Decreaded cerebral blood flow after administration of sodium bicarbonate in distressed newborn infants.* Acta Neurologica Scandinavica, 1978. **57**(3): p. 239-247.

214. Tibballs, J., *Bicarbonate and hemodynamics in neonates.* Intensive Care Medicine, 1993. **19**(2): p. 63-64.

215. Bailey, S.M., K.D. Hendricks-Munoz, J.T. Wells, and P. Mally, *Packed red blood cell transfusion increases regional cerebral and splanchnic tissue oxygen saturation in anemic symptomatic preterm infants.* American Journal of Perinatology, 2010. **27**(6): p. 445-453.

216. Cerussi, A., R. Van Woerkom, F. Waffarn, and B. Tromberg, *Noninvasive monitoring of red blood cell transfusion in very low birthweight infants using diffuse optical*

*spectroscopy.* Journal of Biomedical Optics, 2005. **10**(5): p. 9.

217. Dani, C., M. Pezzati, E. Martelli, C. Prussi, G. Bertini, and F.F. Rubaltelli, *Effect of blood transfusions on cerebral haemodynamics in preterm infants.* Acta Paediatrica, 2002. **91**(9): p. 938-941.

218. Dani, C., S. Pratesi, G. Fontanelli, J. Barp, and G. Bertini, *Blood transfusions increase cerebral, splanchnic, and renal oxygenation in anemic preterm infants.* Transfusion, 2010. **50**(6): p. 1220-1226.

219. Lee, J., A.E. Cerussi, D. Saltzman, T. Waddington, B.J. Tromberg, and M. Brenner, *Hemoglobin measurement patterns during noninvasive diffuse optical spectroscopy monitoring of hypovolemic shock and fluid replacement.* Journal of Biomedical Optics, 2007. **12**(2): p. 8.

220. Liem, K.D., J.C.W. Hopman, B. Oeseburg, A.F.J. deHaan, and L.A.A. Kollee, *The effect of blood transfusion and haemodilution on cerebral oxygenation and haemodynamics in newborn infants investigated by near infrared spectrophotometry.* European Journal of Pediatrics, 1997. **156**(4): p. 305-310.

221. Nelle, M., C. Hocker, E.P. Zilow, and O. Linderkamp, *Effects of red cell transfusion on cardiac output and blood flow velocities in cerebral and gastrointestinal arteries in premature infants* Archives of Disease in Childhood, 1994. **71**(1): p. F45-F48.

222. Younkin, D.P., M. Reivich, J.L. Jaggi, W.D. Obrist, and M. Delivoriapapadopoulos, *The effect of hematocrit and systolic pressure on cerebral blood flow in newborn infants.* Journal of Cerebral Blood Flow and Metabolism, 1987. **7**(3): p. 295-299.